

**STUDYING END PLATE DEFORMATION EFFECTS IN 37-  
ELEMENT CANDU® FUEL BUNDLES USING  
FINITE ELEMENT ANALYSIS**

**ÉTUDE DES EFFETS DE DÉFORMATION DES PLAQUE  
D'EXTRÉMITÉ D'UNE GRAPPE DE COMBUSTIBLE  
CANDU<sup>MD</sup> À 37 CRAYONS À L'AIDE D'UNE  
ANALYSE PAR ÉLÉMENTS FINIS**

A Thesis Submitted to the Division of Graduate Studies  
of the Royal Military College of Canada  
by

**Capt. William Payton-Stewart, BEng**

In Partial Fulfillment of the Requirements for  
The Degree Master of Applied Science

April 2023

© This paper may be used within the Department of National Defence but  
copyright for open publication remains the property of the author.

## Abstract

The CANDU® industry has supported the energy transition away from fossil fuels for over 50 years whilst continuing to invest in design and safety improvements. As part of this investment, they have pursued development of fuel bundle deformation models. The Royal Military College of Canada (RMC) has supported model development since 2015; demonstrating feasibility to replicate thermal bowing of fuel elements and begin work on a 3D bundle model using Finite Element Analysis (FEA). This study adds to that model by refining boundary conditions and applied loads, with a specific focus on end plate deformation. End plates have seldom been the focus of modeling studies and are in need of further investigation.

A model with several reactor based loads and frictional contact between the bundle and pressure tube was developed. In doing so, the effects of end plate constraints from both fuel latch and Fuel String Supporting Shield Plug (F3SP) modified fuel channels were compared. Deformation characteristics of the final models were in close agreement with measurements of an irradiated bundle from the Bruce generating station. Within the end plate, stresses were observed to concentrate in corners of the lower webs while deformation was greatest in the center ring. The bundle's end plate orientation was observed to affect end plate deformation, with increases of up to 54% in some instances. Thicker end plates reduced fuel element deformation by an average of 15% and decreased maximum end plate deformation by up to 21%. Controlling bundle orientation and increasing end plate thickness were assessed as promising factors for mitigating bundle deformation.

*Keywords: CANDU, Fuel Bundle, End Plate, Deformation, Model, Finite Element Analysis.*

## Résumé

L'industrie CANDU<sup>MD</sup> a contribué à la transition énergétique pour s'éloigner des combustibles fossiles depuis plus de cinquante ans tout en continuant d'investir dans l'amélioration des designs et de la sûreté. Une partie de ces investissements a été la poursuite du développement des modèles de la déformation de la grappe de combustible. Le Collège militaire royal du Canada (CMR) a supporté le développement de modèles depuis 2015, démontrant la faisabilité de reproduire la flexion thermique des crayons de combustible et le début de la recherche d'un modèle de grappe en trois dimensions à l'aide de l'analyse par éléments finis (AEF). La présente étude continue le développement de ce modèle en raffinant les conditions-frontières et les charges appliquées, avec une attention portée spécifiquement sur la déformation des plaques d'extrémité. Celles-ci ont rarement été le point focal des études de modélisation et un besoin existe pour de la recherche future.

On a développé un modèle comprenant plusieurs charges basées sur le réacteur et des contacts par friction entre la grappe et le tube de force, tout en comparant les contraintes de la plaque d'extrémité à partir des deux loquets du combustible et des canaux de combustible modifiés par des écrans de protection supportant l'enfilade des grappes de combustible. Les caractéristiques de déformation du modèle final étaient rapprochées des valeurs mesurées sur une grappe de combustible irradiée provenant de l'un des réacteurs de la centrale de Bruce. Dans la plaque d'extrémité, on a observé des contraintes concentrées dans les coins inférieurs des membrures de la plaque tandis que la déformation était la plus prononcée dans l'anneau central. On a observé que l'orientation de la plaque d'extrémité de la grappe avait un effet sur la déformation de la plaque, avec des allongements aussi élevés que 54 % dans certains cas. Des épaisseurs plus grandes pour les plaques d'extrémité réduisaient la déformation des grappes de combustible par 15 % en moyenne et la déformation maximale des plaques d'extrémité était réduite par 21 %. Un contrôle de l'orientation des grappes et une épaisseur accrue des plaques d'extrémité se sont révélées être des facteurs prometteurs pour réduire la déformation de la grappe de combustible.

*Mots-clefs: CANDU, grappe de combustible, plaques d'extrémité, modèle, l'analyse par éléments finis*

# Table of Contents

Abstract .....	ii
Résumé .....	iii
Table of Contents .....	iv
List of Tables .....	vi
List of Figures .....	vii
List of Symbols .....	xiii
List of Acronyms .....	xiv
Acknowledgements.....	xv
1. Introduction.....	1
2. Background.....	4
2.1 Nuclear Power.....	4
2.2 CANDU® Reactors.....	5
2.3 CANDU® Fuel Bundles .....	8
2.4 Fuel Bundle Deformation and Operating Conditions .....	10
3. State of the Art.....	13
3.1 Fuel Codes .....	14
3.2 Advanced Finite Element and Fully 3D Bundle Deformation Models .....	16
3.3 Experimental Studies.....	22
4. Research Objective .....	24
5. Methods and Research Approach .....	25
5.1 Model Development and Benchmarking.....	25
5.2 Analysis of End Plate Deformation Effects .....	25
5.3 End Plate Deformation Sensitivity Analysis .....	26
5.3.1 Bundle Orientation .....	26
5.3.2 End Plate Thickness .....	26
6. Theory .....	27
6.1 Principles of Finite Element Analysis.....	27
6.2 Nonlinear Finite Element Models.....	30

6.3 Finite Element Analysis and Computers .....	33
7. Model Development and Benchmarking .....	34
7.1 Material Properties .....	34
7.2 Bundle and Fuel Element Temperature Profiles.....	36
7.3 Mechanical Loads – Pellets, Weight, and Coolant Forces.....	38
7.3.1 Estimation of Coolant Dynamic Pressure .....	40
7.4 Single Outer Fuel Element Models .....	41
7.4.1 Bearing Pad Boundary Conditions .....	42
7.4.2 Temperature Profiles.....	44
7.5 Full Bundle Model.....	46
7.5.1 End Plate Boundary Conditions .....	50
7.5.2 Pellet Stiffening Effects .....	60
7.5.3 Mesh Convergence Study .....	67
7.6 Model Benchmarking and Verification .....	71
7.6.1 Solid Mechanics Verification .....	71
7.6.2 Comparison with Post-Irradiation Data.....	75
8. End Plate Deformation Analysis .....	81
8.1 End Plate Deformation at NOC .....	81
8.2 Effect of Bundle Orientation on Deformation .....	85
8.3 Effect of End Plate Thickness on Deformation .....	90
9. Discussion .....	93
9.1 End Plate Deformation at NOC .....	93
9.2 Effects of Bundle Orientation on Deformation .....	94
9.3 Effects of End Plate Thickness on Deformation .....	95
10. Conclusions .....	97
11. Recommendations.....	98
12. References .....	100

## List of Tables

Table 1: Zircaloy-4 Properties at Various Temperatures from MATPRO [39] .....35

Table 2: Zircaloy-4 Creep Constants for Accelerated Deformation Rate [41] .....36

Table 3: End Flux Peaking Factors and Linear Element Powers [42] [43] .....37

Table 4: Initial Mesh Parameters used in Development of Full Bundle Model ....47

Table 5: Effects of Bundle / End Plate Orientation on Vertical Deformation .....85

## List of Figures

Figure 1: Global Energy Consumption by Source in 2020 (TWh) [1] .....	1
Figure 2: CO <sub>2</sub> Emissions Vs. Global Temperature Increase [4] .....	2
Figure 3: Simplified PWR Nuclear Power System [8] .....	5
Figure 4: The CANDU® Reactor [8] .....	6
Figure 5: CANDU® Reactor Fuel Channel Assembly [10].....	7
Figure 6: CANDU® 37-Element Bundle (Skewed End Plate Webs) [13] .....	8
Figure 7: CANDU® 37-Element Bundle (Staggered Bearing Pads) [8] .....	9
Figure 8: Fuel Element to End Plate Connection [16].....	10
Figure 9: 37-Element Bundle Sub Channel Identification [19] .....	11
Figure 10: BOW Code - Driving Forces for Fuel Element Deflection [24] .....	15
Figure 11: Pellet/Sheath Interaction Affecting Fuel Element Stiffness [25] .....	16
Figure 12: Soni's [27] Partial (12) Element Bundle Model without Fuel Pellets ..	17
Figure 13: Williams' and Yatabe's [28] Single Fuel Element Model Including Pellets and Heat Generation – Temperatures in °C.....	18
Figure 14: Bell and Lewis Beam Modeling of 37-Element CANDU® Fuel Bundle [Adapted from 29] .....	19
Figure 15: Lee et al's [30] Full Bundle Model Without Pellets .....	20
Figure 16: Magnified (5X) End Plate Deformation as Observed by Lee et al [30] for End Plates with Axially Fixed Webs (Left) and Axially Fixed Face (Right) .....	21

Figure 17: Deformation Trends Observed from Post-Irradiation Analysis [31]....	23
Figure 18: Types of Elements used to Discretize Geometries for FEA [34] .....	27
Figure 19: Impact of Mesh Refinement on Recreating Curved Geometries [36].	28
Figure 20: Example of Graphical Output from FEA Software [37] .....	30
Figure 21: Graphical Representation of the Newton-Raphson Method [38].....	32
Figure 22: 37-Element Bundle End Flux Peaking Temperature Profile (°C) .....	38
Figure 23: Single Outer Fuel Element and Pressure Tube Model.....	42
Figure 24: Vertical deformation of an Outer Fuel Element at 300 °C with Pellet Weight, Creep, and Bonded contact between the Center Bearing Pad and Pressure Tube (mm, 50X Magnification) .....	43
Figure 25: Vertical deformation of an Outer Fuel Element at 300 °C with Pellet Weight, Creep, and Unbonded (Frictional) contact between the Center Bearing Pad and Pressure Tube (mm, 50X Magnification) .....	43
Figure 26: Outer Fuel Element End Flux Peaking Temperature Profile .....	44
Figure 27: Vertical deformation of an Outer Fuel Element at 300°C with Pellet Weight, Creep, and Free End Caps (mm, 50X Magnification) .....	45
Figure 28: Vertical deformation of an Outer Fuel Element with End Flux Peaking Temperatures, Pellet Weight, Creep, and Free Endcaps (mm, 50X Magnification) .....	45
Figure 29: Vertical deformation of an Outer Fuel Element at 300°C with Pellet Weight, Creep, and Axially Fixed Endcaps (mm, 50X Magnification) .....	45
Figure 30: Vertical deformation of an Outer Fuel Element with End Flux Peaking Temperatures, Pellet Weight, Creep, and Axially Fixed Endcaps (mm, 50X Magnification) .....	45



Figure 31: 37-Element CANDU® Bundle Model with Simplified Pressure Tube..	47
Figure 32: Midplane Spacer Pad Contact Pairs .....	48
Figure 33: Initial Bottom Element Contact Status with Pressure Tube.....	49
Figure 34: Nominal Bundle Orientation and Fuel Element Identification.....	49
Figure 35: CANDU® Fuel Channel Architecture - Modified Downstream Shield Plug Highlighted in Red - Adapted from [45] and [47].....	51
Figure 36: Temperature Profile (A) and Pellet Weight Loading (B).....	52
Figure 37: Upstream Coolant Pressure (A) and Downstream Fuel Bundle Support - Latches (B) and F3SP Shield Plug (C).....	52
Figure 38: Vertical deformation of a Latch (A) and Shield Plug (B) Supported 37-Element Bundle with Empty Fuel Elements, End Flux Temperatures, Pellet Weight, Coolant Pressure, and Creep (mm, 15X Magnification).....	54
Figure 39: Axial Deformation of a Latch Supported Bundle with End Flux Temperatures, Pellet Weight, Coolant Pressure, and Creep. Full Bundle (A), Upstream Endplate (B), and Downstream Endplate (C) (mm, 15X Magnification) .....	55
Figure 40: Axial Deformation of a Shield Plug Supported Bundle with End Flux Temperatures, Pellet Weight, Coolant Pressure, and Creep. Full Bundle (A), Upstream Endplate (B), and Downstream Endplate (C) (mm, 15X Magnification) .....	55
Figure 41: Difference in radial displacement of Outer Fuel Elements at the bundle midplane - Latch Vs. Shield Plug Supported Bundle (mm) .....	56
Figure 42: Difference in radial displacement of Intermediate Fuel Elements at the bundle midplane - Latch Vs. Shield Plug Supported Bundle (mm) .....	57
Figure 43: Difference in radial displacement of Inner Fuel Elements at the bundle midplane - Latch Vs. Shield Plug Supported Bundle (mm) .....	58

Figure 44: Vertical Deformation of a Latch Supported Bundle with End Flux Temperatures, Pellet Weight, Coolant Pressure, and Creep. Bundle with Hollow Fuel Elements (A), Solid Fuel Elements (B), and Solid Fuel Elements with 20X Creep (C) (mm, 15X Magnification) .....62

Figure 45: Vertical Deformation of a Shield Plug Supported Bundle with End Flux Temperatures, Pellet Weight, Coolant Pressure, and Creep. Bundle with Hollow Fuel Elements (A), Solid Fuel Elements (B), and Solid Fuel Elements with 20X Creep (C) (mm, 15X Magnification) .....62

Figure 46: Difference in radial displacement of Outer Fuel Elements at the Bundle midplane between Bundles with Hollow and Solid Fuel Elements for a Latch supported Bundle (mm) .....63

Figure 47: Difference in radial displacement of Outer Fuel Elements at the Bundle midplane between Bundles with Hollow and Solid Fuel Elements for a Shield Plug supported Bundle (mm) .....64

Figure 48: Difference in Location of Maximum Stress between Bundles with Hollow Fuel Elements (A) and Solid Fuel Elements (B) (15X Magnification) .....65

Figure 49: Fuel Element Mesh Convergence Study using Maximum Vertical Deformation and Fuel Element mesh sizes of 7 mm, 5.5 mm, 3.5 mm, and 2 mm .....68

Figure 50: Selected Fuel Element Mesh sizes comparing accuracy to recreate Fuel Element geometry 3.5 mm (A), 2 mm (B), 7 mm (C) .....68

Figure 51: End Plate Mesh Convergence Study using Maximum Von Mises Stress and End Plate Mesh sizes of 2.5 mm, 2 mm, 1 mm, 0.5 mm, and 0.4mm .....69

Figure 52: Selected End Plate Mesh sizes comparing accuracy to recreate End Plate geometry 1 mm (A), 0.4 mm (B), 3 mm (C) .....70

Figure 53: Simply Supported Beam Approximation for Intermediate Fuel Elements - Adapted from [48] .....72

Figure 54: Midspan Vertical Deformation of Intermediate Fuel Elements in a Latch Supported Bundle for Solid Mechanics Verification – Pellet Weight and Coolant Pressure but no Creep or Thermal Expansion (mm, No Magnification) 74

Figure 55: 37-Element Bundle Model comparisons to Post-Irradiation data – Radial displacement of Outer Fuel Elements at the bundle Quarter Plane – Radial axis scaled at 0.2 mm increments .....76

Figure 56: 37-Element Bundle Model comparisons to Post-Irradiation data – Radial displacement of Outer Fuel Elements at the bundle Midplane – Radial axis scaled at 0.2 mm increments.....77

Figure 57: 37-Element Bundle Model comparisons to Post-Irradiation data – Radial displacement of Outer Fuel Elements at the bundle Three Quarter Plane – Radial axis scaled at 0.2 mm increments .....78

Figure 58: Comparison of Upstream Endplate Vertical deformation at NOC for Latch (A) and Shield Plug (B) Supported Bundles (mm, 15X Magnification) .....81

Figure 59: Comparison of Downstream Endplate Vertical deformation at NOC for Latch (A) and Shield Plug (B) Supported Bundles (mm, 15X Magnification) .....82

Figure 60: Comparison of Upstream Endplate Axial deformation at NOC for Latch (A) and Shield Plug (B) Supported Bundles (mm, 15X Magnification) .....82

Figure 61: Comparison of Downstream Endplate Axial deformation at NOC for Latch (A) and Shield Plug (B) Supported Bundles (mm, 15X Magnification) .....83

Figure 62: Comparison of Upstream Endplate Von Mises Stress at NOC for Latch (A) and Shield Plug (B) Supported Bundles (MPa, 15X Magnification) .....83

Figure 63: Comparison of Downstream Endplate Von Mises Stress at NOC for Latch (A) and Shield Plug (B) Supported Bundles (MPa, 15X Magnification) .....84

Figure 64: Effect of Bundle Orientation on Spacer Pad Contact Pressure.....89

Figure 65: Effect of Increased End Plate Thickness on Midplane radial displacement of Outer Fuel Elements (mm) .....90

Figure 66: End Plate Thickness Vs. Vertical Deformation of Upstream End Plate – Nominal End Plate (A), 25% Thicker End Plate (B), 50% Thicker End Plate (C), and 100% Thicker End Plate (D) (mm, 15X Magnification).....91

Figure 67: End Plate Thickness Vs. Axial Deformation of Upstream End Plate Nominal End Plate (A), 25% Thicker End Plate (B), 50% Thicker End Plate (C), and 100% Thicker End Plate (D) (mm, 15X Magnification).....92

## List of Symbols

$A_{PT}$	Pressure Tube (Hollow) Cross Sectional Area
$C_1$	First Creep Constant
$C_2$	Second Creep Constant
$C_3$	Third Creep Constant
$D_{OD}$	Outer Diameter of a Hollow Tube
$D_{ID}$	Inner Diameter of a Hollow Tube
$E$	Elastic Modulus
$I$	Moment of Inertia
$I_{Fuel\ Element}$	Moment of Inertia for a Fuel Element
$L$	Length (of a Simply Supported Beam)
$P$	Axial Load on the End of a Beam
$P_C$	Critical Buckling Factor
$P_{Coolant}$	Dynamic Coolant Pressure
$T$	Temperature
$T_{ID}$	Inner Diameter of a Pressure Tube
$V_{Coolant}$	Coolant Velocity
$w$	Weight / Distributed Load (on a Simply Supported Beam)
$\Delta_{Midspan}$	Midspan Deflection of a Simply Supported Beam
$\epsilon_{Creep}$	Creep Strain Rate
$\sigma$	Von Mises Stress

## List of Acronyms

AECL	Atomic Energy of Canada Limited
BNGS	Bruce Nuclear Generating Station
BWR	Boiling Water Reactor
CANDU®	CANada Deuterium Uranium
CFD	Computational Flow Dynamics
CMC	Canadian Microelectronics Corporation
CNL	Canadian Nuclear Laboratories
COG	CANDU® Owners Group
CPU	Central Processing Unit
CTF	Curvature Transfer Factor
DNGS	Darlington Nuclear Generating Station
ECCS	Emergency Core Cooling System
F3SP	Fuel String Supporting Shield Plug (Design Nomenclature)
FEA	Finite Element Analysis
INL	Idaho National Laboratories
IPCC	Intergovernmental Panel on Climate Change
MOOSE	Multiphysics Object Oriented Simulation Environment
NOC	Normal Operating Conditions
PWR	Pressurized Water Reactor
RAM	Random-Access Memory
REF	Rigidity Enhancement Factor
SPEL	Sheridan Park Engineering Laboratory

## Acknowledgements

The author wishes to thank Dr. D. Wowk and Dr. P. Chan for their guidance and counsel in the completion of this study. Their expertise and understanding of the gaps in the modern nuclear modeling field ensured the efforts of this research were valuable and aligned with industry priorities. On top of holding key positions and responsibilities in their departments, they always made themselves available to support the author. Appreciation is extended to the Canadian Armed Forces and their Sponsored Post-Graduate program that allowed the author to pursue their graduate degree.

Acknowledgement is given to previous RMC students, Lee and Soni, for the work they completed to develop the initial model and geometry used as a foundation for this thesis. The advances and capabilities of the final model presented herein would not have been possible within a two year program if not for their previous efforts.

Financially, contributions from CANDU® Owners Group (COG) were integral to supporting this work. They also provided invaluable experimental data for model comparison and benchmarking. Further funding was provided by the Natural Sciences and Engineering Research Council of Canada (NSERC) for attendance of conferences to discuss this study and receive input from industry experts.

Lastly, CMC microsystems provided access to high power computing hardware and software licenses, without which the execution of this research would not have been possible.

# 1. Introduction

Reliable access to energy has been the basis for the development of modern society and the economic benefits that have accompanied it. The amount of energy consumed in daily life through transportation, manufacturing, agriculture, housing, and communication is staggering. In 2020 Canada had one of the highest energy uses per capita at over 360 GJ per person; an amount equal to 59 barrels of oil [1]. The developed world is so reliant on access to energy that to lose it would constitute far more than an inconvenience. With global energy demand continuing to increase, the security, stability, and affordability of energy production is at the forefront of political debate. This has become no more apparent than during the oil and gas price instability during the Russo-Ukraine war. Despite the advent of new energy technologies the primary global source continues to be fossil fuels including oil, its derivatives, natural gas, and coal [1]. Combined they account for more than 80% of global energy consumption as per Figure 1.

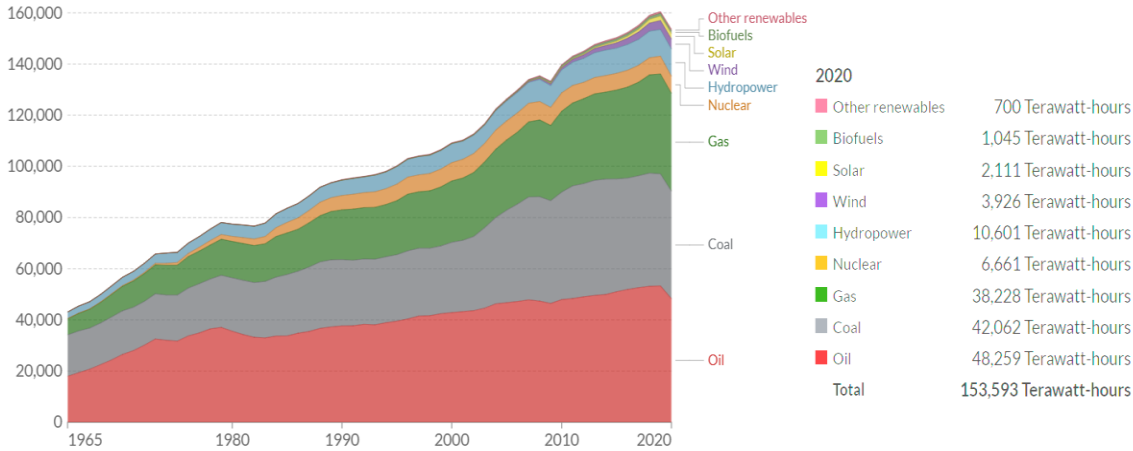


Figure 1: Global Energy Consumption by Source in 2020 (TWh) [1]

The prolific use of fossil fuels has also come at the expense of emissions that have led to climate change. Average global temperatures have risen with emissions as per Figure 2 and the effects are becoming more noticeable. Forest fires, heatwaves, and severe weather events are increasing in frequency and scale. The Intergovernmental Panel on Climate Change (IPCC) has reported that



carbon neutrality must be reached by 2050 for a 50% chance to limit warming to 1.5°C [2]. Beyond 1.5°C, warming effects are expected to accelerate through positive feedback loops that accompany higher temperatures [3]. This gives a maximum of 30 years for the world to divest itself of the fossil fuels that currently provide 80% of its energy.

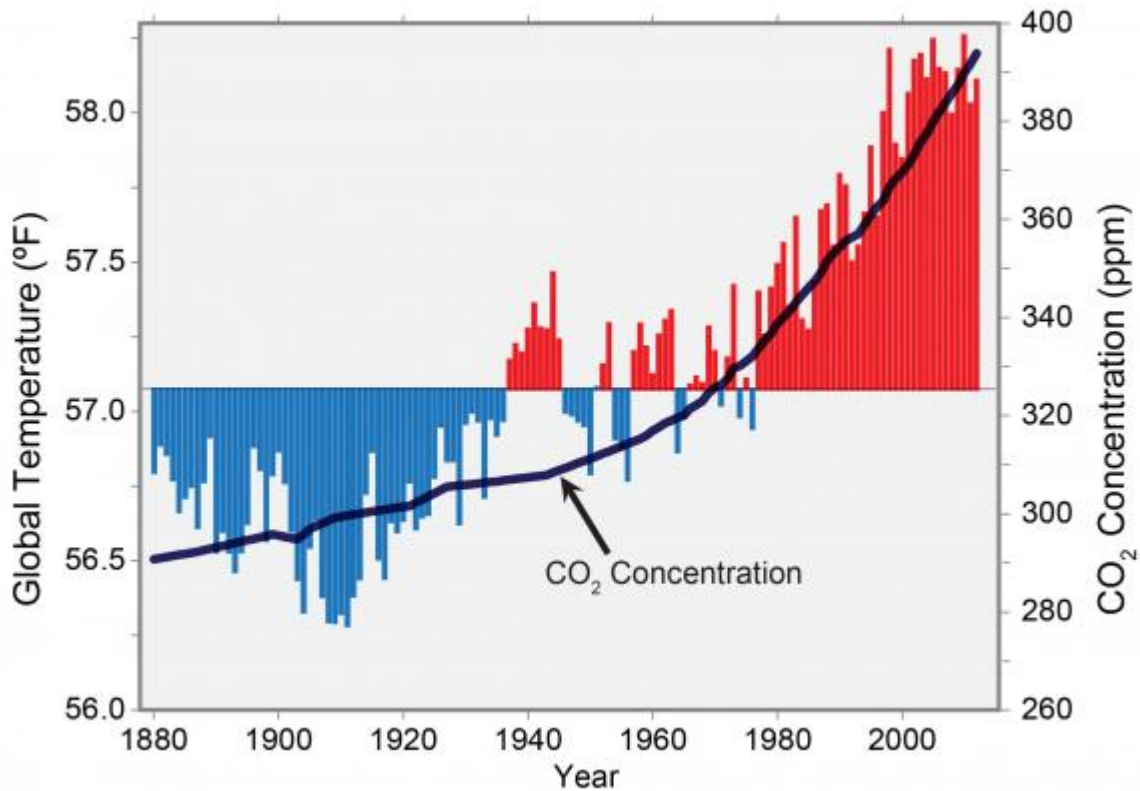


Figure 2: CO<sub>2</sub> Emissions Vs. Global Temperature Increase [4]

Alternative energy sources are needed but they have to meet a complex list of criteria. They must be able to quickly replace existing generation capacities, be carbon neutral, sustainable, geographically secure, and grow with demand [2]. Electrification of the transportation industry alone will require a large increase in generating capacity as countries begin banning new fossil fuel vehicles in 2035 [5]. Solar, wind, and hydroelectric power are the prevailing carbon neutral sources that receive the most focus. Nuclear energy, however, has some advantages over these sources and also has the potential to make a significant impact in the net zero carbon effort.

Even with renewables becoming less expensive, they still have difficulty competing with the energy density and relative geographic independence afforded by fossil fuels. Renewable energy sources suffer in these aspects because they are at the mercy of the environment and are only effective when and where their respective phenomena are present. This requires large amounts of land and transmission infrastructure to get the electricity from the best geographic sites to where it is needed. As a result, a power grid dominated by renewables is expected to require supplemental energy through expensive storage technologies or additional fossil fuel based generation [6]. This is where nuclear power is beneficial in aiding the transition to renewables. New nuclear power plants can be built effectively anywhere and are a stable and reliable form of energy generation. They average a higher capacity factor than solar or wind energy, meaning that a larger generating volume of solar and wind is required for the same net output over equivalent facility lifetimes [7].

Given the short 30 year timeline to reach net zero emissions and increasing economic concerns, many experts agree that nuclear energy must have a place in both short and long term energy production. Scenarios developed by the IPCC for emission reduction concluded that an increase in nuclear power between 98% and 500% would be necessary to meet the 1.5°C target [2]. Technological expansion and research into nuclear technologies is therefore important for combating climate change while maintaining stable energy production. Improving existing reactor designs and developing new ones will be integral to meeting the energy demands of the future.

Of current interest to the Canadian nuclear industry is the development of models for predicting fuel bundle behaviour inside the reactor under a variety of operating conditions. These models can provide insight into bundle susceptibility to failure at extreme conditions or high burnups when trying to get the most amount of energy out of the fuel. This information can be used to improve reactor efficiency and better understand safety limits. Accordingly, the goal of this thesis was to contribute to the development of these models by completing studies to understand the effects both to and from the end plate in fuel bundle deformation.

## 2. Background

### 2.1 Nuclear Power

Nuclear reactors produce electricity using the heat energy from nuclear fission to produce steam that turns turbines connected to electrical generators. The use of steam to turn a turbine and generate electricity is not a novel concept, but to produce that steam from controlled nuclear fission has proven to be a significant scientific and engineering achievement. Nuclear fission is an exothermic reaction defined as the spontaneous and induced splitting of atoms into smaller nuclei. The induced fission process is used in nuclear reactors to accelerate fission rates and produce usable amounts of energy [8]. This is accomplished by moderating the neutrons released during fission to create a sustained chain reaction of fissions in other atoms. As the chain reaction proceeds, heat is released and captured by a coolant (typically water) that is then transformed into steam used by generators. The method by which this cooling is performed differentiates the two most common types of nuclear reactors; Boiling Water Reactors (BWR) and Pressurized Water Reactors (PWR).

BWRs use a single cooling loop to both cool the fuel and produce steam for the generator while PWRs employ two cooling loops connected by steam generators that act as a heat exchanger. The secondary loop in a PWR is connected to the electrical generators while the primary loop cools the fuel directly [8]. The advantage of two cooling loops in a PWR is that the primary coolant flowing over the fuel is pressurized so that it may operate at a higher temperature and improve thermal efficiency. This benefit has resulted in the majority of the world's reactors being some variation of a PWR design. A simplified diagram of a PWR, including the reactor and both coolant loops is pictured below in Figure 3.

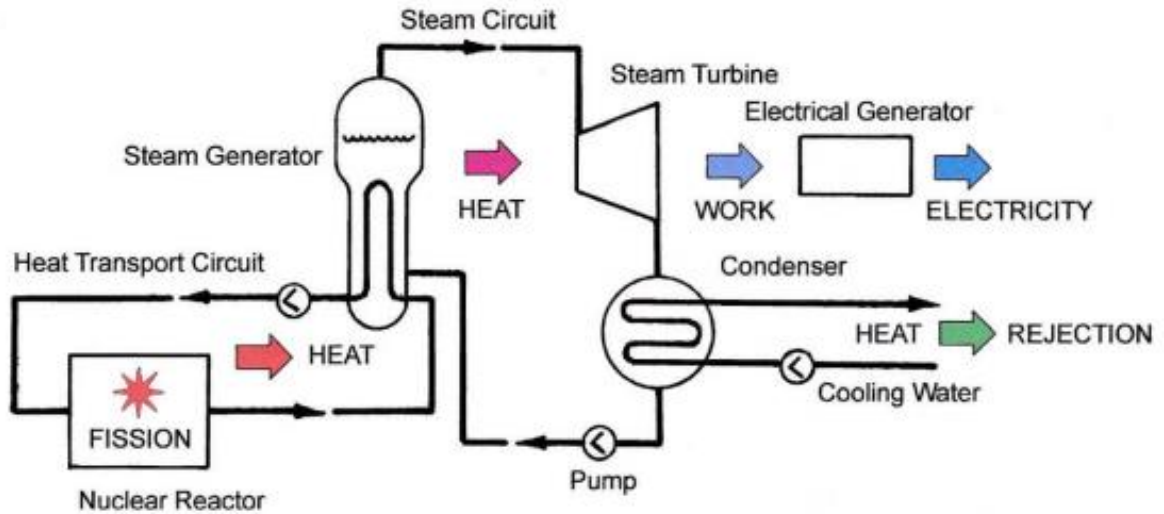


Figure 3: Simplified PWR Nuclear Power System [8]

Uranium-235 (U-235) is the primary fissionable isotope used in power reactors but is of a dilute quantity in natural uranium making up only 0.71%. As a result, most reactor designs require enrichment to sustain a critical fission rate by increasing the concentration of U-235. For most BWRs and PWRs this enrichment increases the U-235 concentration to 3-5% [8]. However, one reactor design in particular, the CANDU<sup>®</sup> (Canada-Deuterium Uranium) reactor, is able to use natural Uranium as fuel. This is due to the high neutron economy afforded by the use of heavy water in the reactor vessel and as primary coolant [8]. The CANDU<sup>®</sup> reactor has been an extremely successful design because of its ability to sustain criticality using a variety of fuel compositions, refuel without shutting down, and its comprehensive complement of safety features [8].

## 2.2 CANDU<sup>®</sup> Reactors

Design of the CANDU<sup>®</sup> reactor began in 1954 as part of Canada's post World War II nuclear innovation. At the time Canada was limited by its industry and unable to construct large pressure vessels or produce the enriched Uranium needed by most designs [9]. Atomic Energy of Canada Limited (AECL) responded by designing the CANDU<sup>®</sup> reactor pictured in Figure 4. The CANDU<sup>®</sup> reactor is a type of Pressurized Heavy Water Reactor (PHWR) and instead of the large monolithic pressure vessel used by other reactors, several smaller

pressure tubes are placed inside of a large unpressurized vessel called a Calandria. The pressure tubes themselves are housed in Calandria tubes and separated by an annulus gas of CO<sub>2</sub> to create fuel channel assemblies as per Figure 5. The fuel for the reactor is then assembled into bundles that are loaded into these fuel channels. The Calandria contains 380 to 480 fuel channel assemblies depending on the reactor's power rating [8]. They are precisely spaced to maintain a critical number of fission reactions that allow the reactor to produce sufficient heat to generate steam. Coolant is pumped through independent feeder pipes to the pressure tubes where it flows over fuel bundles to remove heat. That coolant is then circulated through the steam generators to produce steam in the secondary cooling loop connected to electric generators [8].

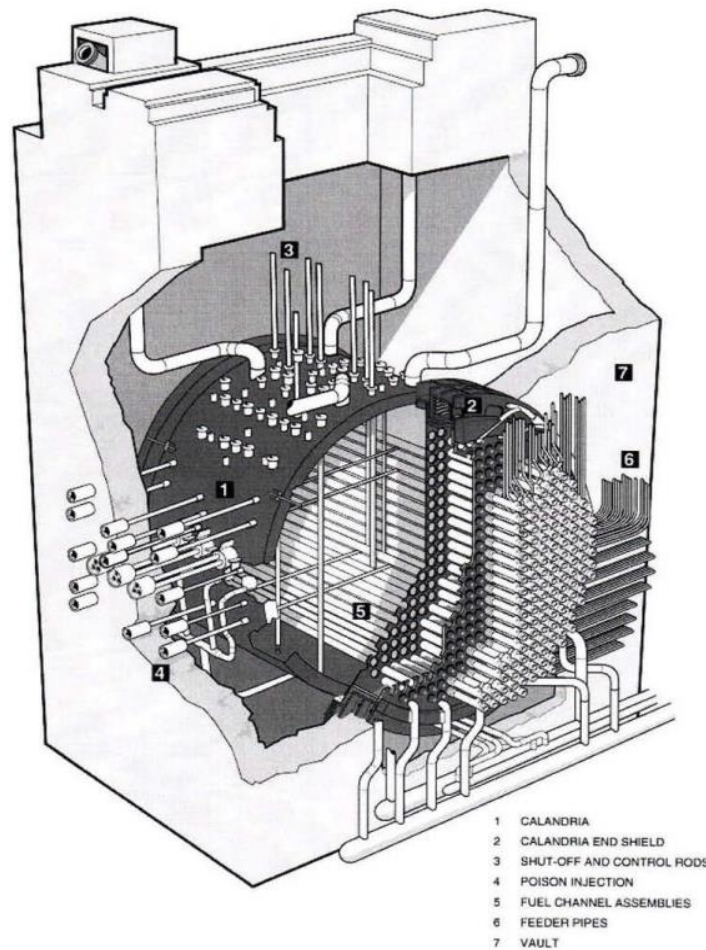


Figure 4: The CANDU® Reactor [8]

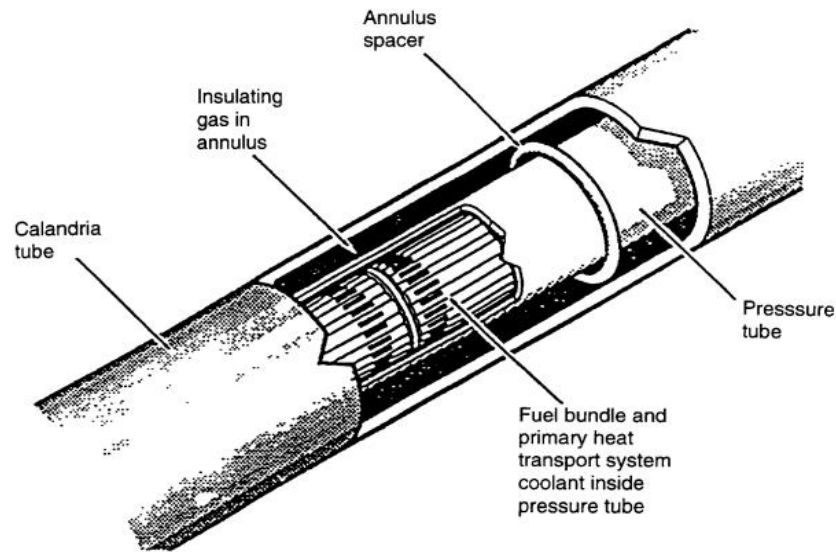


Figure 5: CANDU® Reactor Fuel Channel Assembly [10]

In response to the limited access to enrichment facilities, CANDU® engineers elected to use heavy water as both the neutron moderator and primary coolant of the reactor. Heavy water has similar properties to normal water except the hydrogen atoms of the water molecules are replaced with deuterium; a hydrogen atom with a neutron. The deuterium reduces the neutron absorbing cross section of heavy water and creates a superior neutron economy [8]. This allows CANDU® reactors to sustain criticality without enriched Uranium. The use of unenriched Uranium does however, have the consequence of requiring the reactor to be refueled more frequently. This led to the design of the iconic CANDU® fuel bundle and the on-power refueling system. Together they maximize the reactor's capacity factor by keeping fuel assemblies small and allowing continuous operation, while fuel bundles are exchanged.

The CANDU® reactor has proved itself over more than 50 years of operation. As of 2016 there were 29 CANDU® reactors in operation around the world with 19 of them in Canada having a combined output of more than 14,000 MW. In the Canadian province of Ontario, CANDU® reactors provide roughly 60% of the province's electricity needs [11]. Accordingly, they have been integral to phasing out fossil fuel based power generation in the province and combating climate change. A further testament to the reliability and superb design of the CANDU®

system is that a reactor at the Darlington station currently holds the world record for longest continuous operation at more than 963 days [12]. This success all relies in part on the robust and reliable fuel bundle design.

### 2.3 CANDU® Fuel Bundles

Different generations of CANDU® reactors have used slightly different bundle designs but they have all followed the same general shape so that they could continue to work with the original reactor architecture. Changes have primarily been in the number and diameter of fuel elements along with the end plate shape to accommodate them. Fuel bundles have been designed with 28, 37, and 43 fuel elements but have maintained the same overall dimensions by decreasing element diameters as the total number of elements in the bundle increases [8]. The 37-element bundles are the most common and are used in the majority of operating reactors. Within the 37-element design there are some sub designs pictured below in Figures 6 and 7. The difference between these designs comes down to the bearing pad placement and end plate geometry.

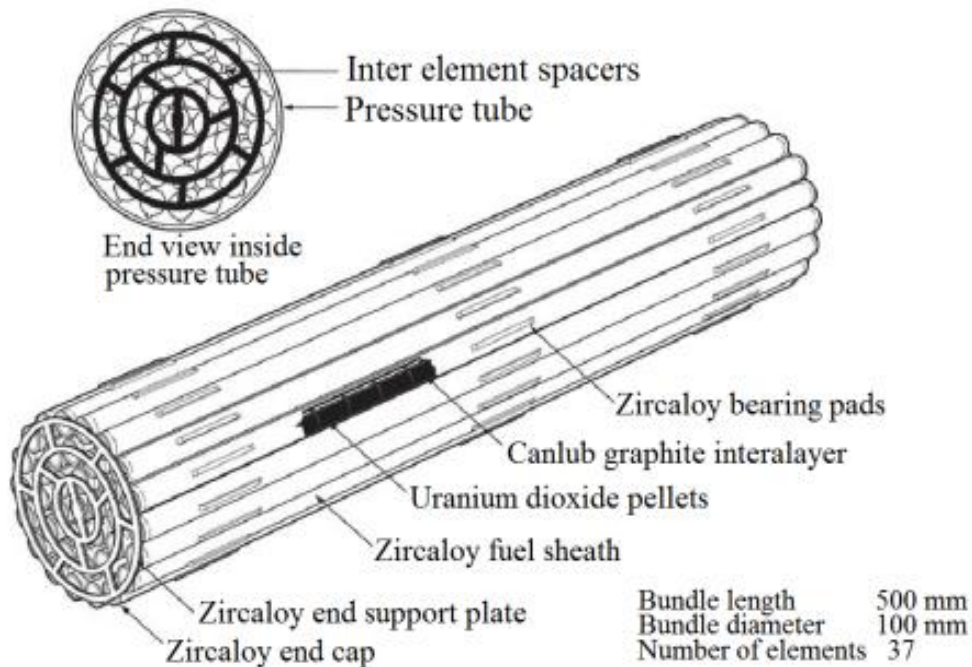


Figure 6: CANDU® 37-Element Bundle (Skewed End Plate Webs) [13]



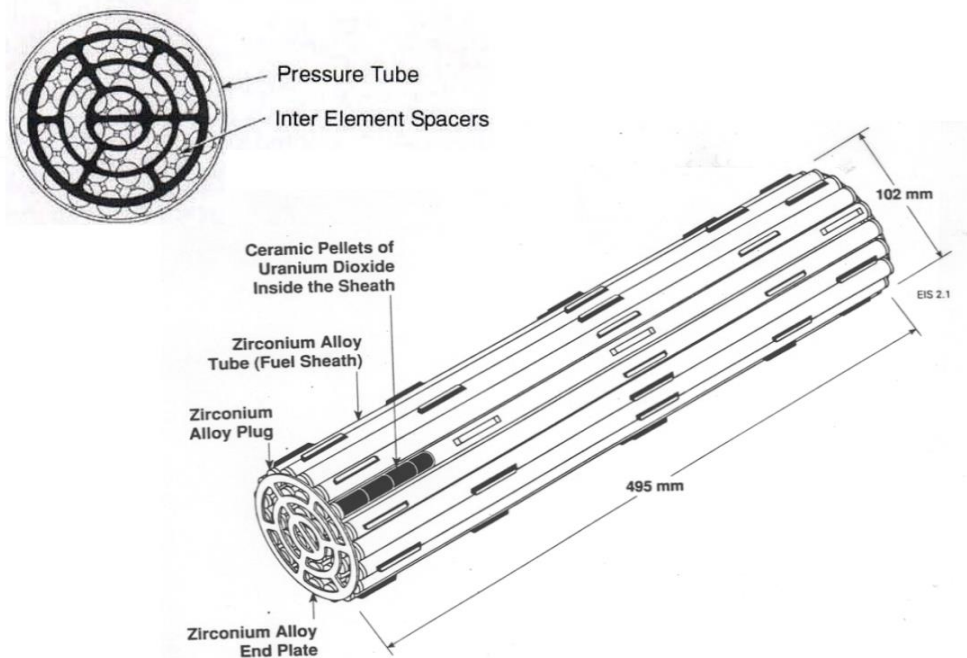


Figure 7: CANDU<sup>®</sup> 37-Element Bundle (Staggered Bearing Pads) [8]

The bundles are constructed entirely of a Zirconium alloy known as Zircaloy-4. This alloy consists of roughly 95% Zirconium with trace amounts of alloying elements for strength and corrosion resistance [14]. This alloy provides the best combination of thermal, mechanical, and neutron absorption properties. The elements are filled with natural uranium dioxide pellets and sealed using a resistance-welded endcap as shown in Figure 8 [14]. The element sheaths are thin at only about 0.4 mm, which allows them to collapse onto the fuel pellets under the pressure of the coolant and increase thermal conductivity. Spacer and bearing pads are attached to the fuel elements to prevent them from contacting each other and the pressure tube, respectively [14]. Spacer pads are located between elements along the midplane of the bundle while bearing pads are found circumferentially on the outer elements only. In Canada, brazing is used to attach both types of pads, since the fuel elements are thin and traditional welding could damage their integrity [14]. India's Nuclear Fuel Complex, however, has recently developed an all welded bundle, without the use of brazing [15]. The fuel elements are arranged cylindrically and welded to the end plates at the endcaps, which is also shown in Figure 8.



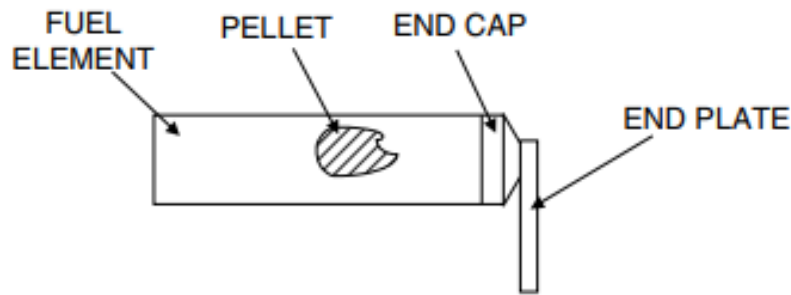


Figure 8: Fuel Element to End Plate Connection [16]

The structural integrity of the bundles is of great importance to reactor safety and operation as the bundles contain the fuel and radioactive fission products. Failure of the sheath can result in fission product contamination of the coolant and increase radiation levels in the reactor facility and spent fuel storage. Current statistics nevertheless demonstrate a strong track record for the reliability and robust nature of CANDU® fuel bundles, with an annual defect rate of less than 0.01% [14]. Even with such an incredible track record, a holistic understanding of bundle susceptibility to failure as the reactor and bundle's age remains critical to establishing safety and design limitations.

## 2.4 Fuel Bundle Deformation and Operating Conditions

CANDU® fuel bundles reside in one of the most complex and demanding engineering environments. They must be able to survive high temperatures, radiation, pressure, and corrosion without releasing their radioactive contents. This is the case both when the fuel bundle is in the reactor but also once it is placed into a cooling pool or long term storage [8]. Nominal operating conditions for a bundle inside the reactor see coolant temperatures and pressures of approximately 300 °C and 10 MPa for 6 - 24 months [8]. Stresses from exposure to this environment result in plastic deformation of the bundle through creep, which can increase the probability of a failure. These deformation effects are most pronounced when bundles are used in aged pressure tubes, at high burnups, or are subjected to accident conditions [17].

Accidents or reactor trips can come in several forms and initiate through a variety of means but they all generally pose the same concern for the fuel bundles; a

loss of cooling capacity causes an uncontrolled increase in bundle temperature. Although the active fission process may be halted by one or many of the CANDU® reactors safety features, decay heat will still cause a rapid rise in bundle temperature without the continuous flow of coolant [18]. The Emergency Core Cooling System (ECCS) is designed to prevent this from happening but it may take time to initiate depending on the nature of the accident [18]. The concern then becomes the temperature the bundles reach before the ECCS can take effect or if it fails.

An abrupt increase in temperature from decay heat will decrease the stiffness of the Zirconium alloy causing increased deformation of the bundle. This can permanently reduce subchannel area and the ability for coolant to flow through the bundle [17]. These subchannels are identified in Figure 9. It is also possible that deformation becomes so severe that individual fuel elements contact one another or the pressure tube itself. In both cases, hot spots and fretting can occur, which significantly increases the risk of failure and renders the bundles unsafe for further operation. The end plates, spacer pads, and bearing pads aid to prevent this from occurring, but can only combat a limited amount of deformation, especially at accident conditions [17]. Although bundle deformation is of large concern under or during accident conditions, it is also a concern under normal operating conditions (NOC), since deformation still occurs, albeit at a much slower rate.

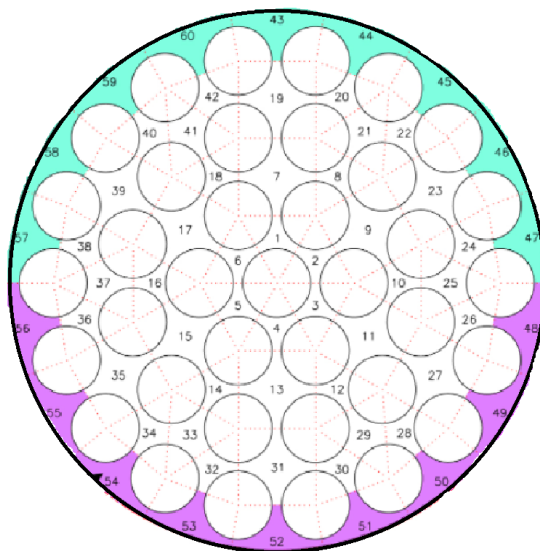


Figure 9: 37-Element Bundle Sub Channel Identification [19]

The standard life of a bundle in the reactor results in minor deformation from the prolonged exposure to thermomechanical loads, but becomes more pronounced at high burnups and when the bundles are used in aged pressure tubes. While in the reactor, bundles are loaded axially by pressure from coolant flow and contact with adjacent bundles. Additionally, the weight of the  $\text{UO}_2$  fuel pellets loads the bundle in the direction of gravity and is significant due to the high density of Uranium. The heat generated by fission then increases temperatures and causes creep deformation under these loads [17]. Creep is defined as the plastic deformation of a material over time when subjected to a stress below the yield stress. It is accelerated at higher temperatures by increased diffusion and dislocation movement at the atomic level [20]. The longer the bundles are in the reactor the more time they have to creep and deform. At high burnups, bundles also experience a drop in thermal conductivity from irradiation induced structural changes in the fuel. This causes bundles in high power positions and those towards the end of their life to run hotter [21]. Radiation itself also causes a complex radiation induced creep phenomenon that further contributes to deformation through swelling and microstructural changes to the fuel and Zircaloy-4 cladding [22]. This is accompanied by effects such as radiation induced grain growth and hardening [22].

One of the lesser understood aspects of bundle deformation is the role end plates have on how a bundle deforms. It is well understood that fuel bundles change shape in the reactor, but how the end plate responds to these effects has not been the focus of many studies. The end plates join the fuel elements together to form the bundle. Thus any changes to or loads on the end plate will affect the rest of the bundle and vice versa. CANDU<sup>®</sup> bundle deformation is a complex phenomenon that is subject to a large number of factors from the reactor operating environment. This makes experimental evaluation difficult and has caused a shift towards computer modeling as the primary method of studying fuel bundle deformation, as will be presented in this thesis.

### 3. State of the Art

Modeling and computer based studies have formed the basis for much of the industry's predictive research and analysis of fuel bundle behaviour. Experiments are mainly conducted to help validate computer models and support their ability to predict results over a range of conditions. Physical experimentation to capture the phenomena of interest is both difficult and expensive given the materials involved and the difficulty in replicating reactor environments [23]. The competing factors of heat transfer, fluid flow, coolant pressure, microstructural material changes, and radiation damage make identifying specific contributors to deformation difficult. Furthermore, analyzing fuel removed from reactors presents an obvious safety hazard due to residual radiation, requiring the use of special facilities to complete analysis. The time delay between removing fuel from a reactor and analyzing it also introduces sources of error as the cooling period may allow some strain recovery [21]. The limitations to using experiments to study bundle deformation have therefore led to a preference for computer based modeling and codes over experiments and industry sampling.

Computer based analysis is not without its own limitations, as assumptions must be made when approximating the complexity of a reactor environment. Accounting for all factors in one simulation is often computationally prohibitive, but multiphysics simulations can sometimes be used to combine multiple factors into one simulation, such as thermal and mechanical loads [16]. In all cases, boundary conditions must be established for models to run, and depending on how these conditions are established, they can introduce sources of error to the model [17]. As a result, the field of reactor fuel modeling is filled with many different studies and models that all have their own benefits and drawbacks. No models have been developed that are comprehensive enough to cover all factors and conditions of interest. Understanding the existing models is thus an important step in developing new ones. The following sections will provide an overview of some of the modeling and experimentation completed for CANDU® fuel bundles relevant to this study.

### 3.1 Fuel Codes

The term fuel codes encompasses a large range of predictive simulation and modeling tools for nuclear fuel assemblies. They can be divided into three categories; specific application, transient and normal operating conditions (NOC), and severe damage analysis [22]. Specific application codes model aspects of fuel performance and design, such as the BOW code that simulates creep deformation of individual fuel elements in CANDU® bundles. Transient and NOC codes are used to study reactor fuel across a range of conditions including normal fuel lifecycles and accident conditions. These include ELESTRES and ELOCA for CANDU® fuel properties at different burnups or during loss of coolant scenarios. Severe damage codes are used for determining the outcome of large accidents and core damage, such as MAAP4 [22]. Although complex given their multifaceted approach and calculations, codes typically operate more like a calculator than a full simulation. Values are entered for environmental or reactor conditions and the codes complete calculations to plot data or specify the extent to which fuel structures change.

The BOW code is commonly referenced when considering structural behavior of CANDU® fuel bundles. It was developed by AECL and represents fuel elements as beams without a full 3D modeling representation [24]. It considers temperature variations, element power, hydraulic drag, pellet cracking, mechanical stress, and strength effects imparted on fuel elements through contact with neighboring elements and end plates [24]. It is used to predict the curvature, buckling, and change in length of fuel elements in response to these effects. The resulting lateral deflection of the fuel elements is referred to as bow, which is where the code gets its name. The bowing of a fuel element as described by the BOW code is represented in Figure 10. In addition to the bowing of elements, the code will also report if deflection is sufficient to contact neighboring fuel elements or the pressure tube. Its accuracy was substantiated by experiments completed at Sheridan Park Engineering Laboratory (SPEL), Whiteshell Laboratories, and Canadian Nuclear Laboratories (CNL) [24]. The BOW code does have its limitations. For one, the code requires both a Rigidity Enhancement Factor (REF) and Curvature Transfer Factor (CTF) to be prescribed to reflect the fuel pellet and sheath interaction. Furthermore, it does not provide an analysis of end plate stiffness or end plate connections and the role they play in how the fuel elements deform [24]. As a result, the interaction between these components may be more complicated than assumed and is

worth further exploration. This leads to the biggest limitation, which is the inability of the BOW code to complete full geometric modeling of the entire bundle to see how all elements deform together.

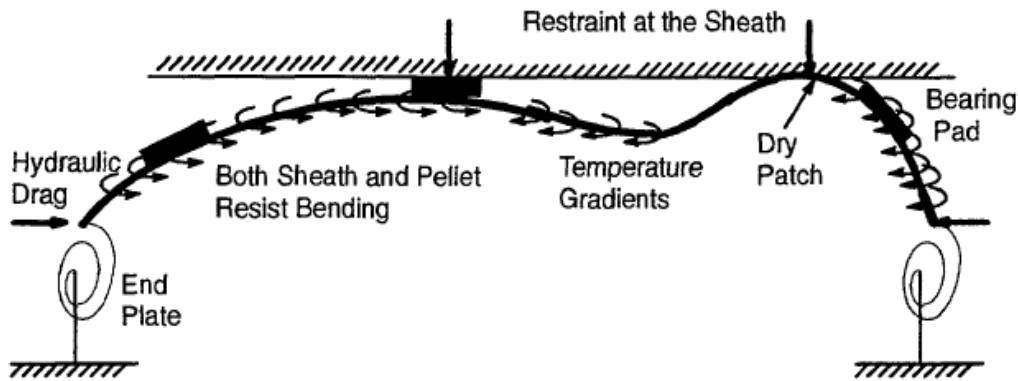


Figure 10: BOW Code - Driving Forces for Fuel Element Deflection [24]

Codes like ELESTRESS and ELOCA for NOC and transient conditions focus less on structural deformation and more on fuel performance through chemistry and the fission process. The ELESTRESS code requires inputs for burnup, element dimensions, coolant temperature, and pressure. It then calculates values including fission product distribution, pellet-sheath gaps, and fuel pellet properties including temperature and internal pressure [25]. The ELOCA code takes this a step further and determines the same types of values but for accident conditions at higher temperatures such as during a loss of coolant [25]. These codes are more beneficial in understanding fuel chemistry rather than mechanical behavior of the overall bundle and thus are less relevant to the current study. However, the properties of the fuel pellets as they change with burnup does have relevance to the stiffening effect they impart on the fuel element to resist deflection and bowing [25]. This is what the CTF and REF factor seek to account for in the BOW code. These codes and their factors of interest have an implicit effect on end plate deformation through the transfer of forces. However, they are ultimately of less consequence to end plate deformation. The pellet-sheath interaction and its effect on fuel element stiffness is shown in Figure 11.

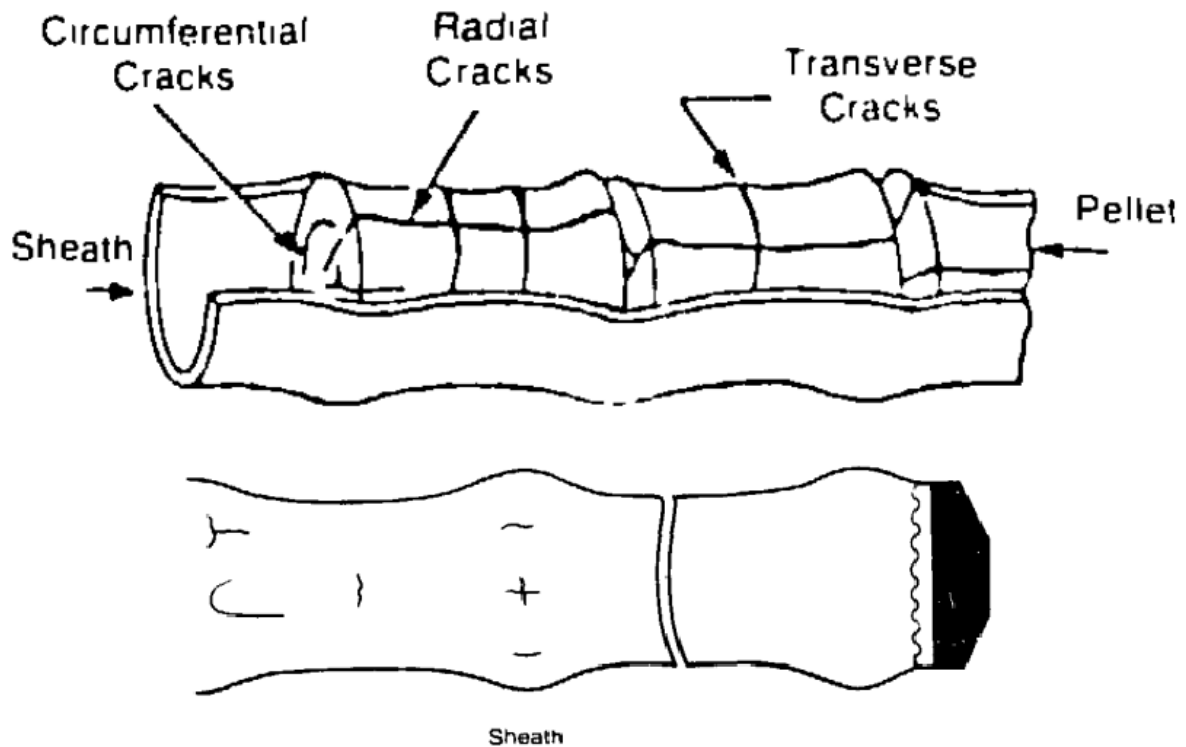


Figure 11: Pellet/Sheath Interaction Affecting Fuel Element Stiffness [25]

### 3.2 Advanced Finite Element and Fully 3D Bundle Deformation Models

Advanced Finite Element and Multiphysics Models capable of full 3D rendering are the predominant methods for modern CANDU® fuel bundle simulations. In comparison to the fuel codes discussed previously, programs such as ANSYS™, COMSOL Multiphysics™, ABAQUS™, and MOOSE/HORSE can be more comprehensive in their analysis. Aside from MOOSE (Multiphysics Object Oriented Simulation Environment) and its derivative HORSE, these programs are all commercial software applications used in a variety of industries. HORSE is an outlier in that it was developed by RMC for Idaho National Laboratory (INL), specifically for nuclear applications with horizontal fuel rods. Examples of the use of HORSE for CANDU reactors is limited, and few studies with it provide superior results to the other FEA software packages [26]. Accordingly this review of previous work will focus on models constructed using ANSYS™ and COMSOL Multiphysics™.

In 2017 Soni [27] studied the deformation behaviour of empty Zircaloy fuel elements and a partial 12 element bundle without fuel pellets using ANSYS™. Soni's [27] initial studies validated the use of ANSYS™ to replicate the deformation observed in heat up and strain experiments with empty elements. Thermal gradients were used as a temperature profile for the fuel elements, while gravity type loads were applied to simulate their weight and that of the fuel pellets [27]. The partial 12 element model extended the success of the agreement between ANSYS™ and the single element experiments to show sag and deflection in the partial bundle. This model is presented in Figure 12. The temperature gradient was between 1073 K and 873 K, which represented conditions beyond NOC, but had the benefit of exaggerating deformation effects. Minor changes to sub channel geometry were observed and no bowing great enough to cause pressure tube contact was seen [27]. The model's limitations were the omission of pellets from the elements and the associated effects. Furthermore, boundary conditions placed on the end plates limited the accuracy of the model at those locations. Overall however, Soni's [27] model was an important step in bundle modeling by validating ANSYS™ simulations for fuel elements with real experiments.

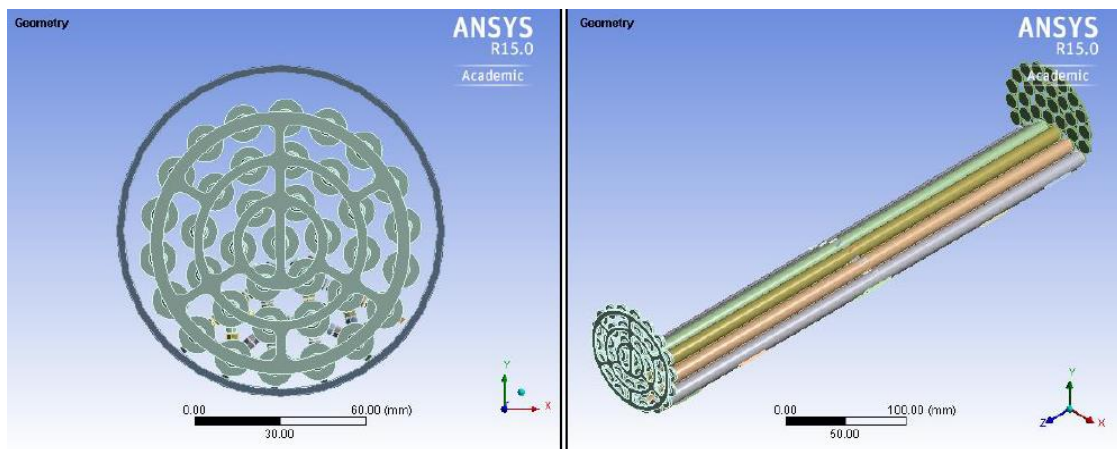


Figure 12: Soni's [27] Partial (12) Element Bundle Model without Fuel Pellets

Williams and Yatabe [28] expanded on the validation work completed by Soni [27] to develop a complete fuel element with pellets as the second step to a geometrically accurate 3D bundle model. Williams and Yatabe [28] needed to use two planes of symmetry to achieve solution convergence in response to computational difficulties that arose from including pellets within the fuel



elements. Their [28] final model is shown in Figure 13. Several issues with solution convergence were encountered by Williams and Yatabe [28] and originated in the contact dynamics between the pellets, sheath, and endcaps. Changes in contact from the thermal and mechanical loads caused pellets to become unconstrained. By adjusting some parameters, convergence was eventually achieved but in the process demonstrated the complications of modeling fuel pellets [28]. Williams and Yatabe [28] included heat generation and pressure from the coolant in addition to the loading that Soni [27] had used for their model. The heat generation aspect can be seen in Figure 13.

As presented herein, the model does not account for pellet cracking, fission gas, or fuel swelling, but they believe these could be included using the ELESTRES code as a basis [28]. Agreement of the model with others was marginal, since deformation was under-predicted in some instances, suggesting that further analysis of the pellet-sheath gap is required. The model took an average of 12 to 24 hours to be solved with a two core processor while already being simplified through symmetry [28]. This immediately draws concern to the feasibility of translating this work into a full 37-element bundle. Encountering these issues with only 15 pellets when there are 30 pellets in a single fuel element and more than 1000 pellets in a full bundle, indicates computational demand would be significant for a complete model [8]. In spite of its limitations, this iteration of a single fuel element was an important step towards a full 3D bundle model. Notably, it highlighted the future difficulties that will be encountered when building a full 37-element fuel bundle with pellets.

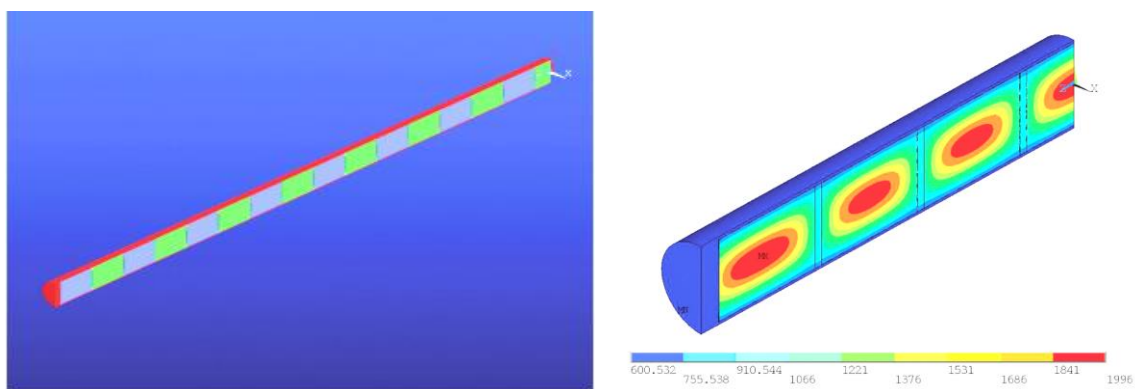


Figure 13: Williams' and Yatabe's [28] Single Fuel Element Model Including Pellets and Heat Generation – Temperatures in °C

In terms of full bundle models that have been published, Bell and Lewis [29] developed a COMSOL Multiphysics™ model in 2012 as an expansion and modern improvement to the BOW code. The model was able to represent the whole bundle including the end plates but it consisted entirely of simplified beam elements [29]. Despite this simplification, this study represented a significant step to being able to better identify the combined deformation effects of multiple elements in one model. The ability to concurrently view the deformation of multiple elements was an important development for analyzing subchannel geometry changes and the impact on coolant flow. The construction of this model in COMSOL Multiphysics™ is shown below in Figure 14.

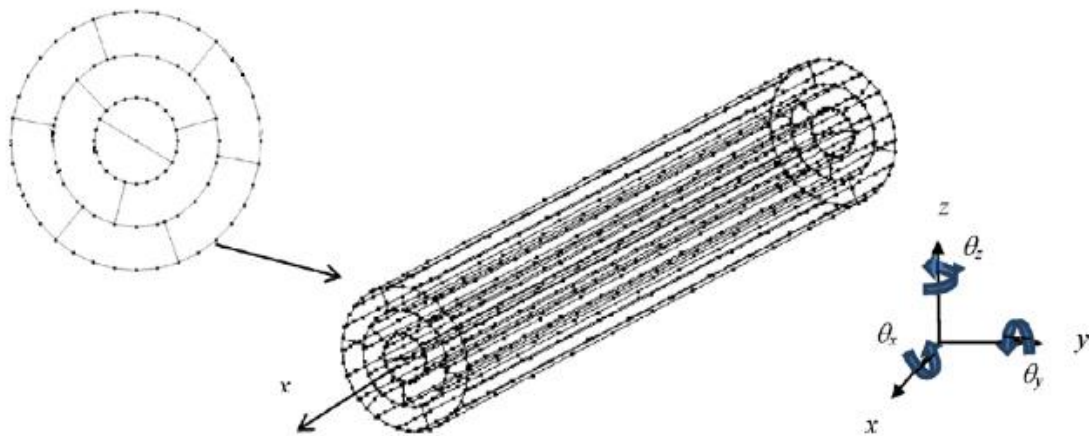


Figure 14: Bell and Lewis Beam Modeling of 37-Element CANDU® Fuel Bundle [Adapted from 29]

Bell and Lewis's [29] model is in agreement with both the BOW code and experiments conducted outside of the reactor on unirradiated single fuel elements. However, this model is limited by a few aspects. The first is that it conservatively neglects the midplane spacer pads of the bundle that are designed to prevent the elements from contacting each other at large deflections [29]. Secondly, even though the end plates are actually represented here, unlike the BOW code, the use of beam elements is not perfectly accurate to the real end plate's geometry. Combined, these factors limit the accuracy of end plate deformation in this model despite the fuel elements showing good agreement with BOW code and experiments.

Lee *et al* [30] was the first to develop a full 37-element bundle model that was geometrically accurate with regards to the real design and the only simplification being the omission of pellets. The many contact pairs between spacer pads, bearing pads, fuel elements, and the pressure tube were included. These contact pairs ensured that all interactions between fuel elements would be accounted for as accurately as possible [30]. The final model represented a significant advancement in bundle modeling and is shown in Figure 15. Lee *et al* [30] used the model to study the effects of pressure tube creep on bundle deformation. The model focused on macro deformation trends instead of specific magnitudes, since the deformation due to creep was simulated by applying incremented forces to the bundle. At the highest loads, this caused significant end plate sag and end plate contact of the pressure tube during the sensitivity analysis. At the highest loads, element-to-element contact at the quarter plane, where there are no spacer pads, was also observed [30]. The model was highly complex and required specialized computing power from CMC Microsystems to be solved in around 15 hours [30]. Thus, adding pellets to Lee *et al*'s [30] model, using an approach such as Williams' single fuel element model with pellets, would certainly create a simulation that would take on the order of days to solve.

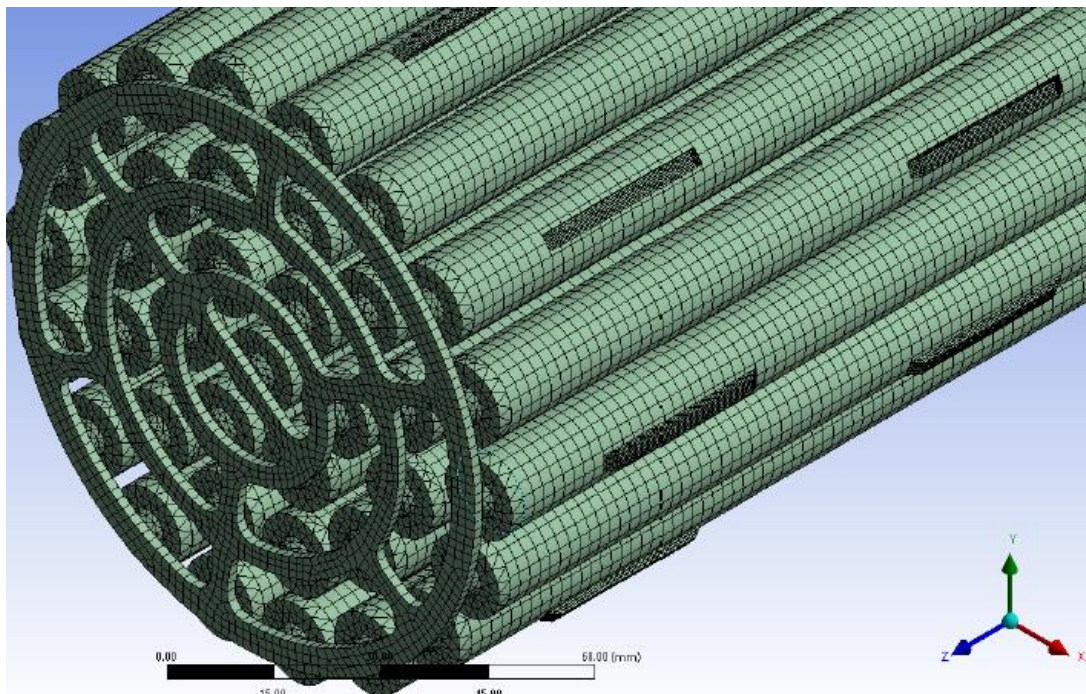


Figure 15: Lee *et al*'s [30] Full Bundle Model Without Pellets

In developing the full bundle model, Lee *et al* [30] also observed that the method by which end plates are constrained played a significant role in the deformation response of the bundle. Fully constraining the end plate face in the axial (Figure 15, Z-Direction) caused extreme bending of fuel elements as they were not allowed to expand axially through deformation of the end plates [30]. Constraining only the webs or specific edges of the end plate in the axial direction resulted in the expected deformation profile seen in experiments [31]. Moreover, it showed that the end plate will deform as the fuel elements bow, creating a wave pattern [30]. The difference in deformation effects between the constraint methodologies is shown in Figure 16. Although the deformation in both images is magnified by a factor of 5, it supports that the end plate plays a significant role in fuel element deflection and merits further investigation.

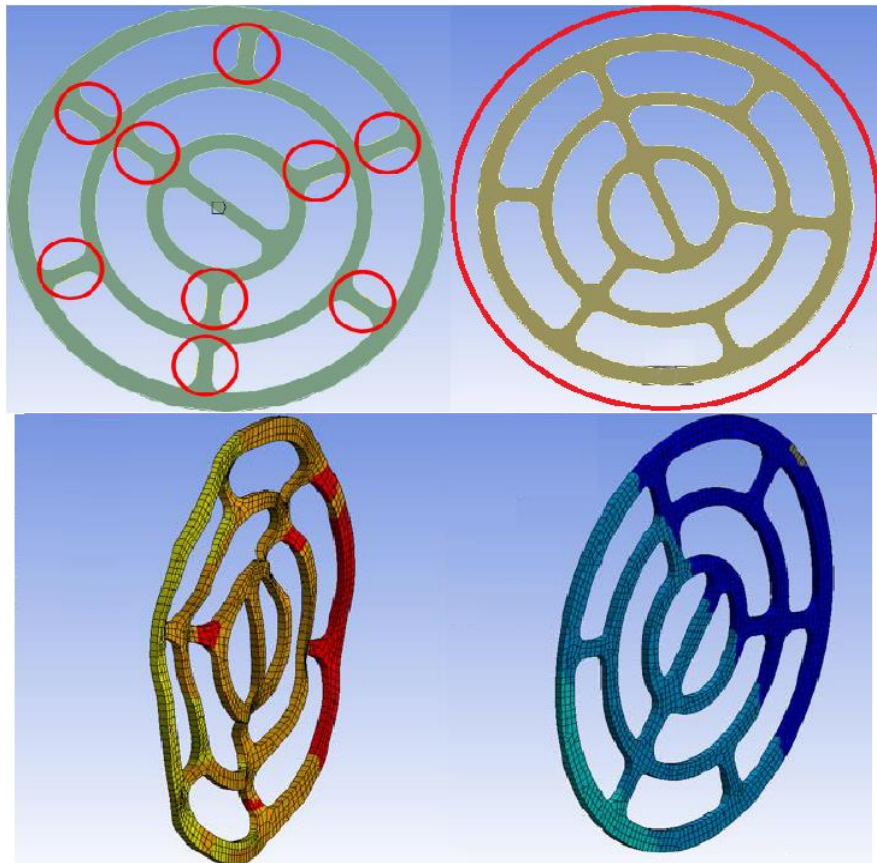


Figure 16: Magnified (5X) End Plate Deformation as Observed by Lee *et al* [30] for End Plates with Axially Fixed Webs (Left) and Axially Fixed Face (Right)



### 3.3 Experimental Studies

Some experimental studies to simulate and quantify bundle deformation in a reactor have been completed. However, they are limited in number due to the expensive materials, radiation hazards, unique testing apparatuses, and other difficulties associated with recreating a reactor environment. Ideally experiments would be completed using the CANDU® reactors themselves but taking one offline to run experiments is not feasible due to electrical grid stability and financial penalties of not producing electricity [18]. The radiation hazards associated with spent fuel also necessitate special handling and transport considerations. Most data is thus collected from experiments completed outside of the reactor environment in labs using replicas and unirradiated fuel bundle components from the manufacturers [27]. Some post-irradiation experiments have been completed by disassembling spent fuel bundles in protective hot cells. However, the data is not perfectly reliable, since bundles must spend time in cooling pools before being sent for analysis [21]. Neither post-irradiation analysis nor experiments completed outside the reactor are without their own issues, but combined they provide a basis to benchmark the accuracy of computer models.

One of the most informative post-irradiation experiments was conducted through the examination of a 37-element bundle that spent two years in a reactor at the Bruce generating station. Bundle G85159W was placed in a high power position where it achieved an exceptionally high burnup of 492 MWh per Kg of Uranium [31]. The deformation effects were minor but fell in line with observations from out of reactor experiments. The fuel elements showed minor amounts of bow with no element-to-element or element-to-pressure tube contact while the end plates experienced two distinct deformation effects [31]. These were the dishing and doming as well as the parallelogram or tilting effect. The dishing and doming effect is believed to be due to hydraulic drag from the coolant flow, whereas the parallelogram effect is attributed to pressure tube sag and differing support provided to the bundle based on the slope of the tube [31]. All of these effects are pictured in Figure 17. The exact magnitudes of deformation cannot be discussed as they are considered to be proprietary information.

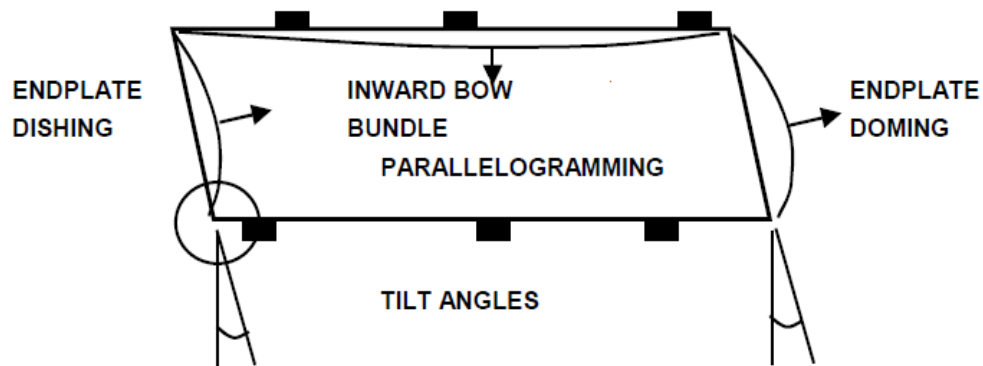


Figure 17: Deformation Trends Observed from Post-Irradiation Analysis [31]

Despite the end plate deformation being noticeable and almost certainly having a relationship to fuel element deflection, it is seldom the focus of modeling studies. The fuel elements have been the primary focus, since they are the components that contain the fuel and need to be cooled and durable enough to prevent fuel failure. It is clear from post-irradiation analysis, however, that the end plate has an impact to bundle deformation that may not be getting enough attention.

## 4. Research Objective

With the majority of CANDU® bundle modeling focused on the deflection and bow of fuel elements, the end plates have received less attention and mostly been modeled as idealized boundary conditions for fuel elements. This does not allow rotation at the ends of fuel elements and can result in non-conservative predictions of deformation, since they are represented as having fixed ends. The flexibility of the end plate has seldom been properly represented with sufficient freedom of movement or reactor accurate boundary conditions. As a result, end plate deformation characteristics seem to have only been discovered through post-irradiation experiments or as an inference from studying fuel elements. Being the primary structure holding the bundles together, the effect end plates have in deformation of a fuel bundle is believed to be more significant than the majority of models have revealed. The end plates receive a pressure and drag load from coolant flow, localized bending moments at the fuel element connections, and are subject to creep under these applied loads just like the rest of the bundle [8]. Any loads imparted on the end plate will be transferred directly to the fuel elements through their welded connection and vice versa; thus the two components must deform together. Accurate modeling of the end plate as well as the fuel element connections is perceived to be integral to the continuing development of fuel bundle models.

This thesis used a series of Finite Element models constructed using the software ANSYS™ to examine how end plate orientation, thickness, connections, loading, and boundary conditions affect bundle deformation. The goals were to advance and refine the models developed by RMC [27][30] while garnering a more thorough understanding of end plate interaction with fuel elements and the associated deformation effects. Modeling aspects including contact, element type, and geometry for modeling end plates were all evaluated. The applied loads were consistent with Normal Operating Conditions (NOC). This kept deformation magnitudes in line with post-irradiation data and relevant to the effects expected to be experienced by the average bundle at the time it exits the reactor. Coupled with RMC's existing research [27][30], the results of this study further advance CANDU® fuel bundle modeling and the industry's understanding of specific deformation effects.

## **5. Methods and Research Approach**

This study was broken down into three phases. These phases are the development and comparison of the model to experimental data, an in depth evaluation of the end plate effects in bundle deformation, and a final analysis that considers the sensitivity of end plate deformation to specific geometric factors. This section outlines the purpose and methods associated with each phase of the study.

### **5.1 Model Development and Benchmarking**

The first phase was the development of a bundle model consistent with experimental post-irradiation data and expected deformation profiles. Before studying end plate deformation specifically, it was first necessary to have a model loaded and deforming in a manner expected for a bundle at NOC. The goals of this phase were to establish material properties and compare the effects of boundary conditions, thermal profiles, and mechanical loads. Mechanical loads included gravity from the bundle's own weight and axial pressure from coolant flow, while thermal profiles were applied to incorporate creep and expansion from the heat generated by fission. Boundary conditions were selected with accuracy to the reactor environment and architecture being the most important consideration. The boundary conditions that received the most focus were the bearing pads and their interface with the pressure tube as well as the end plates and how they contact other bundles or the ends of the fuel channel. Once a full model was developed with working boundary conditions and all load factors incorporated, it was compared to existing data for benchmarking. Successful benchmarking was based upon the models accuracy to studies by Soni [27], Lee et al [30], and available experimental data [31].

### **5.2 Analysis of End Plate Deformation Effects**

With a full model developed in the first phase, the second phase was an investigation into how the end plate deforms, and how end plate deformation affects the rest of the bundle. An evaluation of bundle deformation effects from coolant pressure, differential thermal expansion, and pellet weight was



completed using the model developed in the first phase. Specific contributions to bending, twisting, dishing, and doming of the end plate were observed.

### **5.3 End Plate Deformation Sensitivity Analysis**

#### **5.3.1 Bundle Orientation**

The first component of the sensitivity analysis was a study on how the orientation of the end plate affects the deformation profile of both the whole bundle and the end plate. The bundle's end plate does not have perfect rotational symmetry and is only symmetric every 120 degrees. As a result, different orientations of the end plate webbing with respect to gravity were hypothesized to have some, if even a minor, effect on deformation. If one of the major webs was not perfectly vertical this was expected to increase vertical compression of the end plate since there is less direct resistance to the weight of the bundle in that orientation. To support this idea, the developed model was evaluated through 120 degrees of end plate rotation to determine if controlling bundle orientation had the potential to reduce stress and deformation.

#### **5.3.2 End Plate Thickness**

The second component of the sensitivity analysis was an evaluation of the impact to deformation by increasing the thickness of the end plates. A thicker end plate has been considered as an improvement to the existing design because of end plate cracking observations in irradiated bundles [32]. A thicker end plate is expected to mitigate stresses because of the increased stiffness from the added material. Reduced bending in the end plate from the increased thickness may also have a feedback effect that reduces deflection of the fuel elements. To complete this study, the developed model was modified to have an end plate with up to double the nominal thickness. It was then subjected to established loadings from the first phase to determine if there were notable advantages to the modification with respect to deformation at NOC.

## 6. Theory

### 6.1 Principles of Finite Element Analysis

This section provides a brief overview of the theory behind FEA and why it was used to study end plates in CANDU<sup>®</sup> bundle deformation. FEA is a numerical method used to simplify and solve boundary value based engineering problems in many fields including structural mechanics, fluid mechanics, and heat transfer [33]. Applicable problems involve a structure or geometry that is too complex to solve using first principles calculations for stress, strain, or temperature. FEA can solve for these variables for a nearly infinite range of geometries and at not just specific points, but throughout the whole system. This is accomplished by discretizing complex geometries into smaller parts known as elements, and treating the variable of interest as a field variable to be solved in each element. Elements are easier to represent mathematically since they take the form of simple geometric shapes that can be 1D, 2D, or 3D in nature. Loads can then be transmitted between these elements to determine the value of the field variable throughout the geometry [33]. The most common FEA elements are shown below in Figure 18.

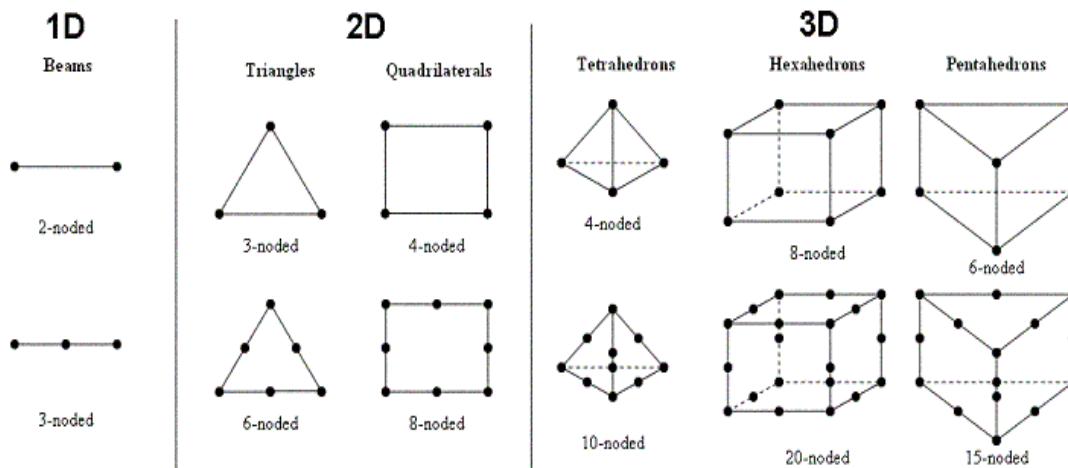


Figure 18: Types of Elements used to Discretize Geometries for FEA [34]

The combination of elements to form the original geometry is known as the mesh; one of the most important aspects of FEA. The size of the mesh along

with the type and number of elements determines how well the original geometry is reflected in the discretization. Naturally, some elements are better at mapping certain surfaces. For example, in solid geometries tetrahedrons work well to map curved surfaces, but are computationally burdensome in large rectangular bodies. Hexahedrons, however, can fill a rectangular space with fewer elements while more accurately mapping the shape [35]. The importance of mesh accuracy is also why some of the elements in Figure 18 have midpoint nodes. In the case of hexahedrons the midpoint node allows the element to moderately map curved surfaces in a way that normal hexahedrons cannot [35]. To highlight the importance of mesh refinement when discretizing a geometry, Figure 19 shows how a reduction in mesh sizing with tetrahedrons improves the accuracy of a curve. Adjusting the mesh to map the geometry is therefore related to accuracy of the results.

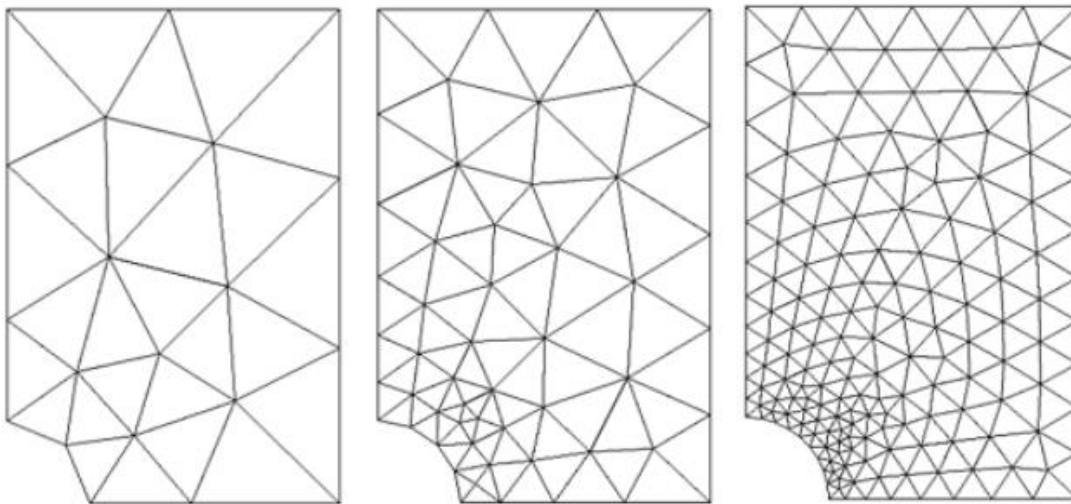


Figure 19: Impact of Mesh Refinement on Recreating Curved Geometries [36]

The most accurate results would be determined with an infinitely refined mesh, however this is not practical due to the exponential increase in computational load. As a result, mesh refinement is best used only at the areas of interest or where maximum and minimum values of the field variable are expected [35]. Furthermore, the results produced by mesh refinement will eventually reach an asymptote, where further refinement has a negligible improvement on the model's accuracy. Such a mesh is considered to have achieved convergence,

indicating when an acceptable mesh has been reached [35]. For this fuel bundle model, mesh convergence was studied for the end plate and fuel elements.

The solution to the field variable throughout the finite element mesh is computed using polynomial equations, which are derived from material properties, element shapes, and boundary conditions. In the case of structural models the formulation of these polynomials is represented by the following equation where  $\{F\}$  represents the force vector,  $[K]$  the stiffness matrix derived from material properties and element shapes, and  $\{U\}$  the displacement vector [35].

$$\{F\} = [K]\{U\} \quad (1)$$

In this equation either force or displacement can be chosen as the field variable and calculated by defining the opposing value through boundary conditions. This means that displacements can be calculated from forces or forces can be calculated from displacements. The stiffness matrix is the essential part of the equation defining the finite element method. The matrix is formulated using either the Galerkin Method or Principle of Minimum Potential Energy [35]. It generates a system of equations that relates nodes and elements to one another through the field variable using shape functions and material properties. Depending on the model and mesh size, the resulting system of equations can number in the millions, which is why FEA makes use of computers. Solving this system of equations is contingent on sufficient boundary conditions being defined for each degree of freedom in the field variable. If there are insufficient boundary conditions then the resulting system of equations becomes underdetermined and the model is not solvable [35]. In 3D structural models when displacement is the field variable, boundary conditions must be defined such that displacement in the X, Y, and Z axis are known in at least one location in the model.

Establishing boundary conditions is a key aspect of FEA model development and often the greatest source of error. They must be defined even if it requires diverging from the system's true design conditions. For example, even though contact between components may be frictional in the true system, an FEA model may require that contact to be fixed and immovable to sufficiently reduce the degrees of freedom and allow the model to solve. This is particularly relevant to the contact between bearing pads and the supporting pressure tube for fuel bundle models. Despite this limitation, clever model construction can sometimes work around this problem to limit this as a source of error.

Once the system of equations generated by Equation (1) is solved, the results can be converted into a graphical output. Properties derived from the field variable, such as stress in structural models, can then be displayed throughout the geometry. The graphical output assigns colours to each element based on a scale for the variable of interest. An example of FEA graphic output is provided in Figure 20.

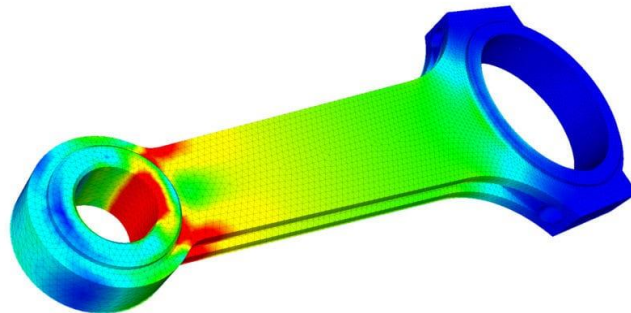


Figure 20: Example of Graphical Output from FEA Software [37]

When using FEA in other types of engineering problems the form of Equation (1) and the method of generating the system of equations remains the same but the variables change. In the case of thermal systems, which are also used in this study, force vectors and displacements are replaced by heat generation and temperature while the stiffness matrix becomes a thermal conductivity matrix. This flexibility allows FEA to be used in a large breadth of engineering problems and is why it is an excellent option for studying CANDU® fuel bundle deformation.

## 6.2 Nonlinear Finite Element Models

The previous section defined finite element analysis for a linear approach but there are many situations where a nonlinear analysis may be required. These include models that experience a change in material properties, contact between different bodies, or large deformations that distort the geometry [35]. A fuel bundle model must be nonlinear due to contact and changes in strain rates from

creep. Contact occurs where the bearing pads rest on the pressure tube and between the spacer pads of the fuel elements. The transfer of forces through both types of pads influences deformation shape and so modeling this interaction is important. Creep must also be included, since it is the main cause of bundle deformation [31]. The nominal forces from fuel pellet weight and coolant flow are not enough to plastically deform the bundle on their own, thus an accurate model needs to include creep as would be experienced by a real bundle. In FEA, both contact and creep result in a constant change of element stiffness and material properties. With respect to Equation (1) this changes the stiffness matrix with every increase in deformation. The changing stiffness matrix results in nonlinearity, requiring the model to be solved iteratively. Equation (1) therefore becomes Equation (2) when the problem is nonlinear [35].

$$\{F_n\} = [K(U_{n-1})]\{U_n\} \quad (2)$$

In this equation, the stiffness matrix is a function of the displacement values from the previous load step. As a result, an iterative approach to find the new displacement is required. Most FEA programs will use the Newton-Raphson Method to approximate a linear solution to the nonlinear problem. The Newton-Raphson method is an iterative algorithm that uses first derivatives to determine the roots of a function from an initial estimate [33]. Graphically, the iteration process takes the form of Figure 21. The blue lines represent the converging linear approximation to the nonlinear function represented by the pink line. Eventually the linear approximation will be tangent to the function at the point it passes through the root on the axis, which is when the solution is considered to be found [38]. In the case of FEA, the nonlinear function is Equation (2) with  $\{F\}$  on the y-axis and  $\{U\}$  on the x-axis. There is one caveat to the Newton-Raphson algorithm, however, in that the initial estimate to satisfy the equation must be relatively close to the true value or convergence will not occur [38]. This poses an issue when there are large forces or displacements in the model.

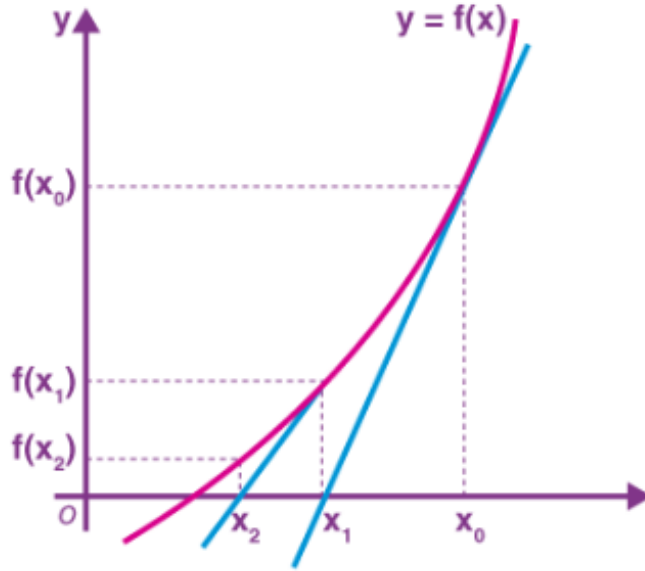


Figure 21: Graphical Representation of the Newton-Raphson Method [38]

If deformations or forces are large, it is seldom possible to achieve convergence through a single pass of the Newton-Raphson algorithm. The difference between the linear approximation and function becomes too large, making it difficult to determine an initial estimate for the solution. To resolve this problem, load substeps are used to reduce the amount of deformation in each pass of the algorithm [35]. The use of load steps was integral to the development of the bundle models since multiple loads and load surfaces between pellet weight, coolant forces, and temperature needed to be applied. By breaking this complex loading down into substeps, the amount of deformation was reduced in each step making it easier for the algorithm to converge on a solution.

Modeling CANDU<sup>®</sup> bundle geometry and the interaction between fuel elements, end plates, and the pressure tube is not easily simplified. Although deformation of specific aspects of the bundle, like individual fuel elements, could have been estimated using solid mechanics, deformation of the whole bundle cannot be predicted this way. FEA was therefore a powerful tool for this study because of its ability to accurately map the full bundle geometry but also incorporate multiple physical phenomena.

### 6.3 Finite Element Analysis and Computers

Since the formulation of a problem through FEA essentially creates a large matrix with many equations that need to be solved collectively, computers are a significant asset. Problems with thousands or even hundreds of thousands of equations can take a long time to be solved with the types of Central Processing Units (CPU) and amounts of Random-Access Memory (RAM) found in everyday computers. Thus specialized computing hardware is frequently talked about in FEA studies when dealing with large models. CPUs and RAM both determine how fast a problem can be solved, but RAM is often the limiting factor because it is responsible for storing the short-term data produced in the process of solving the equations [35]. The more equations and larger the model, the more RAM is needed to store the short-term data. Therefore between a CPU and RAM, the amount of available RAM will determine if the FEA problem can be solved from a hardware perspective. A smaller CPU will still solve the same problem as large CPU, but will simply take a longer amount of time.

To achieve sufficient amounts of RAM as well as CPU speed in solving FEA models, many users turn to specialized computing hardware. Companies such as CMC microsystems offer remote access to high end CPUs and large amounts of RAM through cloud services. These services were made available for this thesis but were seldom used. The intent was to keep the final model of a size that could be run in a reasonable time with the type of computer platform available to the average person. Accordingly, the models in this thesis were all run using a computer with a 6 Core Ryzen 3600X processor at 4.0 GHz and 32 GB of RAM at 3200 MHz. This combination proved more than capable for all models except those with the smallest mesh sizes in the mesh convergence study. Solution times for the final model used in benchmarking against experimental data required an average solution time of 6 Hrs with 950,000 nodes.



## 7. Model Development and Benchmarking

The first step of this analysis was to construct and benchmark a model that could be used to examine the effects that the end plates have on bundle deformation. This required a model that could predict the overall deformed shape at NOC. Model development was completed in stages and started with the individual bundle components of fuel elements and end plates. At each stage the effects of boundary conditions, thermal profiles, mechanical loads, and finite element mesh were studied. Being able to achieve expected deformation profiles was considered equally important to doing so with loads reflective of the true reactor environment. For example, even though a point load or boundary condition on a specific fuel element may have aided in achieving a desired deformation effect, it was not accepted in the final model if it was not comparable with known loads from the reactor.

### 7.1 Material Properties

Aside from the uranium dioxide fuel, the sole material used in the construction of CANDU® fuel bundles is Zircaloy-4. The properties of Zircaloy-4 are well known due to various experiments and its widespread use as cladding material in different reactors [8]. For this thesis, the properties of Zircaloy-4 were derived from MATPRO, a materials database developed by INL for studying nuclear fuels. MATPRO not only has nominal properties for Zircaloy and its many alloys, but also contains a series of codes for determining properties with consideration for the effects of cold work, oxidation, irradiation and temperature changes. Only changes in material properties from temperature are considered in this model, because impacts from the other factors add a layer of complexity that is both beyond the scope of the current work and not easily incorporated into ANSYS. Furthermore, it was hypothesized that incorporating the other factors would only have an effect on the magnitude of deformation and not the bundle's deformation trends or shape.

The properties and values as derived from MATPRO, and entered into ANSYS for Zircaloy-4 are presented in Table 1. All of these values were assumed to be isotropic in that they are the same in all directions within the material, even though Zircaloy tubing has been found to have anisotropic properties, differing between the longitudinal and radial axis [39]. The difference in properties is

dependent upon the extrusion and heat treatment process used during manufacturing, for which the specifics of CANDU® bundles are not widely available. Fortunately, in most cases the difference in directional properties is small enough that they can be conservatively neglected. Accordingly, this analysis opted to simplify the material properties of Zircaloy-4 by assuming them to be isotropic [39].

Table 1: Zircaloy-4 Properties at Various Temperatures from MATPRO [39]

Temperature (Celsius)	Elastic Modulus (GPa)	Poisson Ratio	Thermal Conductivity W/m°C	Coefficient of Thermal Expansion $\mu\text{m}/\text{m}^\circ\text{C}$
20	92.77	0.3	12.58	7
300	74.72	0.3	16.16	7
400	71.99	0.3	17.35	7
500	66.52	0.3	18.55	7
600	61.05	0.3	19.81	7

When simulating creep, only thermally induced creep was applied to the models. Irradiation creep was not considered because there is little experimental data available on which to base it. Thermal creep was implemented using the Norton Creep Law [40].

$$\epsilon_{\text{Creep}} = C_1 \sigma^{C_2} e^{-\frac{C_3}{T}} \quad (3)$$

Values for  $C_2$  and  $C_3$  were used directly from empirical data [41], while the value of  $C_1$  was logarithmically adjusted from the empirical data to find the fastest creep rate that still created a stable model. The empirical values along with those used in ANSYS™ are provided in Table 2. The three constants,  $C_1$ ,  $C_2$ , and  $C_3$  are associated with factors that affect creep rate in relation to stress in the material  $\sigma$ , and temperature,  $T$ . Through Equation 3 they are used to determine the strain or creep rate ( $\epsilon_{\text{Creep}}$ ) in the model. The three constants come from the activation energy to initiate creep along with whether that creep is a result of diffusion or dislocation movement within the material [41].

Table 2: Zircaloy-4 Creep Constants for Accelerated Deformation Rate [41]

	$C_1$	$C_2$	$C_3$
Constants Used in this Study	$2.1 \times 10^{-22}$	5	30,000
Empirical Constants	$2.1 \times 10^5$	5	30,000

An adjusted creep rate was necessary for two reasons. The first was that achieving the expected creep deformation in a model using timelines equivalent to a real bundle was highly impractical. Bundles reside in the reactor for 6 to 24 months and simulating this amount of creep time at a 1:1 ratio was not conducive to achieving results in a reasonable timeframe [8]. The second reason was that creep data is highly specific to the circumstances of the experiment, which are never perfectly accurate to the reactor environment. Differences in applied load and temperature have been seen to cause large differences in the derived creep constants [41]. This means constants derived from one experiment often have difficulty being reconciled with the results of another. Since the Norton Creep Law ultimately simplifies to the rate at which materials deform for a given stress, it was assessed that adjusting the  $C_1$  constant from empirical data was an acceptable decision to obtain more practical simulation times [40]. Changing the  $C_1$  constant was therefore assumed to only affect deformation magnitudes based on the creep time and not affect the resultant shape of the deformed bundle or end plate. This was confirmed in a later study in this thesis and is discussed in 7.5.2.

Having diverged from the empirical  $C_1$  constant, a creep duration equivalent to 6 to 24 months of residency inside the reactor was not obvious. As a result, an approximate duration was established for benchmarking against experimental data [31] using key characteristics observed in the deformed shape of an irradiated bundle. This is elaborated on in further detail in Section 7.6.2.

## 7.2 Bundle and Fuel Element Temperature Profiles

The variation in neutron flux and flow of coolant around the bundle results in an uneven temperature distribution in both the axial and radial directions. The elements in the outer ring of the bundle operate at the highest power, being

exposed to the highest relative neutron flux. Towards the center of the bundle, however, the element power and neutron flux decreases due to the amount of surrounding fuel that results in a localized increase in neutron absorption [42]. A secondary uneven power profile is also observed along the length of each fuel element due to a phenomenon known as end flux peaking. This results in higher neutron flux at the ends of the elements near the end plates and is caused by reduced neutron absorption at that location [43]. The average linear power of fuel elements depending on their location in the bundle along with their corresponding end flux peaking factor is shown in Table 3.

Table 3: End Flux Peaking Factors and Linear Element Powers [42] [43]

<b>Fuel Element Location</b>	<b>Linear Element Power (kW/m)</b>	<b>End Flux Peaking Factor</b>	<b>Expected Element End Power from Peaking Factor</b>
Outer Ring (18 Elements)	51	1.142	58
Intermediate Ring (12 Elements)	41	1.205	49
Inner Ring (6 Elements)	36	1.246	45
Center (1 Element)	35	1.268	44

In addition to the differences in axial and radial power throughout the bundle, disproportionate heat transfer and coolant flow also affects the temperature profile. The outer elements receive the greatest cooling effect due to lower flow resistance in the gaps between the pressure tube and bundle. The inter-element sub channels receive comparatively less flow, and therefore less efficient heat transfer. When combined, the differences in axial power, radial power, and coolant flow create higher temperatures at the center and ends of the bundle [44]. This difference in temperature profile is believed to affect bundle deformation by changing material properties and creating stresses through differential thermal expansion. Including an approximation of this temperature profile was thus considered an important aspect of model development.

An exact temperature profile for 37-Element CANDU® fuel bundles could not be ascertained from literature. Therefore, the data in Table 3 along with an

assumption of a 10°C increase between each successive ring of fuel elements was used as an estimate [44]. The resulting temperature profile is presented in Figure 22. A temperature of 300°C based on the average D<sub>2</sub>O coolant temperature was used as a baseline for the outer fuel elements, which receive the best heat transfer [8]. The data in Table 2 was then used to estimate temperatures throughout the rest of the bundle, since element power is well correlated with temperature [21].

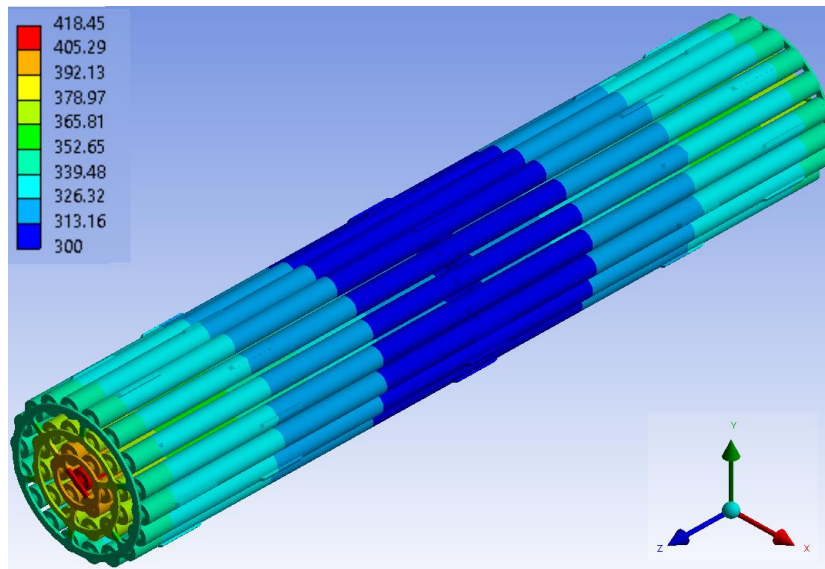


Figure 22: 37-Element Bundle End Flux Peaking Temperature Profile (°C)

### 7.3 Mechanical Loads – Pellets, Weight, and Coolant Forces

The mechanical loads on the bundle can be divided into two main forces. These are the weight of the bundle and the axial forces from coolant flow. The weight of the bundle, composed of the fuel and cladding, is perpendicular to the fuel elements and in the direction of gravity. The coolant forces are imparted axially against the end plates face and length of the bundle. To approximate the force resulting from the weight of fuel and cladding, the density and volume of the two materials in the bundle was converted to a force using gravity of 9.8 N/kg. Neglecting the small gaps left in the fuel elements for thermal expansion, this estimates the bundle's overall mass at approximately 24.3 kg with a weight of 238.1 N. This is equivalent to a weight of 6.5 N per fuel element, and is the value

used for individual fuel element weight in this analysis. These calculations were completed using official dimensions for 37-Element CANDU® Fuel Bundles [45].

With respect to including pellets in the fuel elements, the initial preference was to exclude them from the model entirely. As detailed in Section 3, modeling fuel pellets has proven to be exceedingly difficult. The fuel pellets impart a stiffening effect on the fuel elements that increases with irradiation. Swelling and grain growth in the pellets increases the stiffness of the fuel elements at higher burnups, giving them progressively greater resistance to deformation [21]. Furthermore, the spatial differences in neutron flux that affect temperature profiles also cause some pellets to be irradiated faster than others. This means the change in pellet properties is not uniform for the whole bundle and is dependent upon where the fuel elements are in the bundle and where the bundle is in the reactor [21]. The constant and disproportionate change in fuel pellet properties and the associated stiffening effect is computationally prohibitive for this model. There is also no known empirical data to use as a basis. Between the need for a high number of assumptions, modeling complexity, and a proven record for being computationally onerous, the initial preference was to exclude pellets from the model.

Before discussing loads from coolant flow it is important to provide some context for the positional nomenclature. When the term upstream is used, this refers to the end of the bundle towards the inlet pipe where the coolant is entering the pressure tube and pushes against the bundle. Downstream refers to the opposite end of the bundle that is closer to the outlet pipe where coolant exits the pressure tube after removing heat from the fuel bundles.

There are two separate forces on the bundle from coolant flow, which are the dynamic pressure on the upstream end plate and the drag force over the whole bundle. The dynamic pressure loading is assumed to be the same for each bundle, since they have the same amount of surface area with perpendicular exposure to coolant flow. The resultant force is assumed to be translated through contact of adjacent end plates and not increase over the length of the fuel channel. This means each bundle would be exposed to the same amount of dynamic pressure regardless of position in the fuel channel. The drag force, however, is assumed to increase linearly with each successive downstream bundle as the drag from the upstream bundles is transferred down the length of the fuel string. For example, the first bundle only receives drag loading from its

own surface area whereas the last bundle receives drag loading from not only its own surface area but that of all the previous bundles too. This means the drag force is dependent on the bundle's position and increases over its life in the reactor as it moves further down the fuel channel. Without knowing how long bundles reside in each position, the average drag loading becomes difficult to quantify. It was therefore decided that there were too many unknowns for drag force to be approximated, so it was excluded from the model. The dynamic pressure loading on the upstream end plate was the only axial load considered for the model and is estimated below using data from CANDU® 6 reactors.

### 7.3.1 Estimation of Coolant Dynamic Pressure

Pressure Tube Inner Diameter ( $T_{ID}$ ): 104 mm [46]

Coolant Mass Flow Rate ( $\dot{m}$ ): 24 kg/s [46]

Density of ( $D_2O$ ) Heavy Water ( $\rho_{Coolant}$ ): 1110 kg/m<sup>3</sup> [46]

Cross Sectional Area of Pressure Tube:

$$A_{PT} = \pi \left( \frac{T_{ID}}{2} \right)^2 \quad (4)$$

$$A_{PT} = \pi \left( \frac{104 \text{ mm}}{2} \right)^2 = 8495 \text{ mm}^2$$

Coolant Velocity:

$$V_{Coolant} = \frac{\dot{m}}{(\rho_{Coolant})(A_{PT})} \quad (5)$$

$$V_{Coolant} = \frac{(24 \frac{\text{kg}}{\text{s}})}{(1.11 \times 10^{-6} \frac{\text{kg}}{\text{mm}^3})(8495 \text{ mm}^2)} = 2.5 \frac{\text{m}}{\text{s}}$$

Coolant Dynamic Pressure:

$$P_{Coolant} = \frac{1}{2} (\rho_{Coolant})(V_{Coolant})^2 \quad (6)$$

$$P_{Coolant} = \frac{1}{2} (1110 \frac{\text{kg}}{\text{m}^3})(2.5 \frac{\text{m}}{\text{s}})^2 \approx 3600 \text{ Pa}$$

## 7.4 Single Outer Fuel Element Models

Individual fuel elements are the core component of the CANDU® bundle, so an accurate deformation profile for a whole bundle is first dependent upon modeling of the fuel elements. The outer fuel elements in particular, have a key boundary condition in that their bearing pads are the only point of contact between the bundle and supporting pressure tube. The contact between these bearing pads and the pressure tube is integral to how and where loads are transmitted in the bundle to cause deformation. Therefore, outer fuel elements are an ideal starting point for the development of a full bundle model. Lee *et al* [30] completed an analysis for individual fuel elements and revealed that bonding the center bearing pad to the pressure tube, while axially constraining the ends was the ideal approach. They also determined that thermal gradients were important in achieving the expected “S” shape deflection pattern observed in experiments [30]. These are valuable conclusions that translate well to this thesis. However, Lee *et al*'s [30] study would have benefitted from further exploration of a few factors that are evaluated in this Section.

The first is that bonding the center bearing pad is an idealized constraint to aid in solving the model, but not accurate to how the bundle interacts with the pressure tube. In reality the bearing pads rest on the pressure tube and are only frictionally constrained. Bonding them to the pressure tube limits fuel element bowing by not allowing bearing pads to move into and out of contact with the pressure tube. This is not an accurate representation since the fuel bundles are not glued and merely rest on the pressure tube. The feasibility of having only frictional constraints between the bearing pads and pressure tube is therefore explored in this section. The second factor requiring more attention is the nature of the temperature profile applied to the fuel elements. Lee *et al*'s [30] study used a constant temperature and a basic thermal gradient with one end of the fuel element being hotter than the other; neither of these approaches are perfectly accurate. A thermal gradient is known to occur across the length of the fuel channel but occurs at a smaller scale along individual bundles [21]. Additionally, the phenomenon of end flux peaking creates hotspots at either end of the fuel bundle, which was not considered. Accordingly, a symmetric temperature profile including end flux peaking was also evaluated.



### 7.4.1 Bearing Pad Boundary Conditions

To complete the study on bearing pad boundary conditions, a hollow outer fuel element model was constructed based on Ontario Hydro 37-Element CANDU® Fuel bundles with staggered bearing pads. Again, the use of hollow fuel elements was preferred from the outset due to the additional computation load that would be required from modeling pellets. An initial mesh sizing of 2 mm based on mesh convergence observations from Lee *et al* [30] yielded a model with 6824 elements. This outer fuel element model was then placed in contact with a half pressure tube section and subjected to creep at a constant temperature of 300°C with the 6.5 N pellet weight derived in Section 7.3. The decision was made to use a half pressure tube section for both the single element and later full bundle models since contact between the bundle and top of the tube has never been observed. As such, removing the top half of the tube is an easy way to reduce computational load by thousands of nodes without significantly affecting results. The resultant half pressure tube and outer fuel element model is presented in Figure 23. The three bearing pads are identified in red with 1 corresponding to the outer bearing pad, 2 the center bearing pad, and 3 the inner bearing pad.

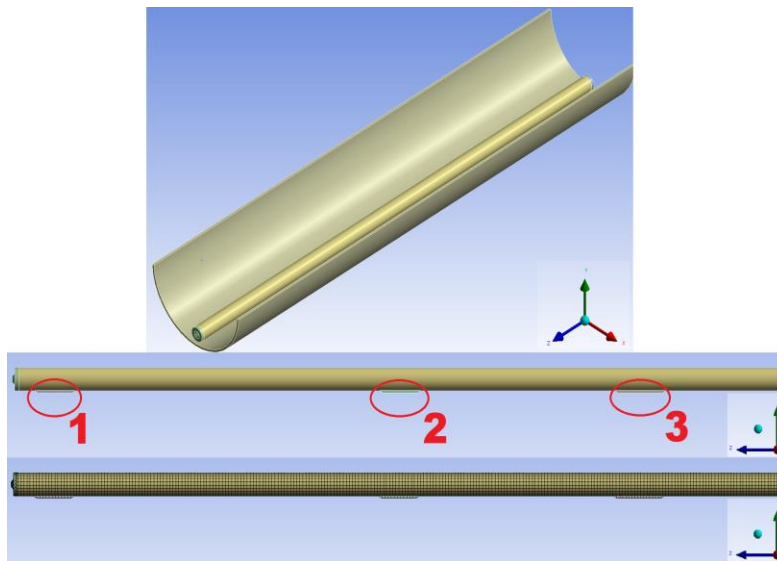


Figure 23: Single Outer Fuel Element and Pressure Tube Model

A comparison between the effects of bonding and not bonding the center bearing pad to the pressure tube was then completed. In Figure 24 the center bearing

pad is bonded while the inner and outer bearing pads have only frictional contact and are allowed to tilt and lift-off of the pressure tube. In Figure 25 the center bearing pad is not bonded and all three bearing pads have frictional contact with the pressure tube, allowing them to move into and out of contact. When bearing pads are in frictional contact with the pressure tube a friction coefficient of 0.1 was used based on fuel bundle modeling research conducted by AECL that deemed the value appropriate for Zircaloy-4 [47].

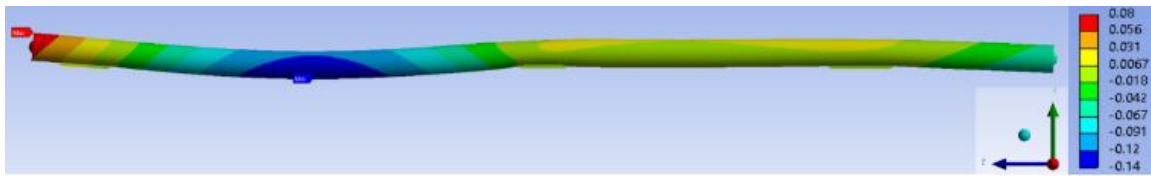


Figure 24: Vertical deformation of an Outer Fuel Element at 300 °C with Pellet Weight, Creep, and Bonded contact between the Center Bearing Pad and Pressure Tube (mm, 50X Magnification)

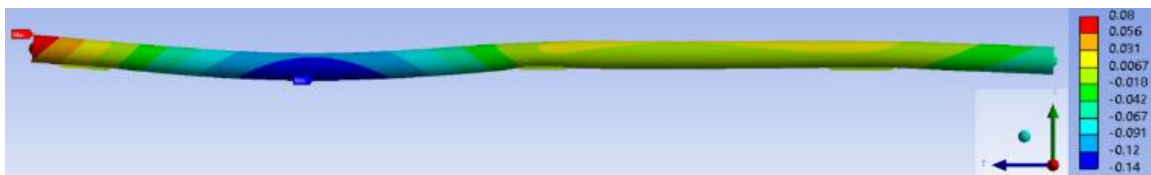


Figure 25: Vertical deformation of an Outer Fuel Element at 300 °C with Pellet Weight, Creep, and Unbonded (Frictional) contact between the Center Bearing Pad and Pressure Tube (mm, 50X Magnification)

Using only frictional contact between the bearing pads and pressure tube results in a near negligible difference in the overall deformed shape compared with bonding the center bearing pad. The “S” shape deflection that Lee *et al* [30] identified as a key correlation to single element heat up experiments is maintained in both models. One notable difference is that the vertical deformation for the frictional model was slightly less than that of the model with the bonded center bearing pad. This is believed to be due to the increased restriction of movement from the bonded bearing pad, which increases the effects of thermal expansion at the ends of the fuel element. When all bearing pads are only in frictional contact with the pressure tube the thermal expansion is

more uniform and also results in a more even distribution of force over the bearing pads. This ultimately results in more deformation at the fuel element ends when the center bearing pad is bonded. Contact of the center bearing pad is also observed to change from sliding to being partially separated when it is not bonded to the pressure tube. This indicates that upward bowing of the fuel element is likely to occur in a full bundle model, which was observed in post-irradiation data [31]. These results confirm that not bonding the center bearing pad to the pressure tube is the more realistic boundary condition. It was therefore adopted for the rest of the models.

## 7.4.2 Temperature Profiles

Having adopted the use of only frictional contact between the outer fuel element bearing pads and pressure tube, the next factor to evaluate was the effect of end flux peaking and the associated temperature profile. The same model from Section 7.4.1 was given a temperature profile based on the end flux peaking factors from Table 2 and the assumptions made to develop Figure 22. This gave the outer fuel element model a midplane temperature of 300 °C and an endcap temperature of 343 °C as depicted in Figure 26.

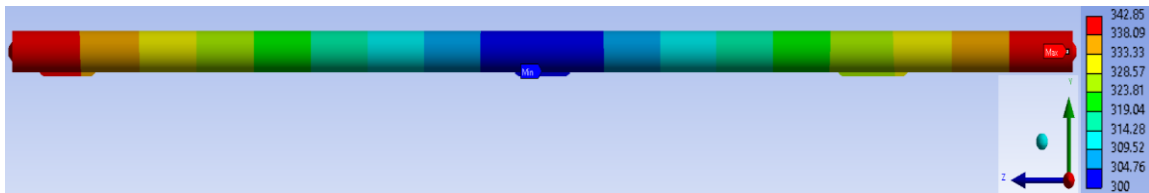


Figure 26: Outer Fuel Element End Flux Peaking Temperature Profile

Temperature differences primarily impact deformation when a body's ability to expand is restricted or creep effects are applied [35]. Accordingly, this section evaluates the temperature effects from end flux peaking profiles with respect to both factors. To evaluate the impact from restricting expansion, two separate comparisons were completed; one with endcaps free to expand and move in all directions and a second with axially constrained endcaps in the Z-Axis. The second comparison is deemed to be more accurate with respect to the boundary conditions on a full bundle. This is because in the reactor the bundles are prevented from axial movement by coolant pressure, adjacent bundles, and fuel channel plugs. In both comparisons creep duration and pellet weight are the

same, with the adjusted  $C_1$  constant being used based on the explanation in Section 7.1. Figures 27 and 28 represent the first comparison with fuel elements that have free endcaps while Figures 29 and 30 are the second comparison using fuel elements with axially (Z-Axis) constrained endcaps.

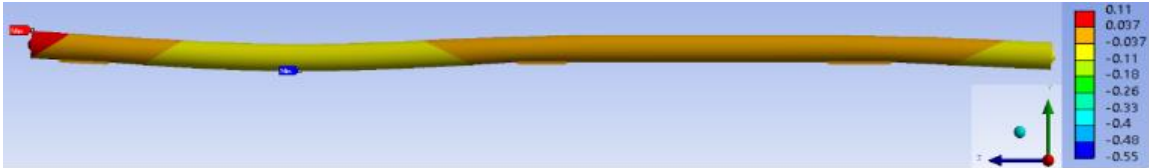


Figure 27: Vertical deformation of an Outer Fuel Element at 300°C with Pellet Weight, Creep, and Free End Caps (mm, 50X Magnification)



Figure 28: Vertical deformation of an Outer Fuel Element with End Flux Peaking Temperatures, Pellet Weight, Creep, and Free Endcaps (mm, 50X Magnification)

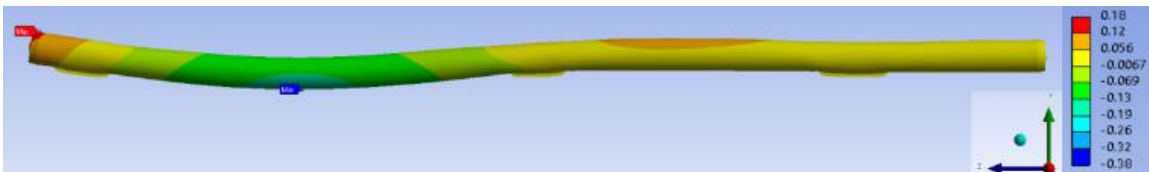


Figure 29: Vertical deformation of an Outer Fuel Element at 300°C with Pellet Weight, Creep, and Axially Fixed Endcaps (mm, 50X Magnification)

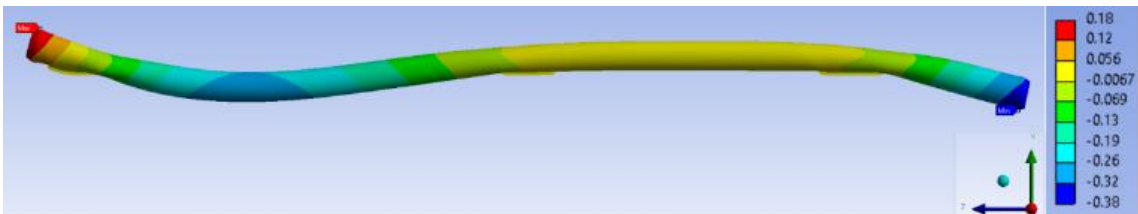


Figure 30: Vertical deformation of an Outer Fuel Element with End Flux Peaking Temperatures, Pellet Weight, Creep, and Axially Fixed Endcaps (mm, 50X Magnification)

Comparing the two temperature profiles it is observed that the higher temperatures from end flux peaking result in a greater amount of vertical deformation. This occurs regardless of how the ends of the elements are constrained; whether they are free to move or axially fixed in the Z-Axis. The difference in deformation is most notable on the inner bearing pad side of the element. This is likely due to both the large overhang between the element end and bearing pad as well as a reduction in stiffness from the local increase in temperature. Of note is that the drooping effect of the element end over the inner bearing pad was a noted observation in post-irradiation analysis [31]. Furthermore, the signature “S” shape is not only maintained, but also more pronounced when end flux peaking is present in the model. Combined, these observations provide support for the inclusion of end flux peaking in the full bundle model.

When comparing the effect of leaving the element ends free or axially constraining them, there are two key observations. The first is that the outer bearing pad end of the element shows the largest change in vertical deformation. This is believed to be due to the proximity of the bearing pad to the end of the element and the resistance it provides against both thermal expansion and the force from pellet weight. When the end of the element is prevented from expanding in the Z-Axis, this creates two constraints to movement that amplify the stress at that location. The second observation is that leaving the ends free causes more upward bowing at the middle of the element and center bearing pad. As mentioned previously, this upward bowing of the bottom elements was seen to occur in the post-irradiation analysis of a bundle and is therefore an important observation with respect to benchmarking the model [31]. Between the verification of the optimum bearing pad boundary condition and the end flux temperature profile these initial studies provided a basis upon which to construct the full bundle model.

## **7.5 Full Bundle Model**

The full bundle model was constructed with the same geometry as Lee *et al* [30], using Ontario Hydro 37-Element CANDU Fuel Bundle drawings [45]. Like the single fuel element studies, the top half of the supporting pressure tube was removed to prevent unnecessary computational load. The resulting model is shown in Figure 31.

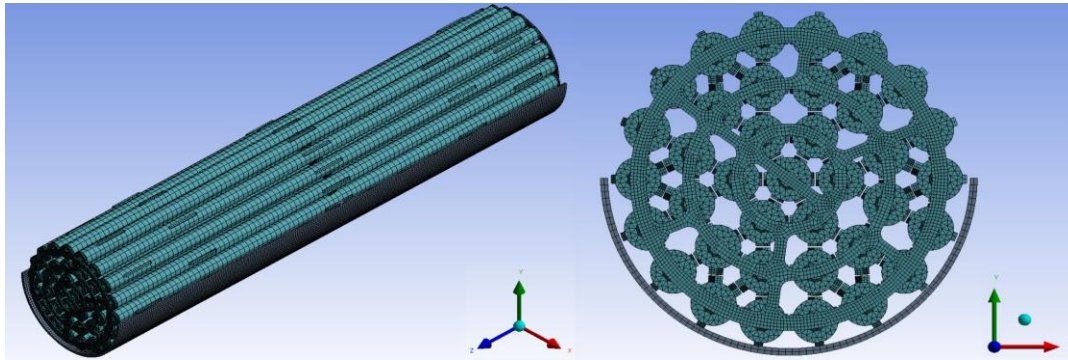


Figure 31: 37-Element CANDU® Bundle Model with Simplified Pressure Tube

A coarse mesh was used for the solid fuel element bodies in the development of the full bundle model compared to the sizing used in the single element studies. This decision was made to save time in the comparison of load steps and boundary conditions by minimizing the RAM requirement that would be created by maintaining the mesh size of the single element studies. Maintaining the same mesh would have resulted in 1,885,250 nodes instead of the 613,418 nodes present in the model from Figure 31. Nevertheless, once the model was stable with all loads incorporated, mesh refinement was completed as a final step in Section 7.5.3. The initial mesh used in the development of the full bundle was created with the element sizing parameters detailed in Table 4. All elements were 3D (solid) and quadratic in nature to ensure geometries were mapped as accurately as possible.

Table 4: Initial Mesh Parameters used in Development of Full Bundle Model

Model Component(s)	Mesh Size	Element Type	Element Order	Sweep Mesh
End Plates	1 mm	Hexahedron	Quadratic	Yes
Endcaps	2 mm	Tetrahedron	Quadratic	No
Bearing Pads and P-Tube	2 mm	Hexahedron	Quadratic	Yes
Spacer Pads	2 mm	Hexahedron	Quadratic	Yes
Fuel Elements	5.5 mm	Hexahedron	Quadratic	Yes

Contact pairs were established between the spacer pads on the fuel elements as well as between the bearing pads and the pressure tube. As shown in Table 4, the mesh parameters are the same for all contact pairs to ensure their interaction is smooth and accurately interpreted by ANSYS™. An image showing all 78 of the spacer pad contact pairs within the bundle is provided in Figure 32. Contact between spacer pads was set with a friction coefficient of 0.1, again based on previous bundle modeling research [47].

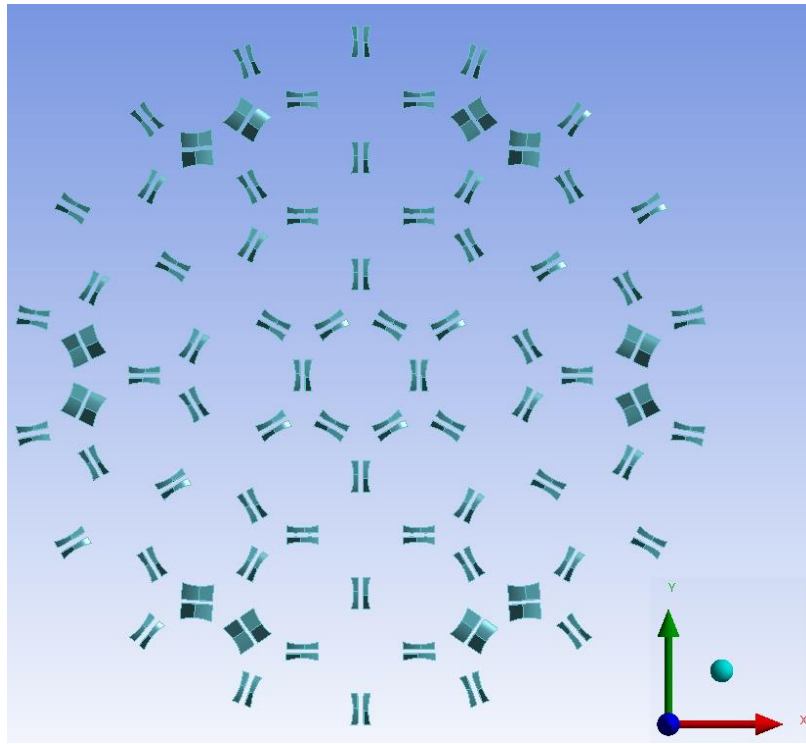


Figure 32: Midplane Spacer Pad Contact Pairs

Contact between bearing pads and the pressure tube was also set as frictional with the same friction coefficient of 0.1, given the same material and contact conditions [47]. The initial condition before the application of any loads had the bearing pads of the bottom two elements in full contact with the pressure tube. A view of this initial contact status is presented in Figure 33. It is important to note that although the initial condition is shown to be “sticking” the contact is still purely frictional. Accordingly, the bearing pads can move in any direction and also become separated from the pressure tube in response to applied loads. This was shown to be an important factor as discussed in Section 7.4.1 when the



center of the fuel element bowed upwards in response to pellet weight and thermal expansion. Accounting for both spacer pads and bearing pads, there are a total of 108 frictional contact pairs in the model per the realistic conditions in the CANDU® reactor.

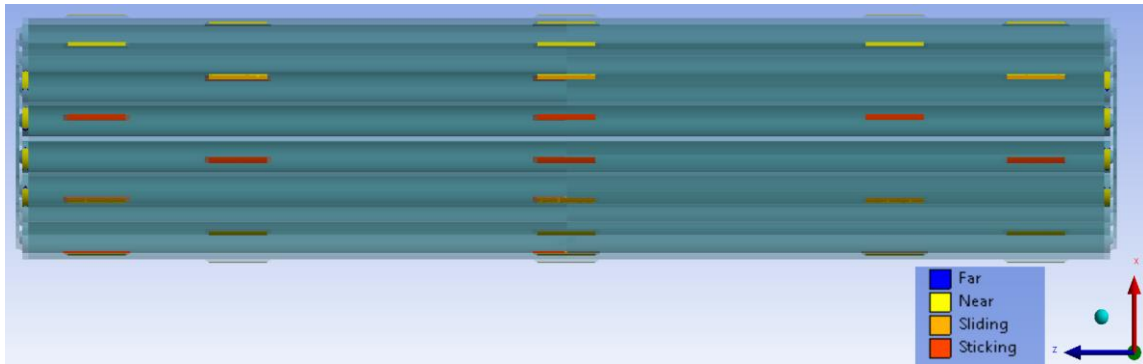


Figure 33: Initial Bottom Element Contact Status with Pressure Tube

When presenting the results from full bundle models it is helpful to define an orientation by identifying fuel elements and their location with respect to both other elements and the supporting pressure tube. Figure 34 defines the nominal bundle orientation used for all models unless otherwise stated. Fuel elements 1 through 18 are the outer fuel elements with elements 10 and 11 at the bottom of the bundle in contact with the pressure tube at the 6 o'clock position.

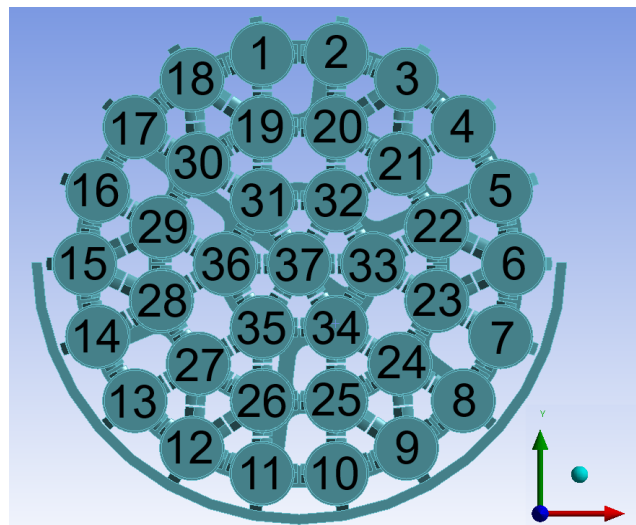


Figure 34: Nominal Bundle Orientation and Fuel Element Identification



### 7.5.1 End Plate Boundary Conditions

The first simulations to be run with the full bundle geometry focused on the accurate application of end plate boundary conditions in response to combined loads of pellet weight, coolant pressure, temperature profile, and creep. To account for pellet weight, the nominal value of 6.5 N per fuel element was applied to each of the 37 elements in the bundle. An end flux temperature profile was adopted based on the results from Section 7.4.2 and Figure 22. The estimated dynamic coolant pressure of 3600 Pa was applied to the upstream end of the bundle and the adjusted creep constants from Table 2 were set for the creep rate. Only two sets of end plate boundary conditions were considered valid based on past and present CANDU® fuel channel architecture. The application of dynamic coolant pressure to the upstream end plate and fuel element ends remained consistent throughout both sets of conditions. Where they differed was in the axial (Z-Axis) constraint applied to the downstream end of the bundle. The first condition reflected a latch system with only the downstream ends of the outer 18 elements being constrained. The second set simulated the F3SP shield plug modification by axially constraining the face of the downstream end plate.

These two downstream end plate conditions were based upon past and present designs of CANDU® fuel channels. In CANDU® 6 reactors, the fuel string consisting of 12 bundles is held in the fuel channel at the downstream end by a F3SP shield plug that fully supports the rings of the last bundle's end plate. This was not the case for Darlington (DNGS) or Bruce (BNGS) reactors, however, as prior to a modification of the shield plug at BNGS, only circumferential latches that contacted the outer 18 fuel elements were used to support the last bundle [32]. The lack of support for the end plate in the latch design created concerns over end plate cracking and led to the F3SP modification to fully support the endplate for BNGS reactors [32]. Whether with latches or the shield plug, this part of the fuel channel is responsible for resisting the axial load imparted on the bundles by coolant flow. With the exception of DNGS, CANDU® 6 and BNGS reactors are now using the shield plug support [32]. As a result, boundary conditions for both designs are evaluated not only for benchmarking but also to compare the impacts of past and present fuel channel design on end plate deformation.

The dynamic pressure from coolant flow against the upstream end plate is the dominant load at the upstream end of the bundle and holds it in position, tandem

with the downstream end plate boundary conditions [32]. The upstream end plate coolant pressure and downstream end plate boundary conditions are considered applicable to all bundles in the fuel string, since the freedom of movement, or lack thereof, at each end should be translated through contact of end plates. Figure 35 shows a CANDU® fuel channel with coolant flowing from left to right. It highlights the nosepiece of the shield plug at the downstream end that supports the end plates in the F3SP modified design. The latches that were historically the only support for the fuel string can also be seen since even with the F3SP modification they are still present in the fuel channel. Based on the increased support from the modified shield plug, it was expected that the model with the corresponding boundary conditions would exhibit less end plate deformation than the model with the latch based condition.

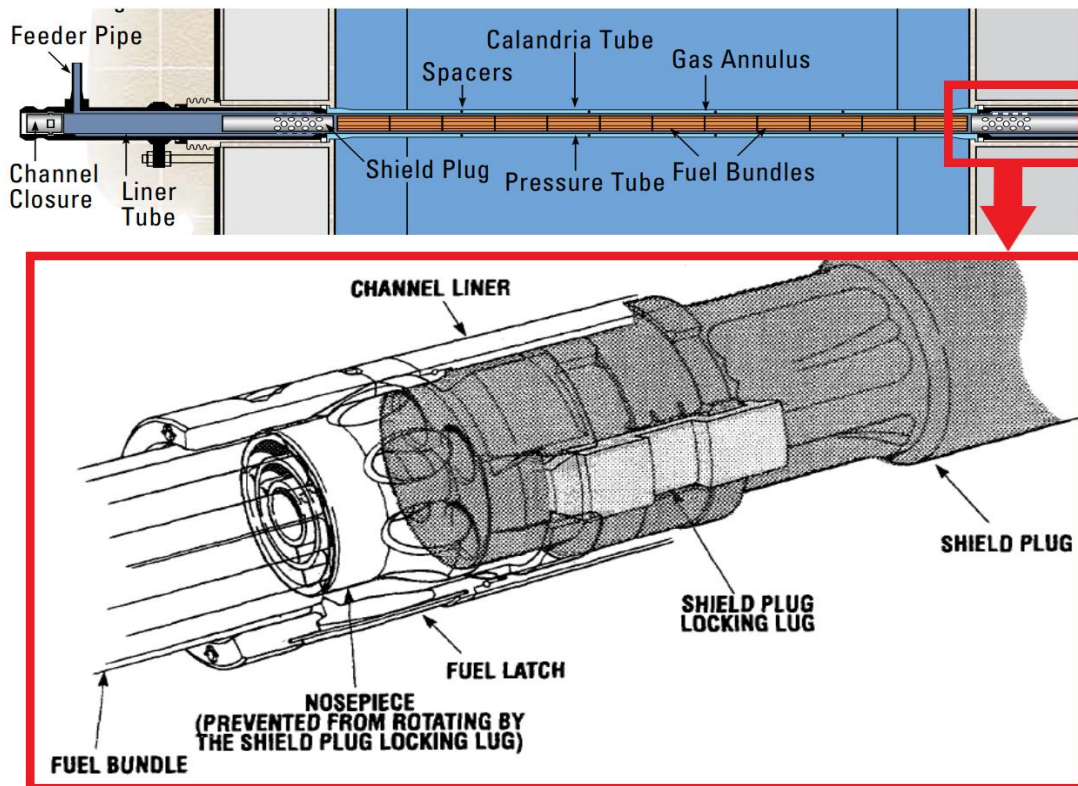


Figure 35: CANDU® Fuel Channel Architecture - Modified Downstream Shield Plug Highlighted in Red - Adapted from [45] and [47]

Other studies [30] sought to achieve the desired deformation shape by only constraining specific parts of the end plate. Although they were successful, fixing

only a few webs or a single part of the end plate is not accurate to the true conditions in the reactor and poses an issue for future validation. Accordingly, this approach was not adopted and is why only the latch and shield plug based end plate constraints were considered in this analysis.

Figure 36 shows the application of temperature profile and pellet weight while Figure 37 shows the application of dynamic coolant pressure to the upstream end of the bundle and the two downstream end plate conditions. Areas highlighted in red represent the locations where forces are applied, while areas highlighted in yellow indicate boundary conditions where the bundle is prevented from moving in the Z-Axis or axial direction.

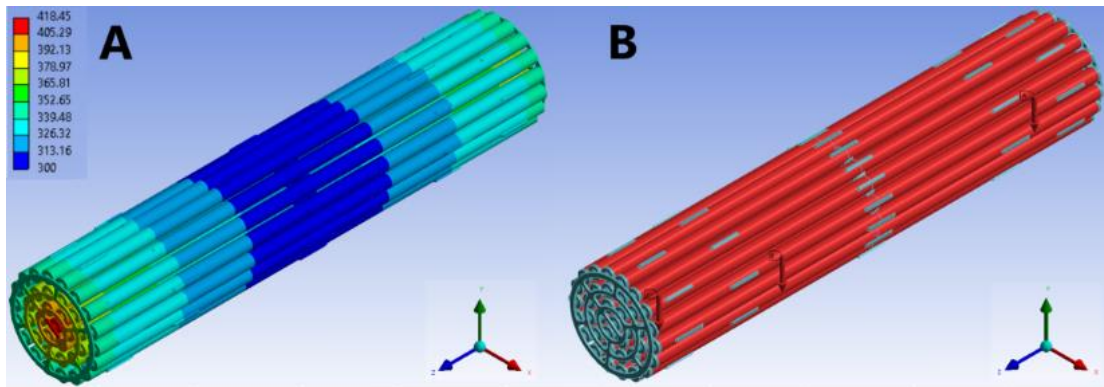


Figure 36: Temperature Profile (A) and Pellet Weight Loading (B)

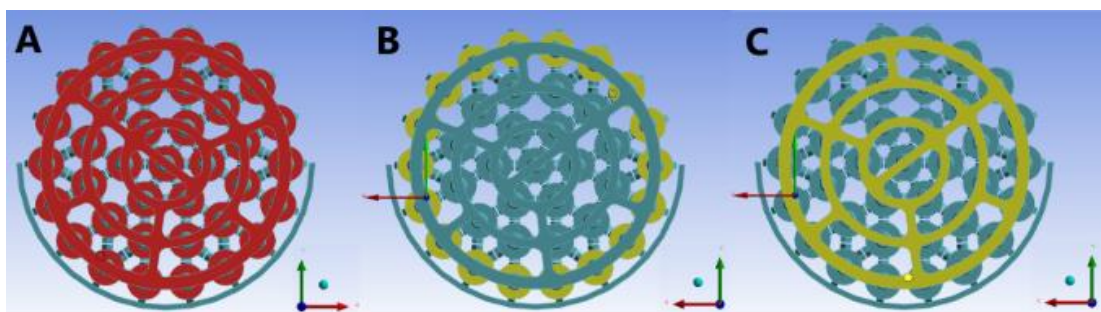


Figure 37: Upstream Coolant Pressure (A) and Downstream Fuel Bundle Support - Latches (B) and F3SP Shield Plug (C)

The following Figures compare differences in vertical, axial, and radial deformation between 37-Element bundle models with latch and shield plug end plate conditions. The deformation is the result of combined loads and equivalent amounts of creep with the same duration and Norton constants. The total creep is arbitrary for these models, since the goal was to compare key deformation effects and profiles instead of discerning exact magnitudes. Figure 38 depicts a side-by-side comparison of vertical deformation in the Y-Axis while Figures 39 and 40 are to be viewed in conjunction to ascertain the difference in axial deformation in the Z-Axis. Particular attention is to be paid to the difference in end plate deformation in these two Figures. Figures 41 through 43 plot the radial displacement of fuel elements at the midplane. The midplane, or the point equidistant from the two end plates in the center of the bundle, was selected as the primary point of comparison due to it being the furthest location from the boundary conditions. Combined, Figures 38 through 43 show the clear differences in overall deformation magnitude and shape between the two different end plate constraints.

The models presented in this section are empty bundles without fuel pellets, yet are highly complex, having incorporated end flux temperature profiles, pellet weight, coolant pressure, and creep. Development of the models required careful refinement of load steps to achieve convergence without the model becoming over- or under-constrained. Five independent load steps were used to apply the reactor loads before creep was initiated. The order of these steps was rearranged multiple times to confirm that the sequence of application did not affect the results.

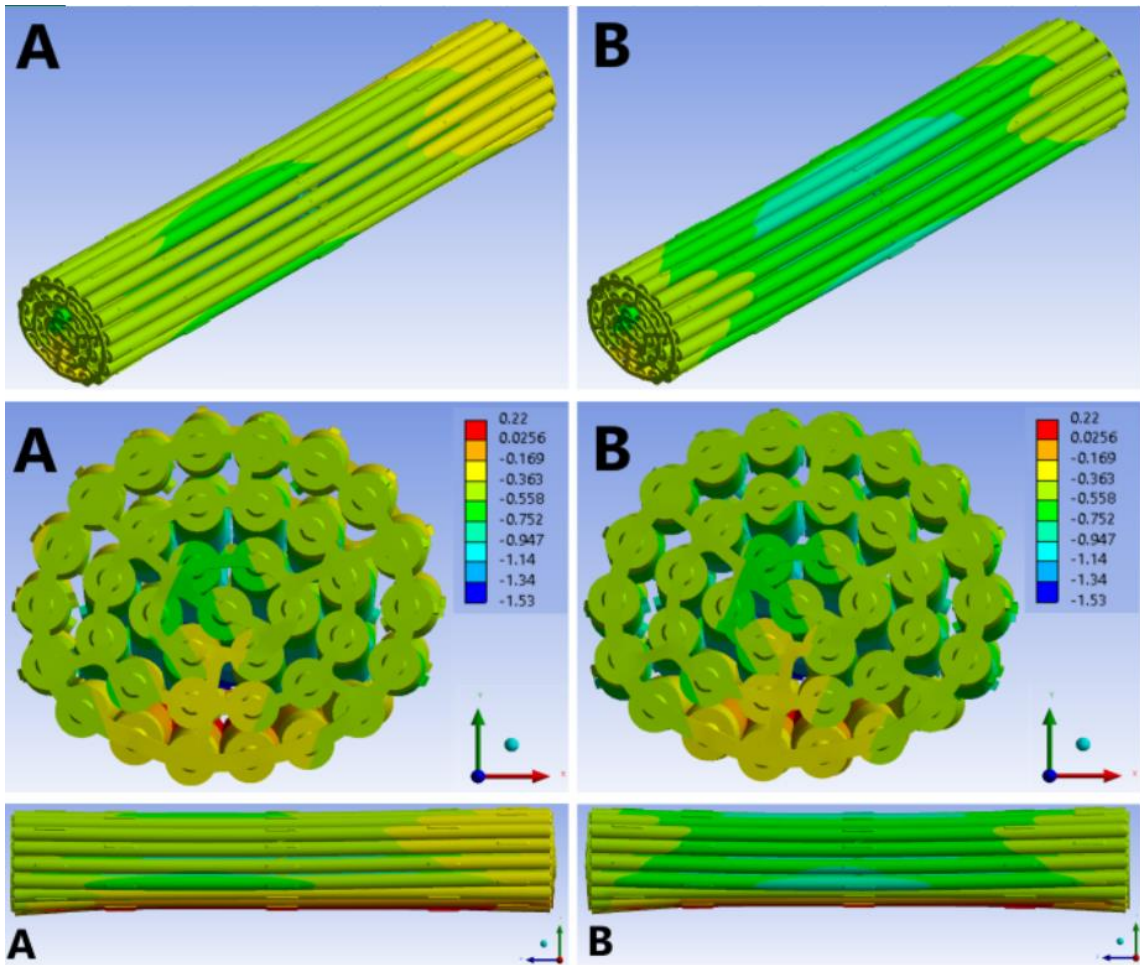


Figure 38: Vertical deformation of a Latch (A) and Shield Plug (B) Supported 37-Element Bundle with Empty Fuel Elements, End Flux Temperatures, Pellet Weight, Coolant Pressure, and Creep (mm, 15X Magnification)



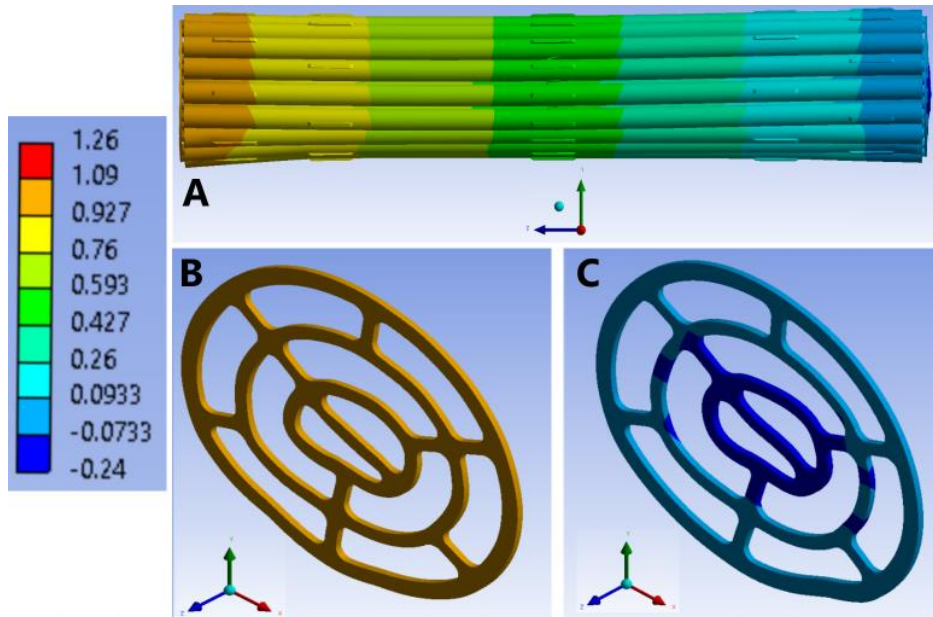


Figure 39: Axial Deformation of a Latch Supported Bundle with End Flux Temperatures, Pellet Weight, Coolant Pressure, and Creep. Full Bundle (A), Upstream Endplate (B), and Downstream Endplate (C) (mm, 15X Magnification)

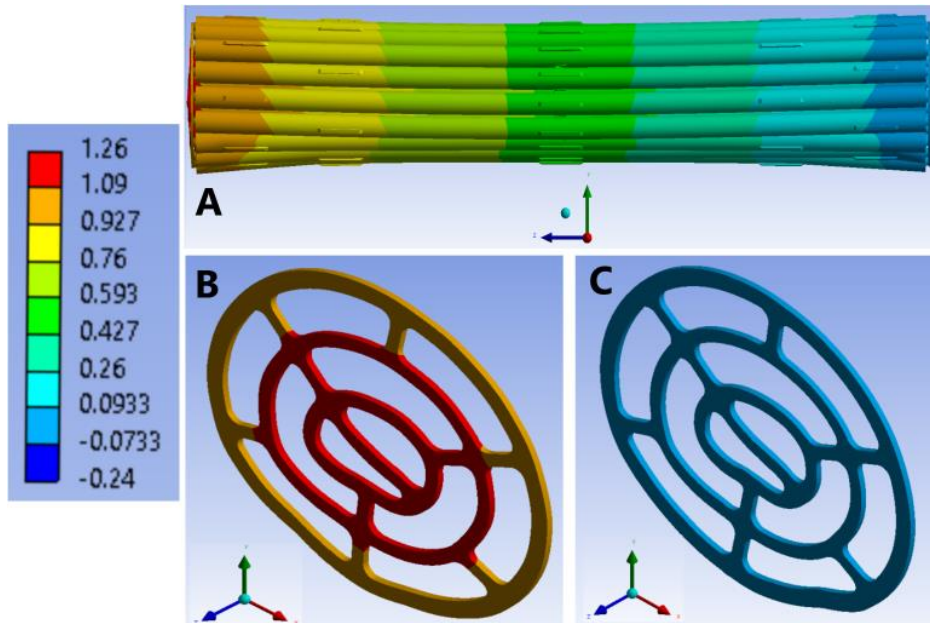
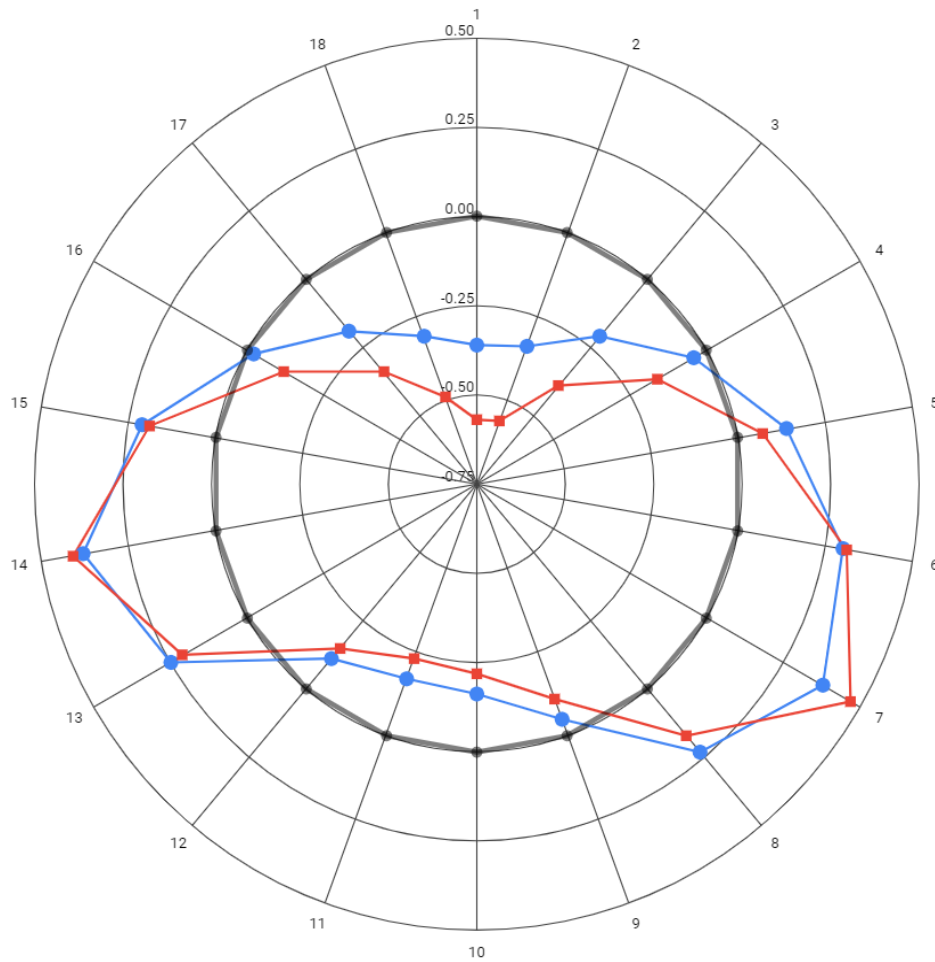


Figure 40: Axial Deformation of a Shield Plug Supported Bundle with End Flux Temperatures, Pellet Weight, Coolant Pressure, and Creep. Full Bundle (A), Upstream Endplate (B), and Downstream Endplate (C) (mm, 15X Magnification)



● Latch Constrained Bundle ■ Shield Plug Constrained Bundle ● Undeformed Bundle

Figure 41: Difference in radial displacement of Outer Fuel Elements at the bundle midplane - Latch Vs. Shield Plug Supported Bundle (mm)

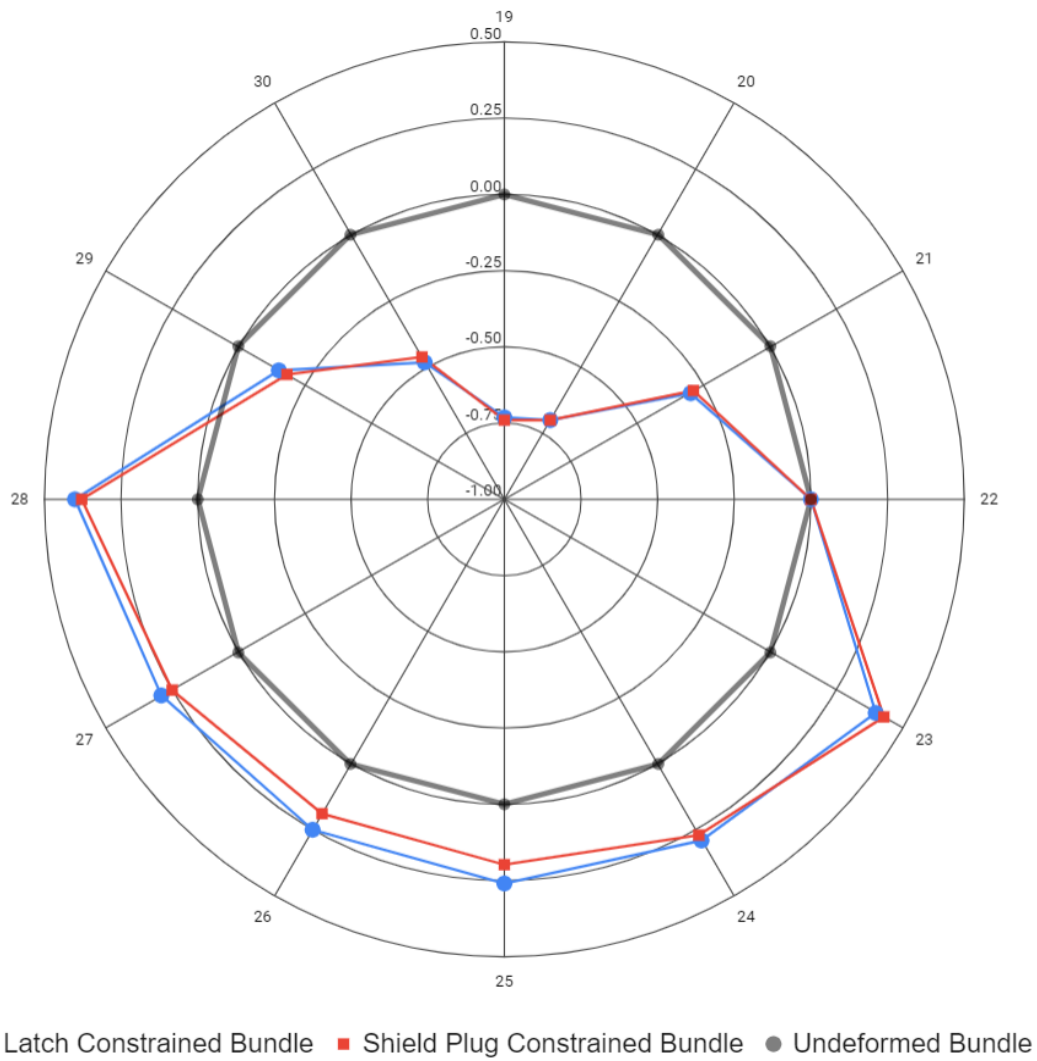


Figure 42: Difference in radial displacement of Intermediate Fuel Elements at the bundle midplane - Latch Vs. Shield Plug Supported Bundle (mm)



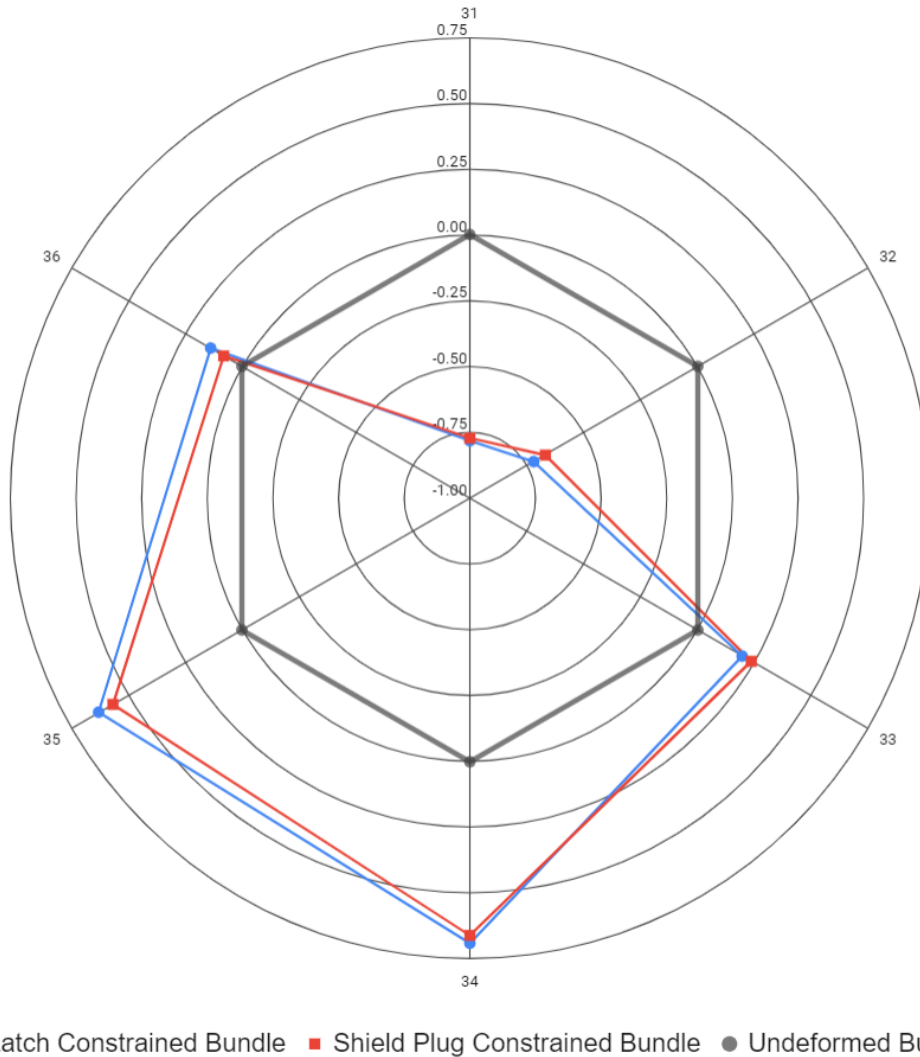


Figure 43: Difference in radial displacement of Inner Fuel Elements at the bundle midplane - Latch Vs. Shield Plug Supported Bundle (mm)

The most notable differences between the two end plate supports are in the radial and vertical deformation of the outer fuel elements along with the dishing and doming of the end plates. Otherwise the two models produce similar results in both deformation magnitudes and profiles. The deformation of the intermediate and inner fuel elements is particularly consistent, with the latch supported bundle exhibiting marginally greater radial displacement in the lower elements. Both models produce a slumping effect as can be seen in Figure 41; the top and bottom elements are compressed towards each other, while the side elements

are forced outwards and away from the center of the bundle. The bottom elements are also seen to bow upwards, as expected and seen in the single element studies. These are important observations because these deformation characteristics were observed in post-irradiation analysis [31]. Achieving this outcome, using realistic loads and boundary conditions, was a key milestone for full bundle model development.

With respect to the difference in results between the two downstream end plate supports, the outer fuel elements at the top of the bundle deform less in a latch supported bundle than that with support from the F3SP modification. A more distinct trough shape is formed by the latter. This is a result of the axial constraint being applied directly to the fuel element ends in the latch supported bundle and preventing them from being able to rotate at the end plate connection. With shield plug support, the fuel element ends have unrestricted movement, allowing rotation at the connections to the end plate. This in turn allows greater deflection of the outer fuel elements. With the entire downstream end plate face being axially constrained by shield plug support, the coolant pressure is also concentrated into displacing fuel elements rather than deforming the end plate. This is evident by the absence of doming in the downstream end plate in the shield plug supported bundle between Figures 39 and 40. This is hypothesized to also aid in increasing deformation of the outer fuel elements in the shield plug model.

End plate deformation is significantly different between the two models as shown in Figures 39 and 40. The fuel latch supported bundle exhibits distinct doming in the downstream end plate and the beginning of dishing in the upstream end plate. In both end plates this deformation occurs in the direction of coolant flow. Higher coolant pressures were observed to make the dishing in the upstream endplate more distinct and better reflective of post-irradiation data [31]. This suggests that incorporation of hydraulic drag would likely be required to achieve the full effect. Without sufficient data to determine the magnitude of this load, however, the dynamic coolant pressure was maintained as the sole coolant based load. In the shield plug model there was no doming in the downstream end plate and the effect in the upstream end plate was reversed from the fuel latch supported bundle such that doming was observed against the flow of coolant. The reason for this being the greater restriction in axial movement of fuel elements with shield plug support, combined with the non-uniform thermal expansion caused by higher temperatures in the center of the bundle. This

results in the thermal expansion of all fuel elements being concentrated in the upstream end plate, which created the observed doming effect against the flow of coolant. It was therefore concluded that thermal expansion is dominant over coolant pressure in the shield plug supported model with respect to axial end plate deformation. Unless a higher pressure is applied to account for the coolant drag force the coolant pressure only affects fuel element deformation in the shield plug model and not the end plates. This becomes an important factor in the final model and results.

The dishing and doming of end plates in the latch supported bundle was observed in experimental post-irradiation analysis [31]. Although upstream end plate dishing is more distinct in the experimental data this still indicates the latch supported model is deforming as expected. This is especially true when considering that bowing of fuel elements at the top and bottom of the bundle was also being accurately reproduced by the model. There was no data available for a bundle from a F3SP fuel channel so the associated model's deformation results cannot be accepted or refuted. Nevertheless, with knowledge that the two models are identical aside from end plate boundary conditions, the F3SP model's results would likely share a similar amount of accuracy if there were data available for a bundle from a F3SP fuel channel. In summary, both the latch and F3SP models were capable of producing the expected deformation shapes and characteristics, particularly at the midplane and end plates. This provided the confidence to evaluate further aspects of bundle modeling including fuel pellets and refinement of the finite element mesh. The implications of the deformation differences between the two fuel channel supports are discussed Section 9.

### **7.5.2 Pellet Stiffening Effects**

Up to this point the models have not included pellets and only used hollow fuel elements. As mentioned in Section 7.3, this was the preference from the outset due to the need for many assumptions and the history of pellet modeling being computationally onerous. Nevertheless, some understanding of the deformation effects being lost by excluding pellets was still needed. Therefore, this Section evaluates bundle deformation by comparing bundles with a simplified pellet approximation against bundles with hollow fuel elements. End plate boundary conditions for both latch and shield plug based fuel channels were considered.

The inclusion of pellets is approximated in the model by modifying fuel elements from hollow Zircaloy-4 tubes into solid Zircaloy-4 rods. Aside from the difference in material properties between Zircaloy-4 and  $\text{UO}_2$ , this approach was hypothesized to be able to capture some of the pellet stiffening effects, assuming they were uniform and did not change over the bundle's life in the reactor. The values for pellet weight, end flux temperatures, and creep were maintained from Section 7.5.1.

There are five figures presented in this Section to compare bundles with solid fuel elements to those with hollow fuel elements. Figures 44 and 45 compare the two types of bundle models in vertical deformation for latch and shield plug supported bundles respectively. Figures 46 and 47 compare the midplane radial displacement of the two types of bundles. They include plots for solid and empty fuel element bundles subjected to equivalent amounts of creep, but also a solid fuel element bundle with 20 times the equivalent creep. The amplified creep bundle was included based on the hypothesis that the pellet stiffening effect would reduce deformation rates, but not affect the overall shape. Lastly, Figure 48 identifies how the location of maximum stress changes between the hollow and solid fuel element bundles.

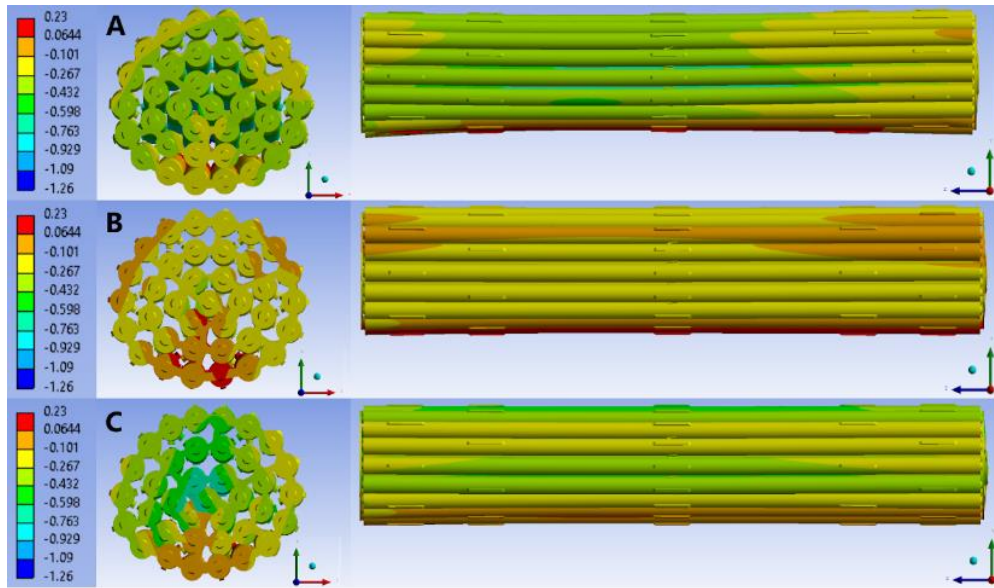


Figure 44: Vertical Deformation of a Latch Supported Bundle with End Flux Temperatures, Pellet Weight, Coolant Pressure, and Creep. Bundle with Hollow Fuel Elements (A), Solid Fuel Elements (B), and Solid Fuel Elements with 20X Creep (C) (mm, 15X Magnification)

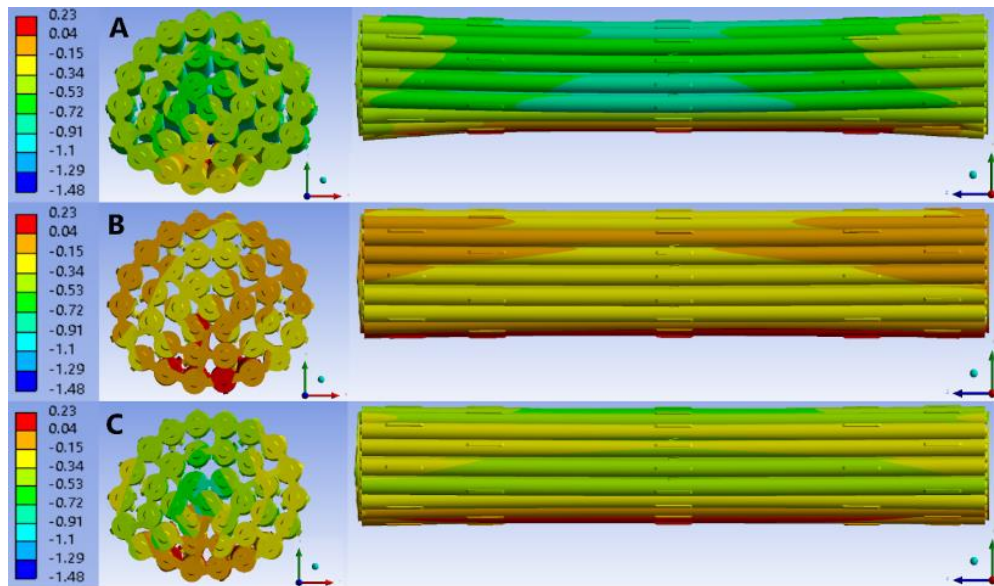


Figure 45: Vertical Deformation of a Shield Plug Supported Bundle with End Flux Temperatures, Pellet Weight, Coolant Pressure, and Creep. Bundle with Hollow Fuel Elements (A), Solid Fuel Elements (B), and Solid Fuel Elements with 20X Creep (C) (mm, 15X Magnification)

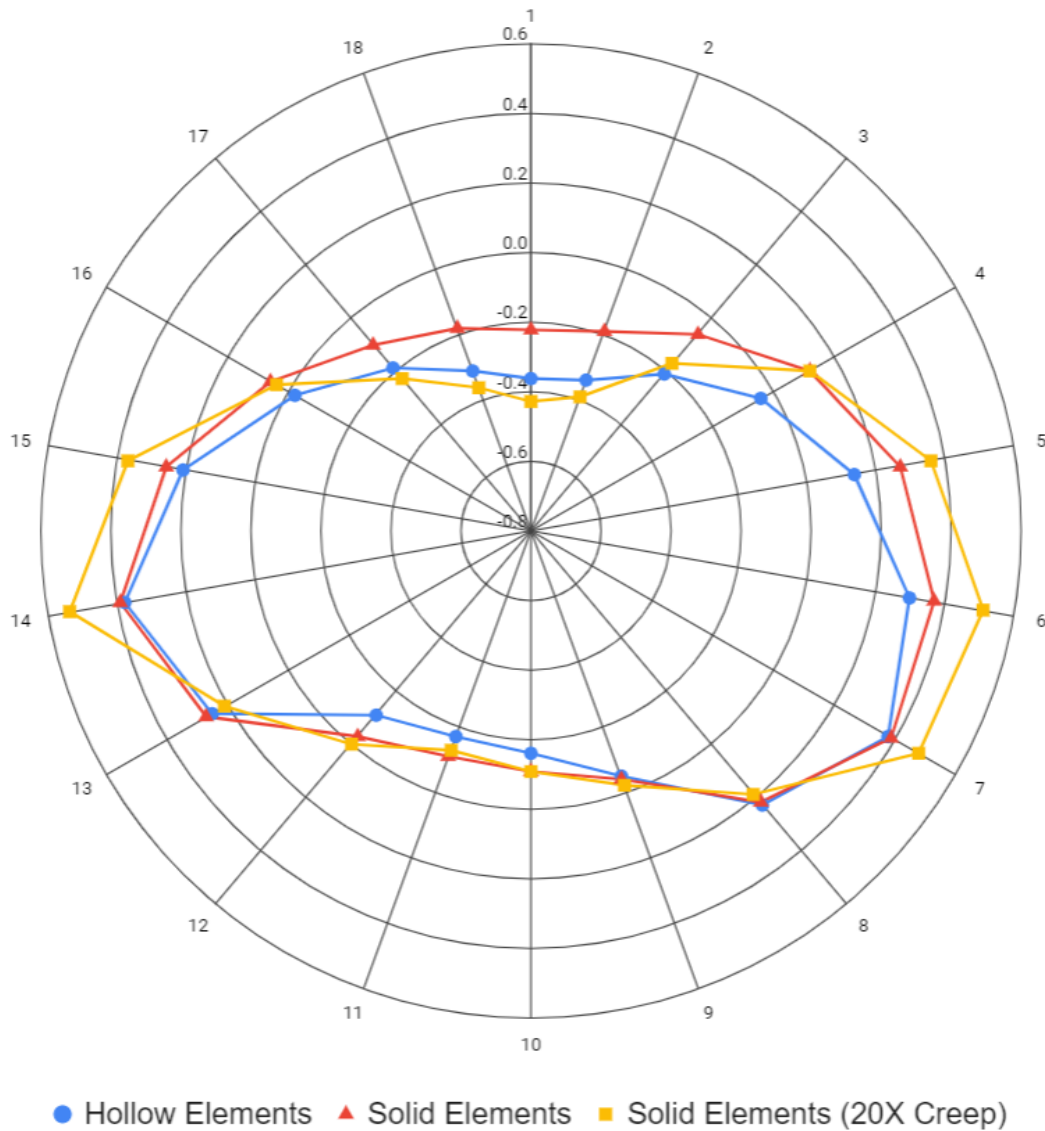


Figure 46: Difference in radial displacement of Outer Fuel Elements at the Bundle midplane between Bundles with Hollow and Solid Fuel Elements for a Latch supported Bundle (mm)

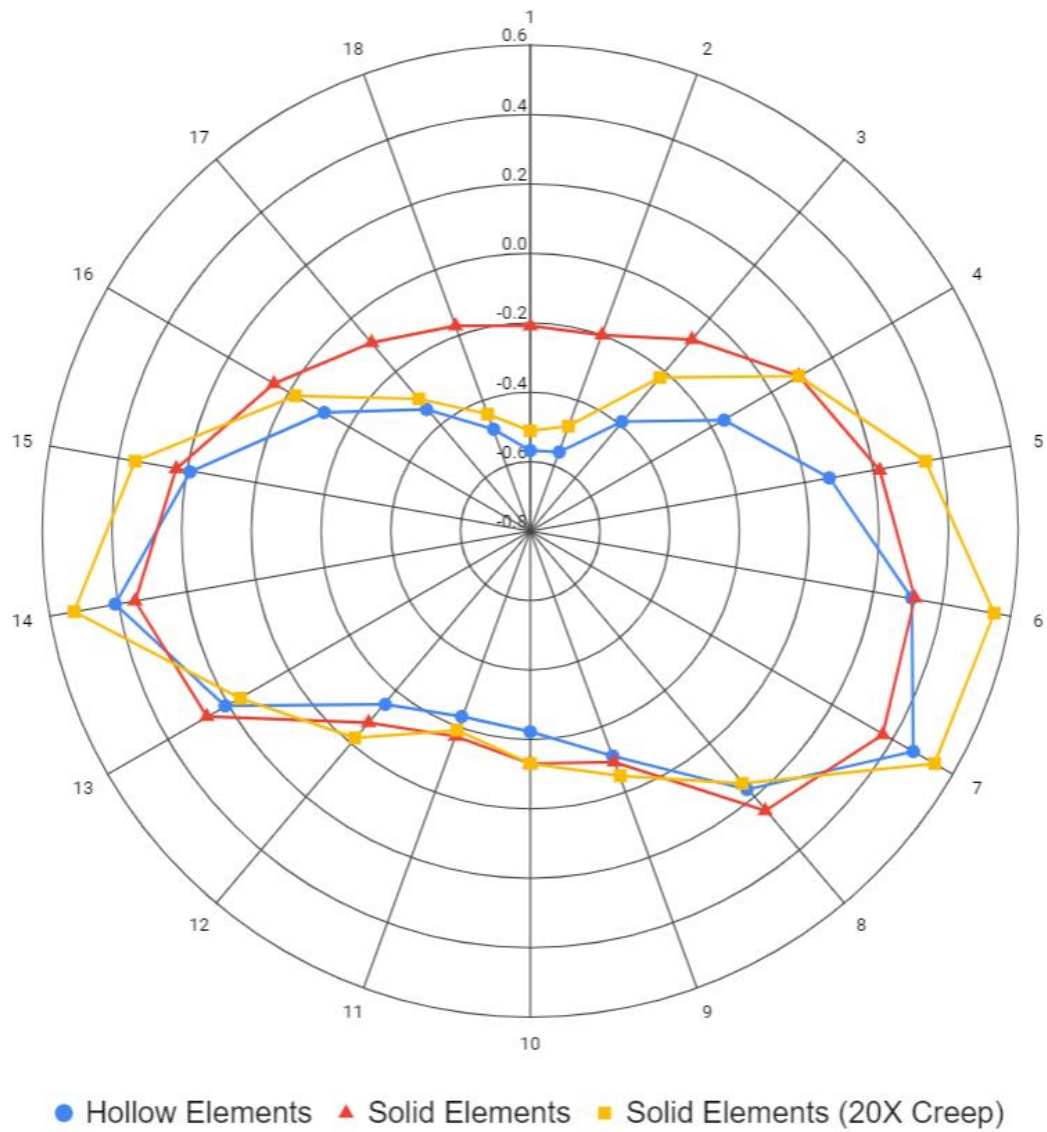


Figure 47: Difference in radial displacement of Outer Fuel Elements at the Bundle midplane between Bundles with Hollow and Solid Fuel Elements for a Shield Plug supported Bundle (mm)



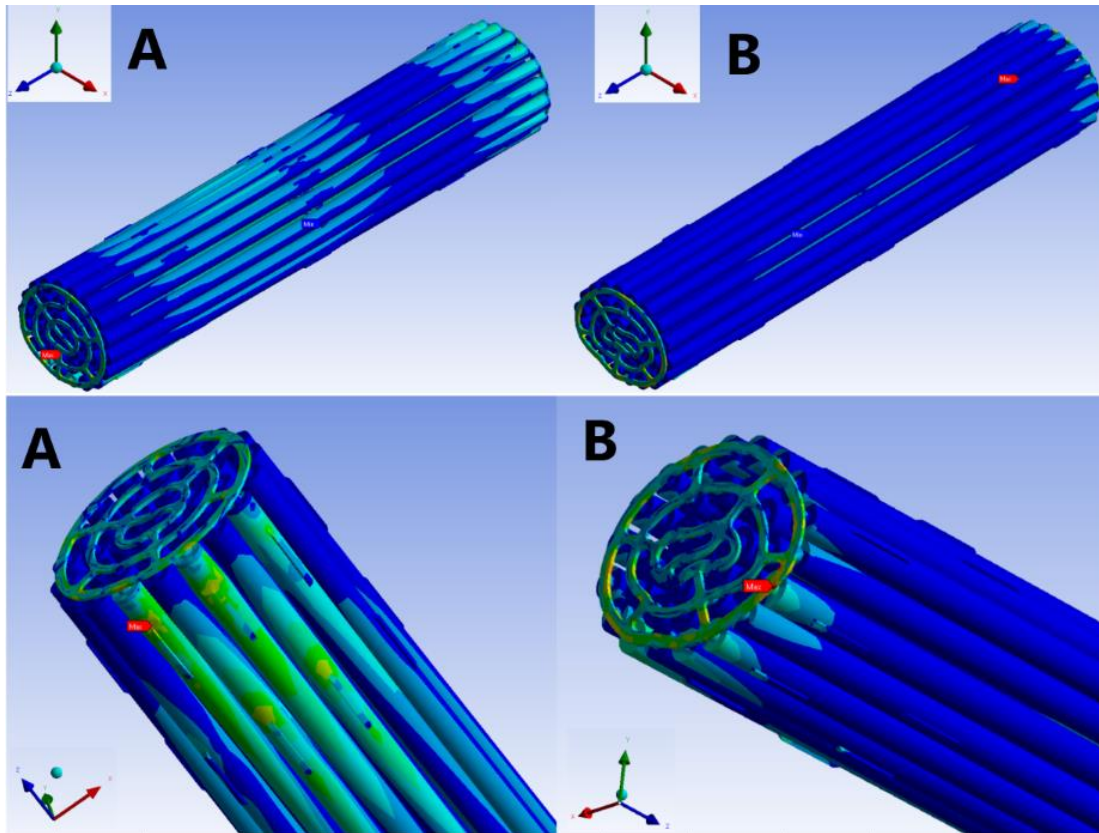


Figure 48: Difference in Location of Maximum Stress between Bundles with Hollow Fuel Elements (A) and Solid Fuel Elements (B) (15X Magnification)

When comparing bundle models with solid fuel elements to those with hollow fuel elements, the deformation magnitudes differ, but the profiles are relatively consistent. The increased stiffness of the solid fuel elements does little more than to provide additional resistance to the applied loads. When subjected to the same creep duration, the models with solid elements deform less than those with hollow elements. However, similar results can be achieved in both by adjusting the total amount of creep. Representing pellets using solid fuel elements thus primarily affects deformation rate of the bundle and not the resultant shape. There are two exceptions to this. The first is that the solid fuel element models exhibit more lateral deflection of side elements. The second is a change in the location of maximum stress.

The additional lateral deflection of the side elements in the solid fuel element models is attributed to the increase in thermal expansion from the additional



material. The increased expansion causes further stress, which results in larger deformations when subjected to higher amounts of creep. In the real bundle even more expansion is expected, since  $\text{UO}_2$  has a 50% greater thermal expansion coefficient than Zircaloy-4 [39][48]. However, this would be compounded with the fact that  $\text{UO}_2$  is a ceramic with a high elastic modulus. Combined, not only is a real fuel element hypothesized to expand more, but its increased stiffness would also reduce the impact of the resulting stress. Without using material properties for  $\text{UO}_2$  and modeling realistic pellets this hypothesis cannot be proven. Therefore, the increased lateral deflection in the solid element model is attributed to being an effect of the highly simplified pellet approximation and not necessarily an effect reflective of what would occur in a real fuel bundle. Accordingly, this observation was not considered sufficient evidence to adopt the solid fuel element model.

The difference in maximum stress location is explained by the concentration of bundle weight on the bearing pads of the outer fuel elements. This creates a point load where the bearing pad meets the fuel element and concentrates stress at that location. This is particularly apparent when the fuel elements are hollow as seen in Figure 48. When the fuel elements are solid, this point load is still present but the additional material in a solid fuel element causes the force to be distributed over a larger area. This reduces the stress at the bearing pad to fuel element connection and causes the maximum stress to be reported in a different part of the bundle. This is likely to be the case for a real fuel bundle, but since end plates were the focus of this study, this observation was not considered to be of great consequence. Despite the difference in location of maximum stress, the overall stress distribution in the end plate was highly comparable between solid and hollow fuel element bundles. This was expected because the load transmission from the fuel elements to the end plate remains unchanged. Accordingly, the same conclusion for the lateral deflection observation was reached in regards to stress. The solid element model was not providing a significant advantage over the hollow fuel element model.

At the end of this study it was concluded that there was minimal benefit to the potential increased computation load by assuming fuel pellets could be approximated with solid fuel elements. At mesh sizes approaching 2 mm a transition from a model with hollow fuel elements to a model with solid fuel elements doubled the number of nodes, which would significantly increase computation time and the RAM requirement. There were no differences between

the two models that could not be explained as a result of assumptions in building the model or the finite element method. Consequently, solid fuel elements were not carried forward. The hollow fuel element model was capable of producing all of the desired deformation effects with the same impacts to the bundle end plate. This does not mean the same conclusion would be reached if a true pellet representation was incorporated. Pellets are unlikely to behave as a monolithic entity as is assumed by using solid fuel elements and the properties of Zircaloy-4 are vastly different from  $\text{UO}_2$ . Development of an accurate method for including the effects of fuel pellets remains an important aspect of model development. For the purposes of this study however, a solid fuel element model was not seen to provide any advantages beyond that of a hollow fuel element model.

### **7.5.3 Mesh Convergence Study**

The final step of model development was the completion of a mesh convergence study to balance computation load with consistent results. There were two bundle components studied for mesh convergence; the fuel element bodies and the end plate. The fuel element bodies were initially given a coarse mesh while building the model, but coarse meshes can distort the shape of curved surfaces and affect results as shown in Section 6. For this reason a mesh convergence study on the fuel element bodies was needed. The second convergence study was completed on the end plates, since they are the component of interest. The initial mesh was already quite small at 1 mm, but additional data was required to verify that the maximum stress locations and magnitudes in the end plate did not change significantly if the mesh was further refined.

There are four Figures presented to explain the two mesh convergence studies. Figures 49 and 51 show how maximum values of displacement and stress change as a function of mesh size in the fuel elements and end plate. These Figures identify an acceptable mesh size based on when the stress or displacement begins to converge with increased model size (number of nodes). For example, a 5% increase in stress from doubling the number of nodes is considered to have converged, since the additional data points and computing time are not providing proportional benefit. Figures 50 and 52 depict how different mesh sizes map the fuel elements and end plate. Specifically shown are the accepted, smallest, and largest mesh sizes considered for the two components. The fuel element convergence study is presented first.

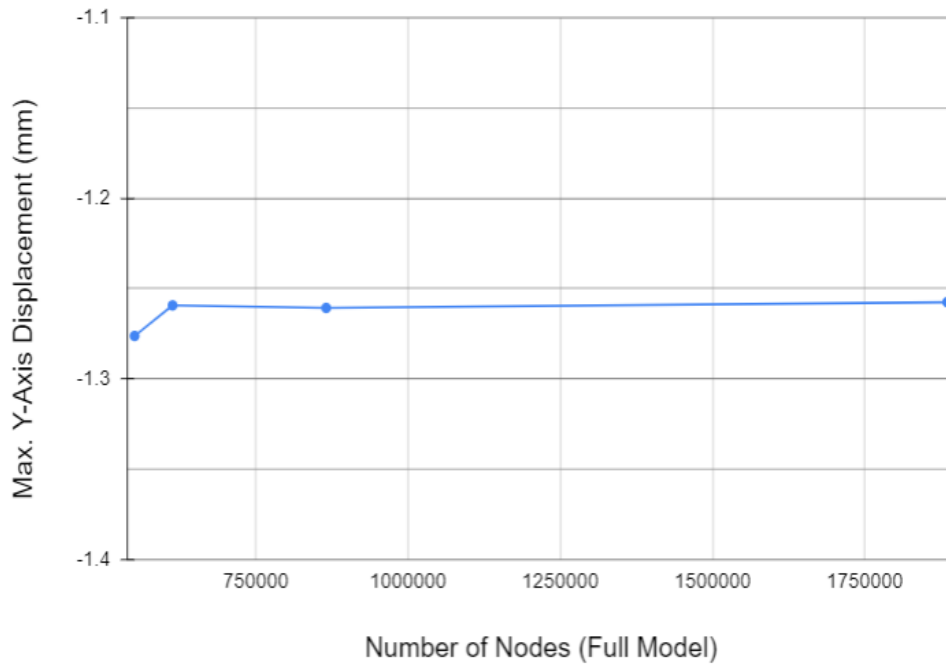


Figure 49: Fuel Element Mesh Convergence Study using Maximum Vertical Deformation and Fuel Element mesh sizes of 7 mm, 5.5 mm, 3.5 mm, and 2 mm

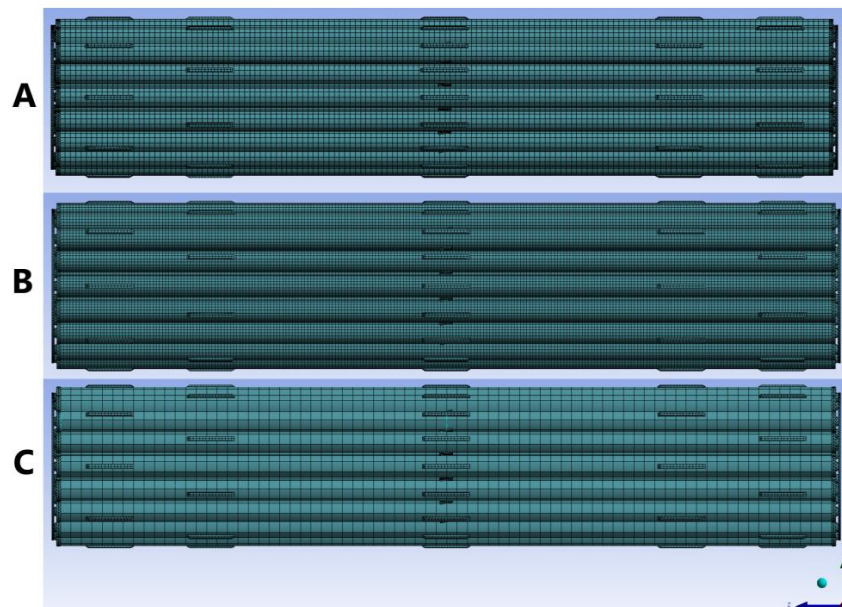


Figure 50: Selected Fuel Element Mesh sizes comparing accuracy to recreate Fuel Element geometry 3.5 mm (A), 2 mm (B), 7 mm (C)

The mesh convergence study for the fuel elements determined that the ideal mesh consist of 3.5 mm hexahedrons. Decreasing the size beyond this value resulted in a negligible difference in results for the increase in model size. Maximum vertical deformation was consistent in all considered mesh sizes at approximately -1.26 mm. Lee *et al* [30] performed a fuel element mesh convergence study using single fuel elements and observed convergence in vertical deformation at a mesh size of 4 mm. Accordingly, the results of both this study and that of Lee *et al* [30] are in agreement and support the conclusion of a 3.5 mm mesh for fuel elements being acceptable. This is qualitatively supported by the visual comparison in Figure 50, which shows a smooth fuel element surface with the 3.5 mm mesh. Smaller mesh sizes provided only minimal improvement.

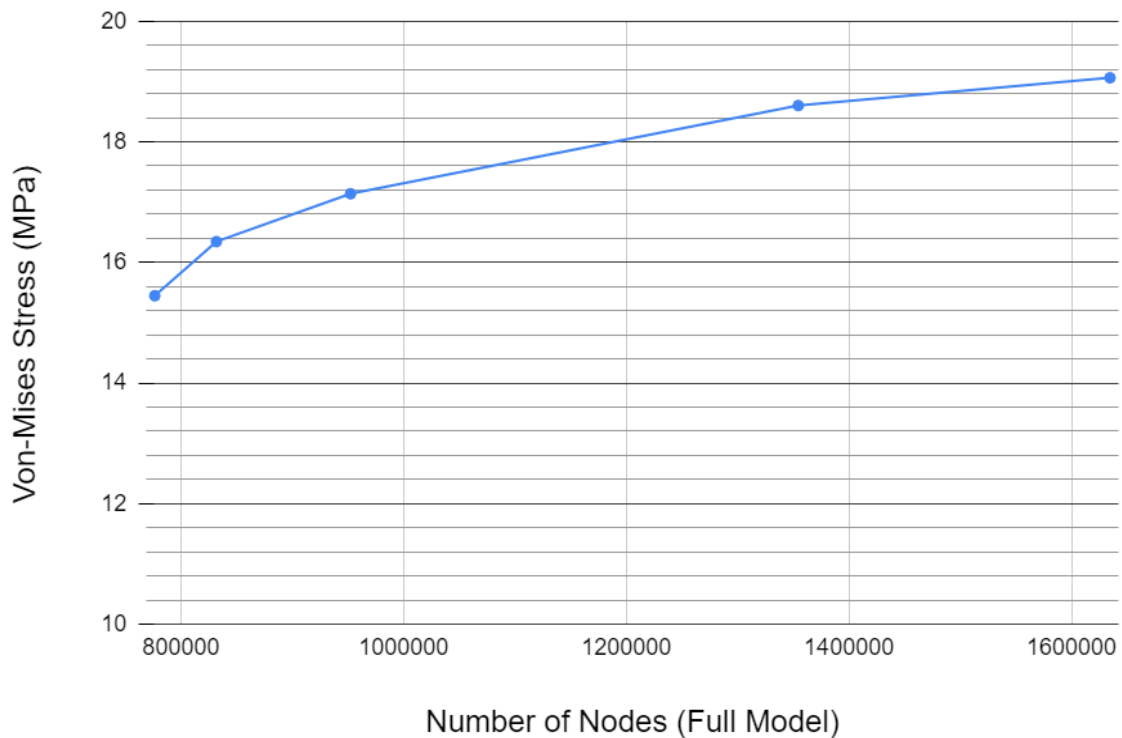


Figure 51: End Plate Mesh Convergence Study using Maximum Von Mises Stress and End Plate Mesh sizes of 2.5 mm, 2 mm, 1 mm, 0.5 mm, and 0.4mm

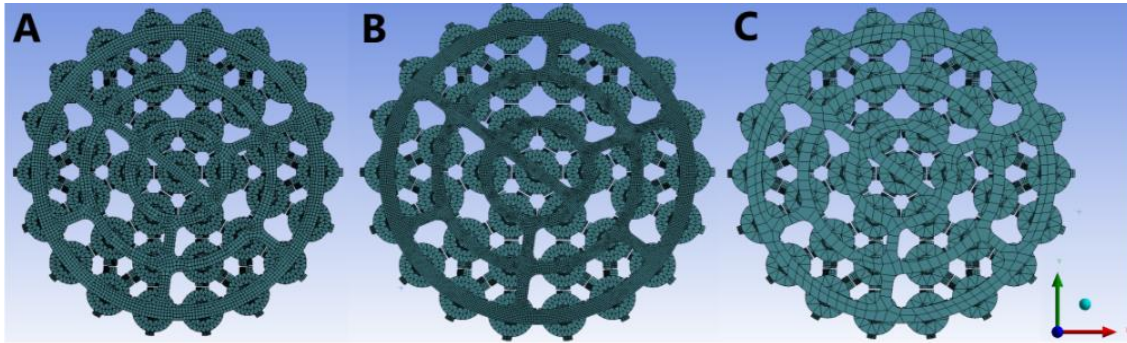


Figure 52: Selected End Plate Mesh sizes comparing accuracy to recreate End Plate geometry 1 mm (A), 0.4 mm (B), 3 mm (C)

The convergence study for the end plate required adjustment of the endcap mesh to smooth the transition region from the fuel elements to the end plate. As a result, the accepted mesh for the end plates was also dependent upon the mesh of the endcaps. An end plate mesh size of 1 mm with a 1.5 mm endcap transition region was found to be the ideal mesh size in this convergence study. In Figure 51 this mesh size corresponds with the third data point. The smallest mesh size considered increased maximum stress from the 1 mm size by only 11% despite a 72% increase in nodes and computation size. In Figure 52 the 1 mm mesh size can also be qualitatively seen to map the surface of the end plate on par with the smallest sizing considered. The 1 mm size also gives the end plate an important characteristic in that it becomes two elements thick. This is important in the final results for studying end plate specific deformation effects. It allows stress and deformation values to be calculated through the thickness of the end plate on both the surface and interior. This creates a more clear definition of deformation.

Summarizing, the mesh convergence studies concluded that a fuel element mesh size of 3.5 mm and an end plate mesh size of 1 mm were acceptable parameters. The remainder of the model maintained the original mesh sizing from Section 7.5 with the exception of the endcaps, which were sized to 1.5 mm to improve the transition region between the fuel elements and end plate. At this point in the study the final model had been completed in terms of geometry, loads, boundary conditions, and material properties. It had a total of 952,366 nodes and took an average of 6 Hrs to solve with the computer setup specified in Section 6.3. The final step of model development was verification of the reported results along with establishing a benchmark to experimental data.

## **7.6 Model Benchmarking and Verification**

This section compares the developed model against post-irradiation data, and solid mechanics calculations to benchmark and verify its ability to produce accurate and expected deformation profiles. Even though post-irradiation data was only available for a latch based fuel channel without the F3SP modification, both models were compared. The observations from Section 7.5.1 revealed only minor deformation differences between the two models, suggesting their benchmarking results should also be similar. Additionally, the two models share identical loadings aside from downstream end plate boundary conditions. This was enough evidence to substantiate comparing both models to the data.

### **7.6.1 Solid Mechanics Verification**

The first step of this phase was to ensure the model results were in agreement with solid mechanics or basic physics calculations. Parts of the bundle with the simplest loading and boundary conditions were selected and the deformation before the initiation of creep and thermal expansion was calculated by hand. Deformation from thermal expansion and creep was left out, since it is complex and not easily calculable using solid mechanics. If the results from ANSYS™ were observed to deviate significantly from the calculation this was an easy way to determine that something in the model was not working properly. The fuel elements on the intermediate ring of the bundle were identified as the ideal component, because the applied loads on these fuel elements can be well represented as a simply supported beam. They are not in frictional contact with the pressure tube, nor is the axial constraint applied directly to them in either model. This prevents direct interference of the boundary conditions with the deflection of these fuel elements. The fuel element ends can then be represented as a simply supported beam with a pin connection at one end and a roller support at the other. The pin connection represents the downstream condition where axial support is indirectly provided by the fuel channel latches or shield plug. The roller connection represents the upstream end where pressure is applied by coolant and allows some axial movement. The pellet weight can then be applied as a distributed force along the length of the beam, while the axial load acts as a buckling force perpendicular to the pellet weight on the end of the beam. The representation of an intermediate fuel element as a simply supported beam is shown in Figure 53.

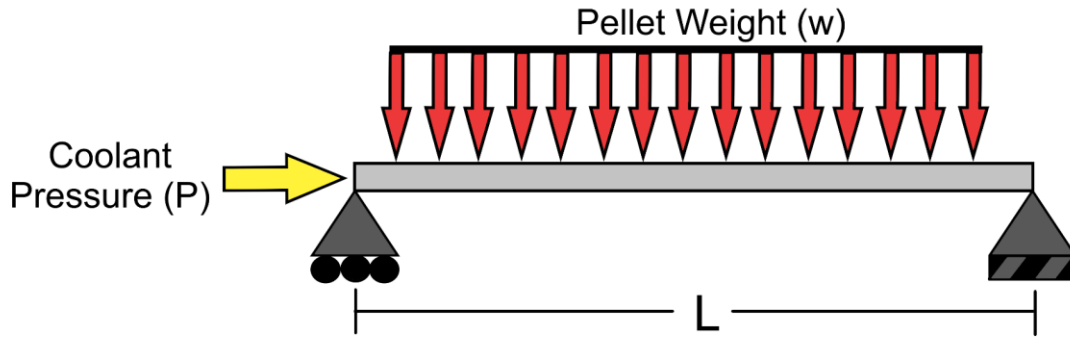


Figure 53: Simply Supported Beam Approximation for Intermediate Fuel Elements - Adapted from [48]

The midspan deflection of the fuel element was selected as the point of comparison between ANSYS™ and the solid mechanics calculation. The deflection was determined using the following equation [49][50].

$$\Delta_{\text{Midspan}} = \left( \frac{5wL^4}{384EI} \right) \left( \frac{1}{1 - \frac{P}{P_c}} \right) \quad (7)$$

The first term of the equation is the standard midpoint deflection for a simply supported beam, while the second term is a factor that accounts for an increase in midpoint deflection from an axial load [49][50]. In the first term  $E$  is the elastic modulus of the material,  $I$  is the beam's moment of inertia,  $L$  is the length of the beam, and  $w$  is the distributed load in force per unit length (N/mm). In the second term  $P$  is the axial load and  $P_c$  is the critical buckling factor, defined as the axial load that causes the beam to buckle.  $P_c$  is calculated by the critical Buckling Equation [50].

$$P_c = \frac{\pi^2 EI}{L^2} \quad (8)$$

To calculate the critical buckling factor for a hollow fuel element, the moment of inertia must first be determined using the equation for a hollow tube.

$$I_{\text{Hollow Tube}} = \frac{\pi}{64} (D_{\text{OD}}^4 - D_{\text{ID}}^4) \quad (9)$$

$$I_{\text{Fuel Element}} = \frac{\pi}{64} [(13.10 \text{ mm})^4 - (12.34 \text{ mm})^4] = 307.4 \text{ mm}^4$$

The Critical Buckling Factor can then be calculated using the Elastic Modulus at room temperature, since temperature effects were not included for verification.

$$E = 92.7 \text{ GPa}$$

$$I = 307.4 \text{ mm}^4$$

$$L = 495 \text{ mm}$$

$$P_C = \frac{\pi^2 EI}{L^2} = \frac{\pi^2 (92770 \text{ MPa})(307.4 \text{ mm}^4)}{(495 \text{ mm})^2} = 1149 \text{ N}$$

Having calculated the moment of inertia and Critical Buckling Factor, all the variables to solve the midpoint deflection equation are now known.

$$w = 6.5 \text{ N/Fuel Element} = 0.013 \text{ N/mm}$$

$$L = 495 \text{ mm}$$

$$E = 92.7 \text{ GPa}$$

$$I = 307.4 \text{ mm}^4$$

$$P_C = 1149 \text{ N}$$

$$P = 1.37 \text{ N (Equivalent Coolant Force on a Single Element)}$$

$$\Delta_{\text{Midspan}} = \left( \frac{5wL^4}{384EI} \right) \left( \frac{1}{1 - \frac{P}{P_C}} \right)$$

$$= \left( \frac{(5)(0.013 \text{ N/mm})(495 \text{ mm})^4}{(384)(92770 \text{ MPa})(307.4 \text{ mm}^4)} \right) \left( \frac{1}{1 - \frac{1.37 \text{ N}}{1149 \text{ N}}} \right) = 0.357 \text{ mm}$$

Using solid mechanics, the midspan vertical deformation for intermediate fuel elements is estimated to be 0.357 mm. Figure 54 shows the vertical deformation as determined by the latch supported bundle model. It highlights the midspan vertical deformation of intermediate fuel elements after the application of pellet weight and coolant pressure but before the initiation of thermal expansion and



creep. On initial inspection the solid mechanics calculation and model results are in close agreement. However, some of the fuel elements have deformation slightly under or over the calculated value. This difference is attributed to the results in the model being influenced by the weight and pressure against all of the fuel elements and not just those on the intermediate ring. The distribution of these loads through the end plate impacts the deformation reported by ANSYS™ for all elements due to sagging of the whole bundle. This in turn affects the deformation for the intermediate elements and is assessed as the key contributor to the differences between the model and solid mechanics calculation. Having accounted for these differences, the model is concluded to be in agreement with solid mechanics and deforming as expected.

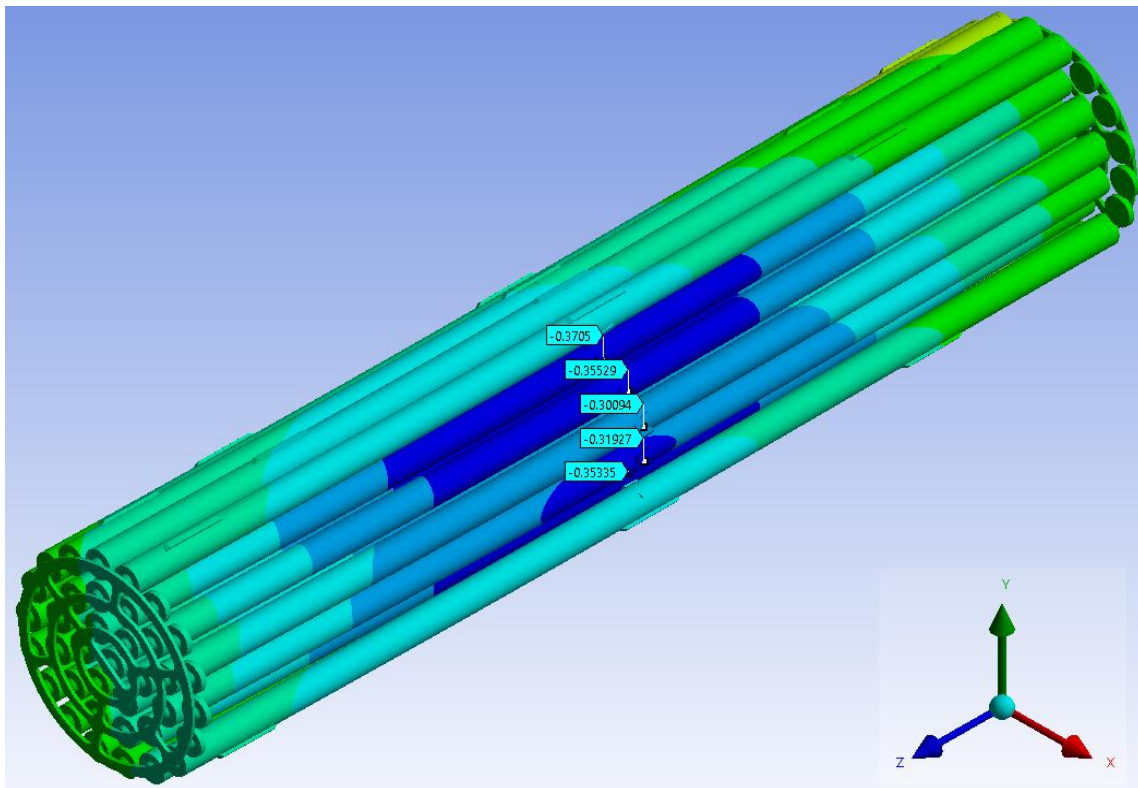


Figure 54: Midspan Vertical Deformation of Intermediate Fuel Elements in a Latch Supported Bundle for Solid Mechanics Verification – Pellet Weight and Coolant Pressure but no Creep or Thermal Expansion (mm, No Magnification)

## 7.6.2 Comparison with Post-Irradiation Data

The second point of comparison for the model was benchmarking its results against those obtained via post-irradiation analysis from a real bundle. The data in question was provided by COG and comes from bundle G85159W, which spent 24 months in a CANDU<sup>®</sup> reactor at the Bruce generating station in a high power position [31]. After being removed from the reactor the bundle spent time in a cooling pool before deformation measurements were made. Unfortunately, the exact measurements cannot be reported or discussed, since they are considered proprietary information. This means that all figures in this section are relegated to being qualitative and not quantitative. They are nevertheless still able to indicate how well the developed models predict the measured deformation shapes.

The three figures in this section compare the radial displacement of outer fuel elements between the two fuel bundle models for the different fuel channel supports and post-irradiation data. The three figures correspond to radial displacement profiles at three points along the length of the bundle. These are the quarter plane, midplane, and three quarter plane, moving from the upstream to the downstream end of the bundle. Since the available data was from a fuel channel without the F3SP modification, it was hypothesized that the latch model would be a better fit for the data. This proved to be somewhat false as is revealed in the figures.

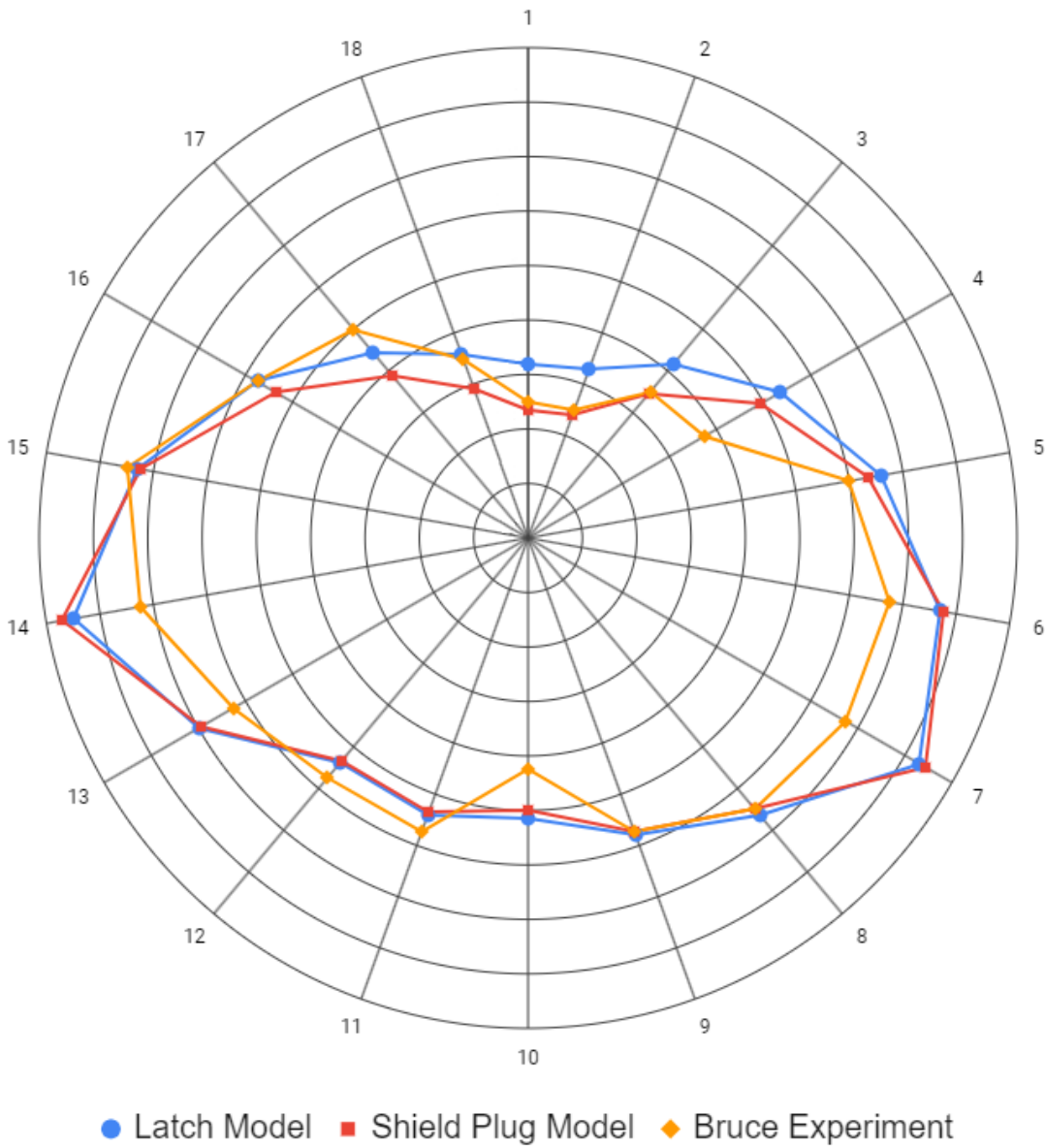


Figure 55: 37-Element Bundle Model comparisons to Post-Irradiation data – Radial displacement of Outer Fuel Elements at the bundle Quarter Plane – Radial axis scaled at 0.2 mm increments

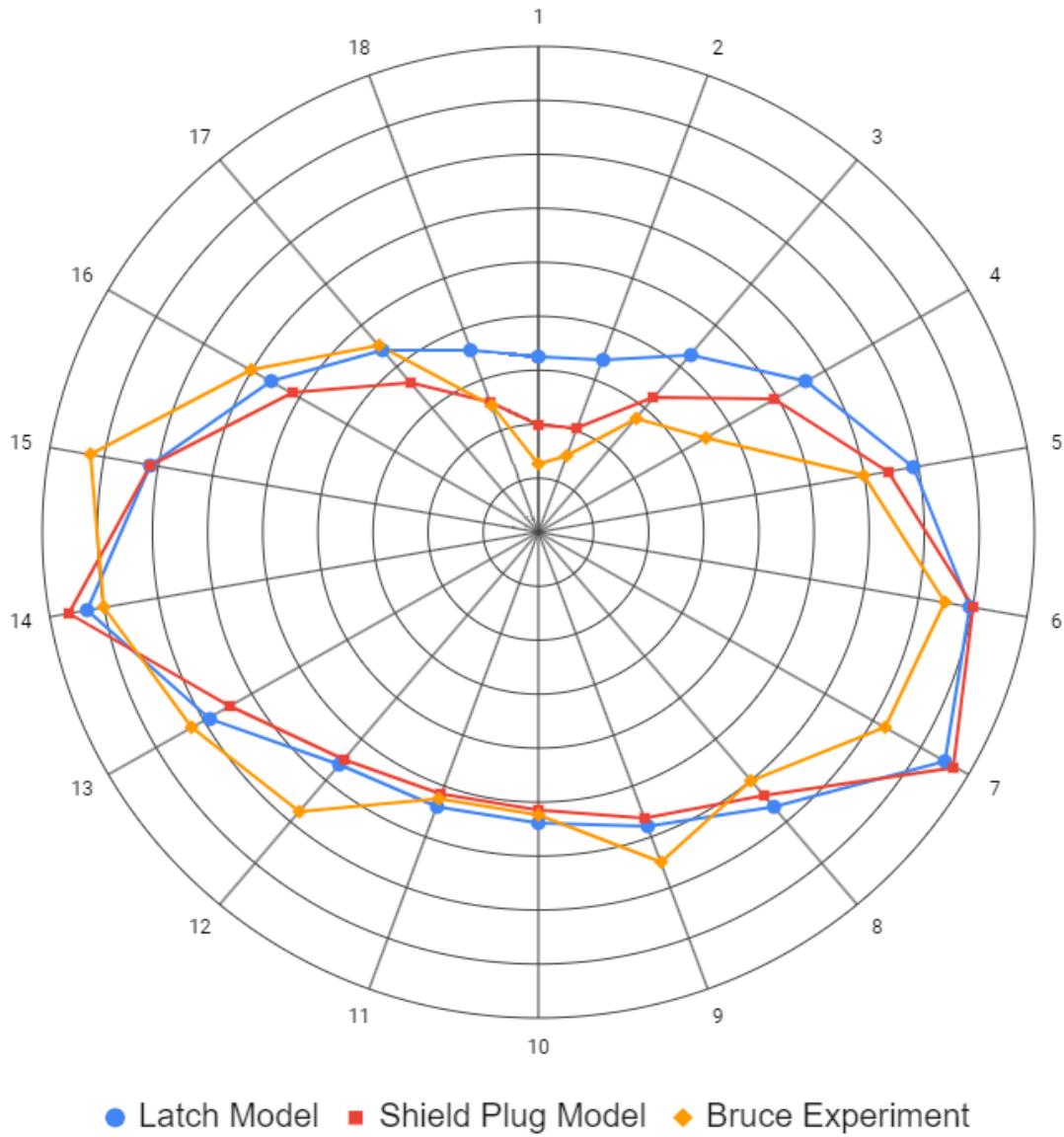


Figure 56: 37-Element Bundle Model comparisons to Post-Irradiation data – Radial displacement of Outer Fuel Elements at the bundle Midplane – Radial axis scaled at 0.2 mm increments

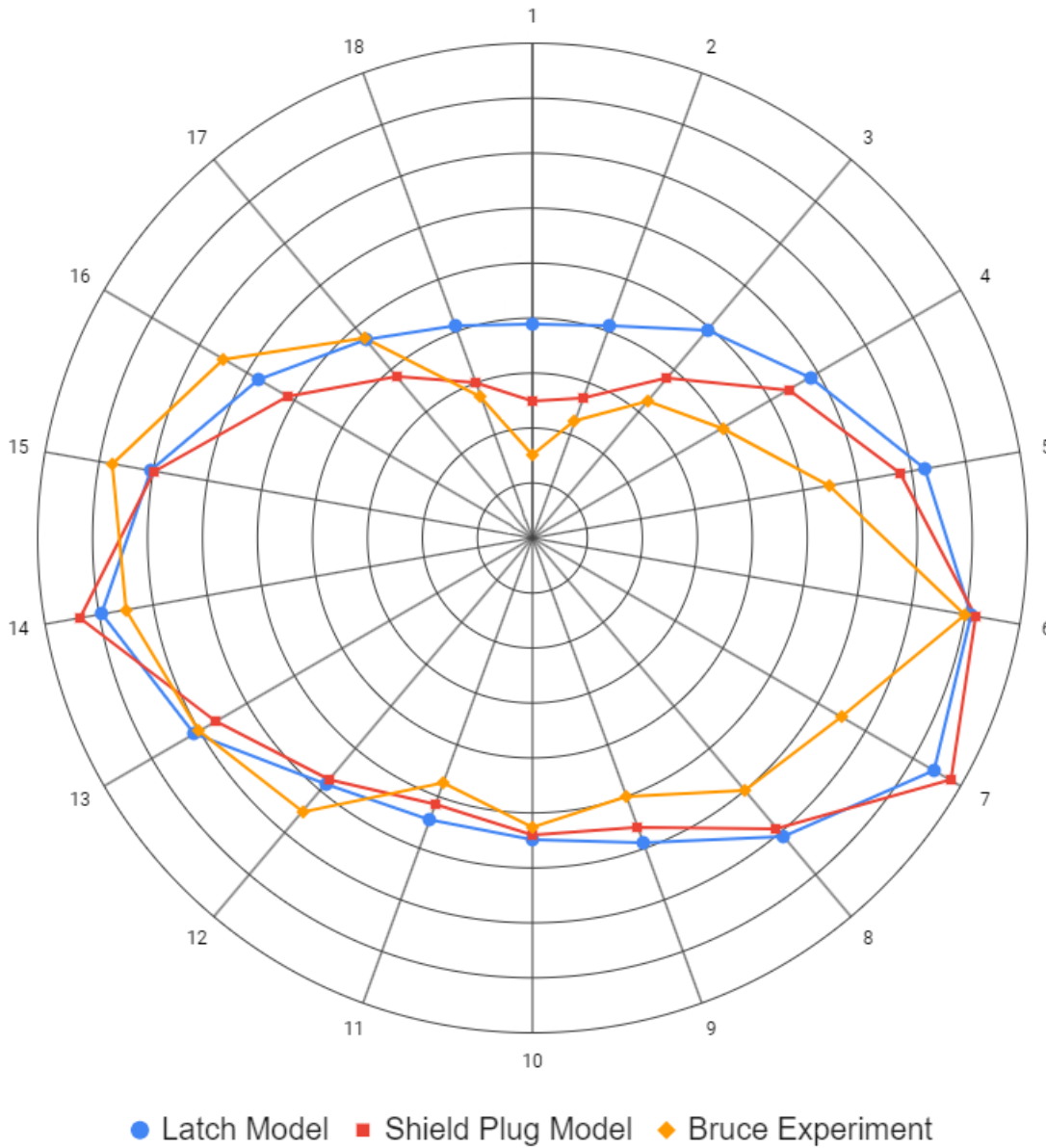


Figure 57: 37-Element Bundle Model comparisons to Post-Irradiation data – Radial displacement of Outer Fuel Elements at the bundle Three Quarter Plane – Radial axis scaled at 0.2 mm increments

The trend of the experimental data is reasonably predicted by both the latch and shield plug supported bundle models. However, the shield plug supported bundle more accurately recreates the deformation of the upper fuel elements. This means the shield plug model is actually a better fit for the data despite the data

itself being from a latch based fuel channel. As mentioned previously in Section 7.5.1, the increased deformation of the upper fuel elements in the shield plug model is correlated with the outer fuel element ends having a greater freedom of rotation at the end plate connection than in the latch model. This appears to be an important aspect of end plate boundary conditions, when it comes to reproducing the distinguished trough at the top of the bundle.

One key observation is that compared to the experimental data, model deformation is very symmetrical. The radial deformation profiles of Figures 55 to 57 show high symmetry in both the latch and shield plug model along the line denoting Elements 1 and 10. This symmetry was expected given that every aspect of each model is symmetrical, from material properties to loads and boundary conditions. Despite the symmetry, both models still follow the general shape of the experimental data across all three planes. This symmetry, however, results in the models being unable to account for some of the differences in deformation between the left and right sides of the bundle. The source of these differences is attributed to a number of factors, with the first being changes in fuel element stiffness with increased irradiation.

Radiation hardening and fuel pellet swelling are two factors known to increase fuel element stiffness, which varies by location in the bundle due to differences in neutron flux [21]. This non-uniform change in properties is hypothesized to affect local deformation rates and ultimately create asymmetric deformation profiles in spite of the otherwise symmetric load the bundles experience. Since radiation induced changes in material properties were not included in these models this may explain some of their inability to accurately predict deformation magnitudes in the experimental data. Incorporating pellet and radiation related effects is therefore expected to further improve the accuracy of the results produced by these models. The second factor is that there is an unknown contribution to deformation in the experimental data from strain relaxation and cooling that occurs between the bundle exiting the reactor and being measured. Whether this increases deformation or allows some of it to recover is unknown. Either way the experimental data is likely not accurate to the exact deformation characteristics of the bundle at the time it was removed from the reactor.

The third factor is that an estimation had to be made to establish an equivalent creep duration in the models for comparison to the data. Since the creep constants had been adjusted to allow for more reasonable simulation times in

Section 7.1, a 1:1 creep duration could not be used and an approximation was needed using a reference point. The chosen point was the midplane radial displacement of fuel elements at the 6 o'clock position of the bundle. These fuel elements are the only part of the bundle where the direction of displacement reverses as creep increases. The midplane of the bottom elements initially bows upwards in response to pellet weight but eventually starts to bow down back towards the pressure tube once spacer pad contact initiates in the lower elements. Using this observation, the models were assumed to have experienced similar amounts of creep once the bottom elements had reached the same midplane radial displacement as the experimental data. Use of this reference point proved to be reasonable since the remaining data fell within small margins of the values predicted by the models. Nevertheless, this method of approximating creep duration was not perfect and may also explain some of the deviations of the models from the data. Even though the experimental profiles could not be perfectly recreated, these models can still predict several of the expected deformation characteristics. The general deformed bundle shape in the data is able to be reasonably recreated by the models in spite of some sources of error and the omission of certain material factors. Thus for the sole purpose of studying deformation trends and not predicting exact values, the models are an excellent benchmark.

## 8. End Plate Deformation Analysis

This section contains the main results from the study, depicting the expected end plate stress and deformation effects using the benchmarked model from Section 7.6. The reference point based creep duration, along with the various loadings from Section 7 were carried forward for all results presented here. The general end plate deformation observations are presented first in Section 8.1, comparing the latch and shield plug models through vertical deformation, axial deformation, and Von-Mises stress. Section 8.2 compares the effects of end plate orientation on deformation through 120 degrees of rotation, using the vertical deformation of both fuel elements and the end plate. Section 8.3 shows the impact of increasing end plate thickness on both the deformation of the end plate as well as the whole bundle. Only the shield plug models are used in the end plate orientation and thickness studies since the corresponding boundary conditions are the ones currently being used in CANDU<sup>®</sup> 6 and BNGS reactors. Section 9 discusses these results in the larger context of end plate design and bundle deformation.

### 8.1 End Plate Deformation at NOC

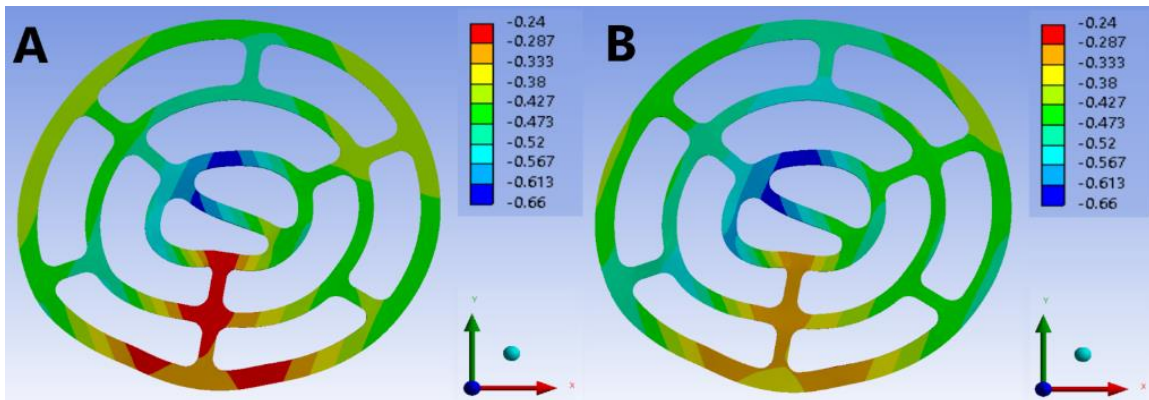


Figure 58: Comparison of Upstream Endplate Vertical deformation at NOC for Latch (A) and Shield Plug (B) Supported Bundles (mm, 15X Magnification)

In Figure 58 attention should be paid to how similar the contour plots are between the two images. Vertical deformation of the upstream end plate is near identical between the two models indicating that axial support provided by the fuel channel has a limited impact on vertical deformation of the end plate.



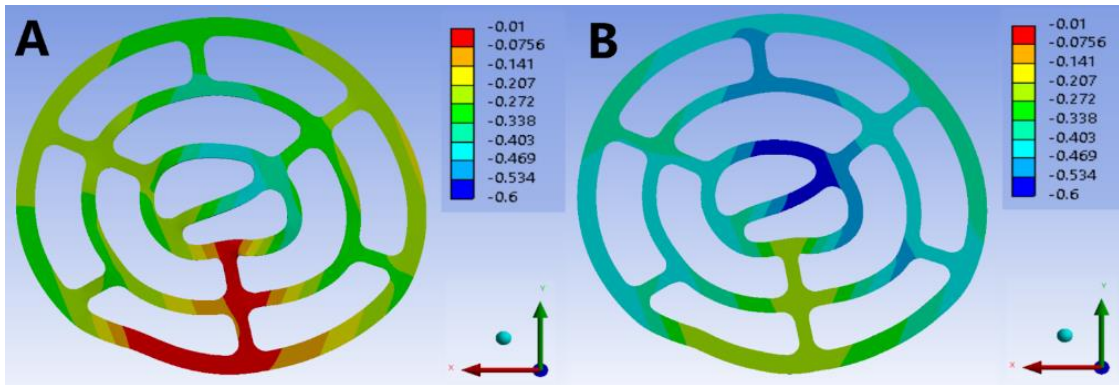


Figure 59: Comparison of Downstream Endplate Vertical deformation at NOC for Latch (A) and Shield Plug (B) Supported Bundles (mm, 15X Magnification)

In Figure 59 attention is again focused on the similarity of contour plots between the two models. The magnitudes of vertical deformation differ, but the transitions in scale of deformation through the end plate are highly comparable. With regards to the difference in magnitudes, the scale is small enough that although the color difference looks large, the numerical difference is only around 0.1 mm. This shows that vertical deformation in the downstream end plate is minimally affected by the axial support from the fuel channel.

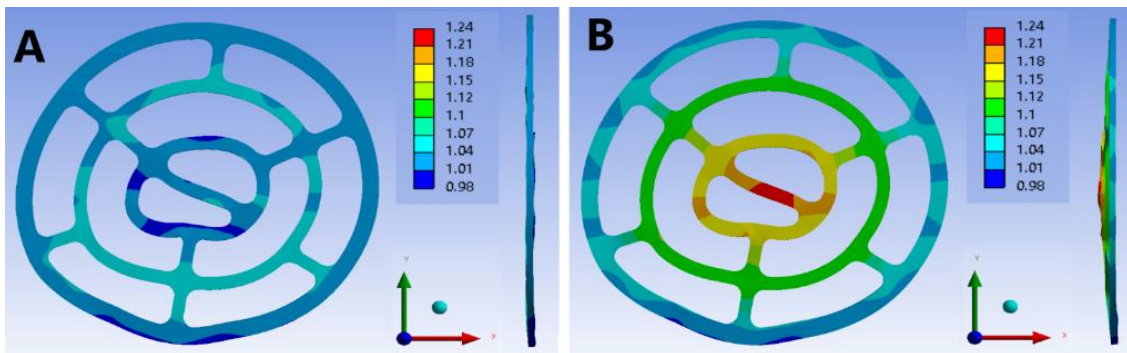


Figure 60: Comparison of Upstream Endplate Axial deformation at NOC for Latch (A) and Shield Plug (B) Supported Bundles (mm, 15X Magnification)

Figure 60 clearly defines the difference in axial deformation on the upstream end plate between the latch and shield plug supports. Flattening and the beginning of dishing is observed with latch support while doming is observed with shield plug support.

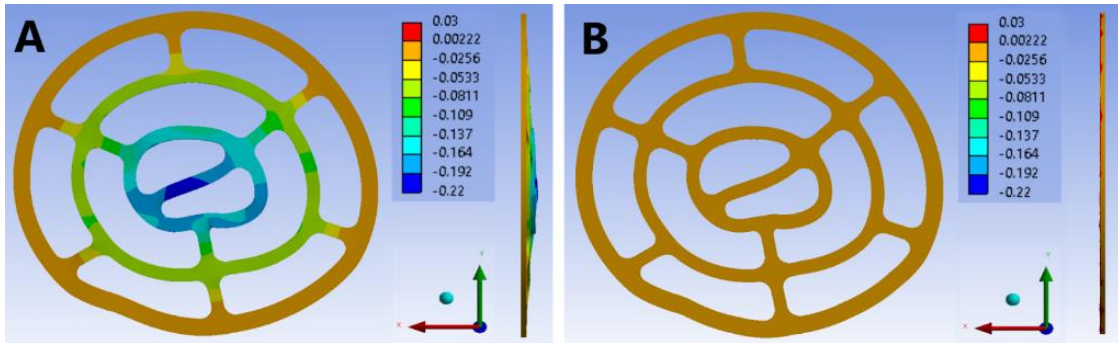


Figure 61: Comparison of Downstream Endplate Axial deformation at NOC for Latch (A) and Shield Plug (B) Supported Bundles (mm, 15X Magnification)

Figure 61 makes clear the difference in downstream end plate axial deformation with the latch model exhibiting clear doming as the result of coolant pressure. The shield plug model has no meaningful axial deformation due to the highly restrictive boundary condition from the F3SP nose piece. It fully supports the rings of the end plate and prevents out of plane movement.

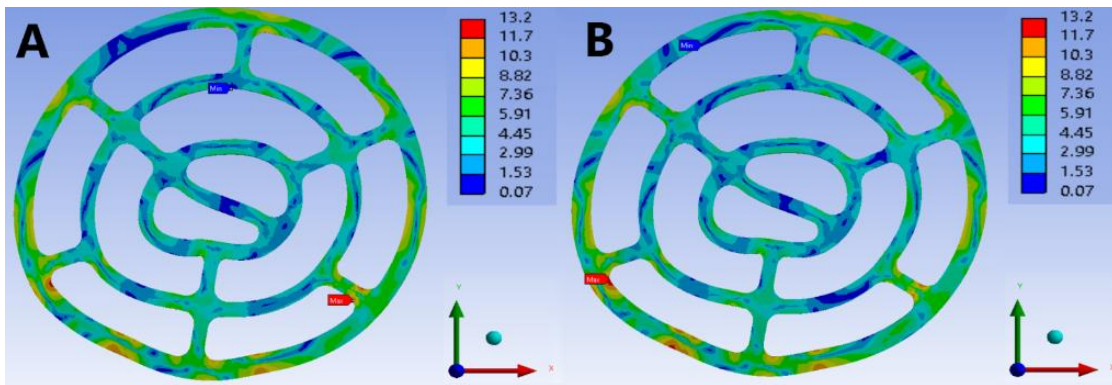


Figure 62: Comparison of Upstream Endplate Von Mises Stress at NOC for Latch (A) and Shield Plug (B) Supported Bundles (MPa, 15X Magnification)

Figure 62 shows that there is a negligible difference in stress distribution and magnitude in the upstream end plate between the latch and shield plug models. The contour plots between the two are almost indistinguishable.

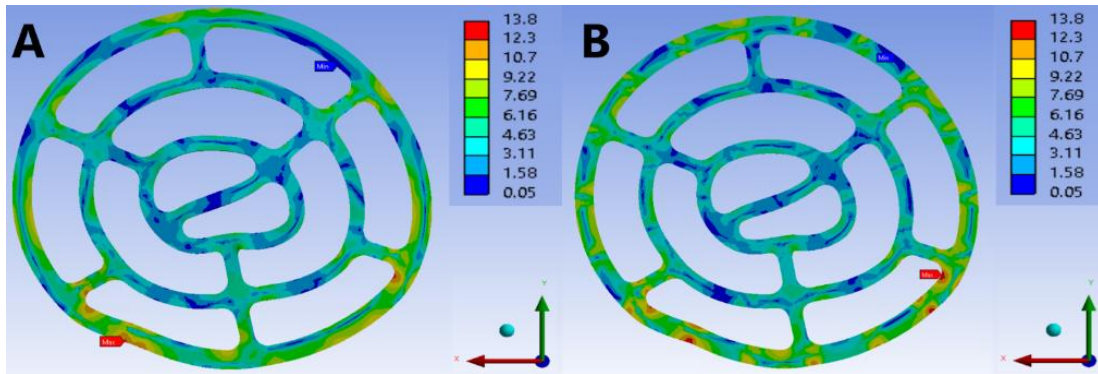


Figure 63: Comparison of Downstream Endplate Von Mises Stress at NOC for Latch (A) and Shield Plug (B) Supported Bundles (MPa, 15X Magnification)

Similar to Figure 62, Figure 63 shows that the stress distribution in the downstream end plate between the two models is also highly comparable. The shield plug supported bundle does have more notable stress spikes at the points of fuel element connections due to the restrictive nature of the associated boundary condition. This is because it reduces the ability of the end plate to twist at the connections to the fuel elements. However, the overall stress magnitudes are still very similar between the models and not sufficiently larger in the shield plug supported bundle to warrant further investigation.

## 8.2 Effect of Bundle Orientation on Deformation

Table 5: Effects of Bundle / End Plate Orientation on Vertical Deformation

Note the increase in deformation of fuel elements and distortion of the end plate as the orientation of the bundle changes.

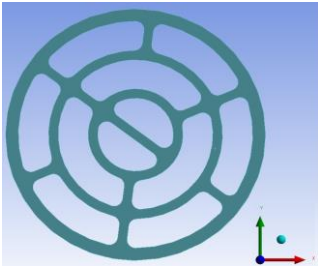
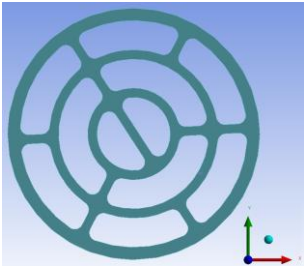
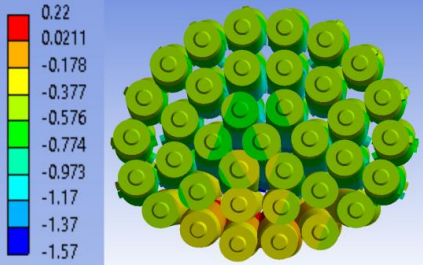
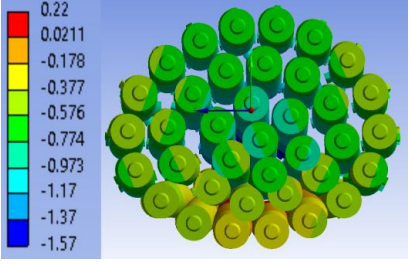
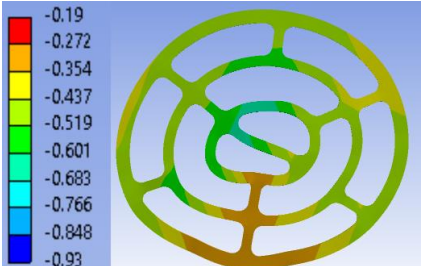
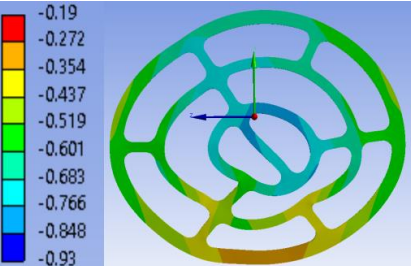
Bundle Rotation	0°	20°
End Plate Orientation		
Vertical Deformation of Fuel Elements 15X Magnification (mm)		
Vertical Deformation of Upstream End Plate 15X Magnification (mm)		



Table 5: Effects of Bundle / End Plate Orientation on Vertical Deformation Cont'd

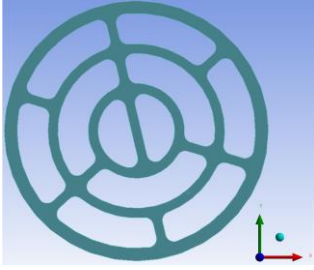
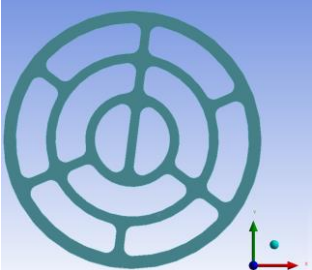
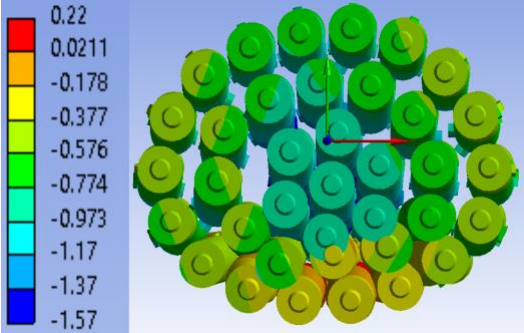
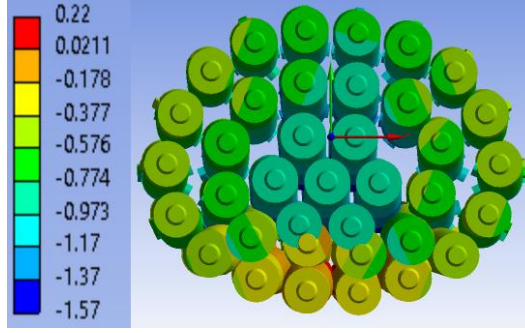
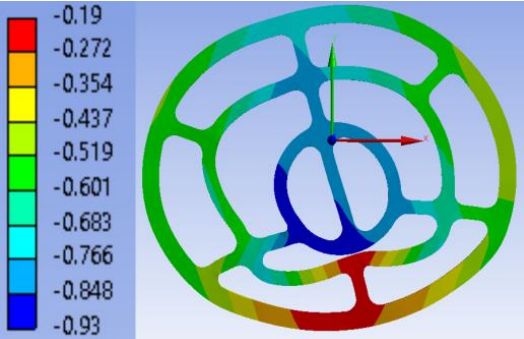
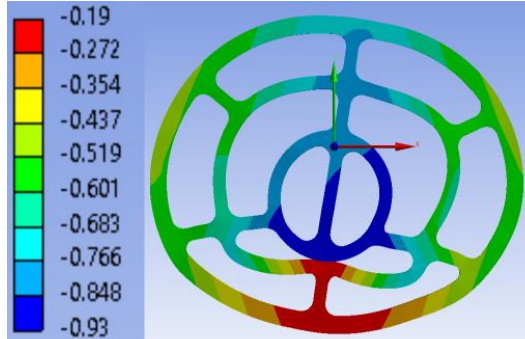
Bundle Rotation	40°	60°
End Plate Orientation		
Vertical Deformation of Fuel Elements 15X Magnification (mm)		
Vertical Deformation of Upstream End Plate 15X Magnification (mm)		

Table 5: Effects of Bundle / End Plate Orientation on Vertical Deformation Cont'd

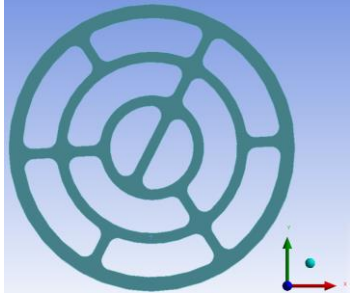
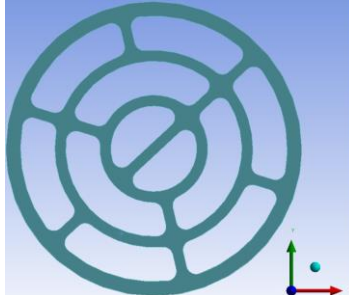
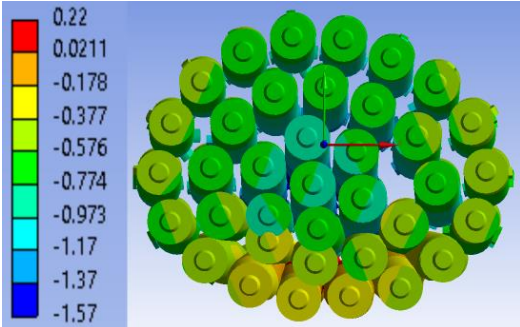
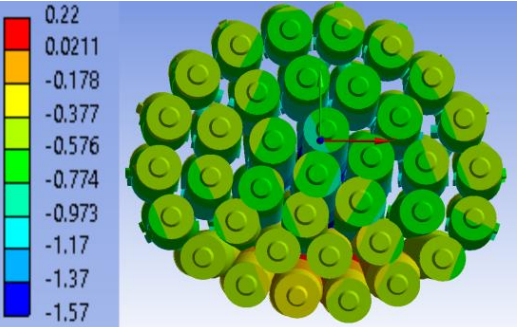
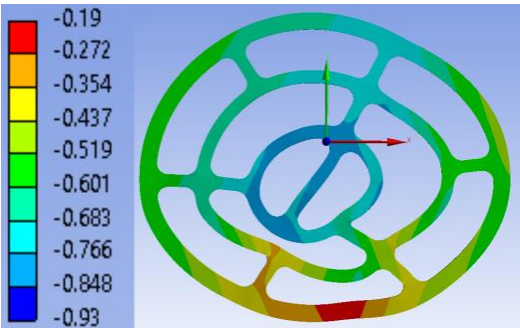
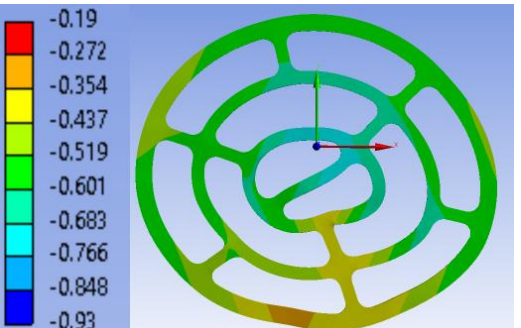
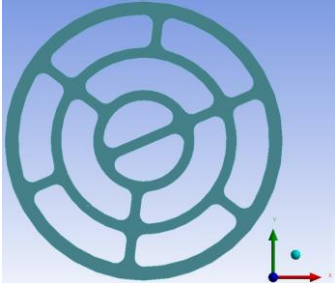
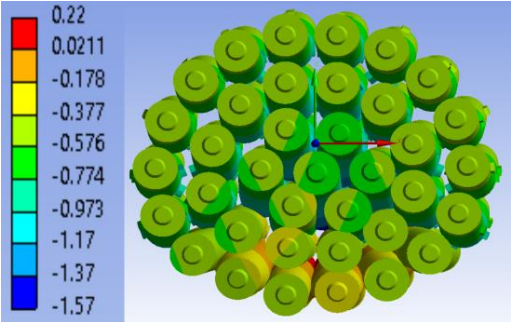
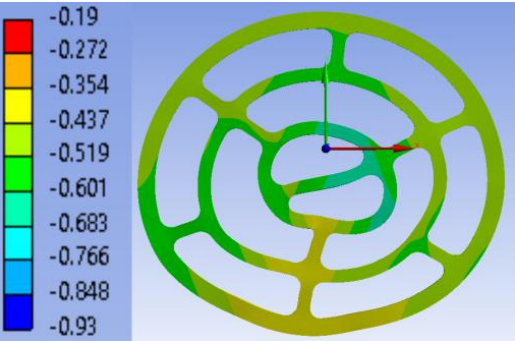
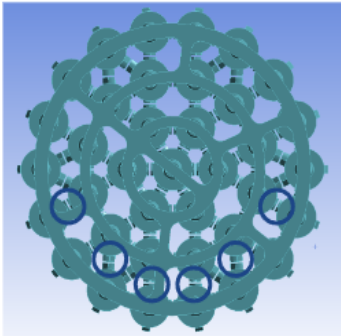
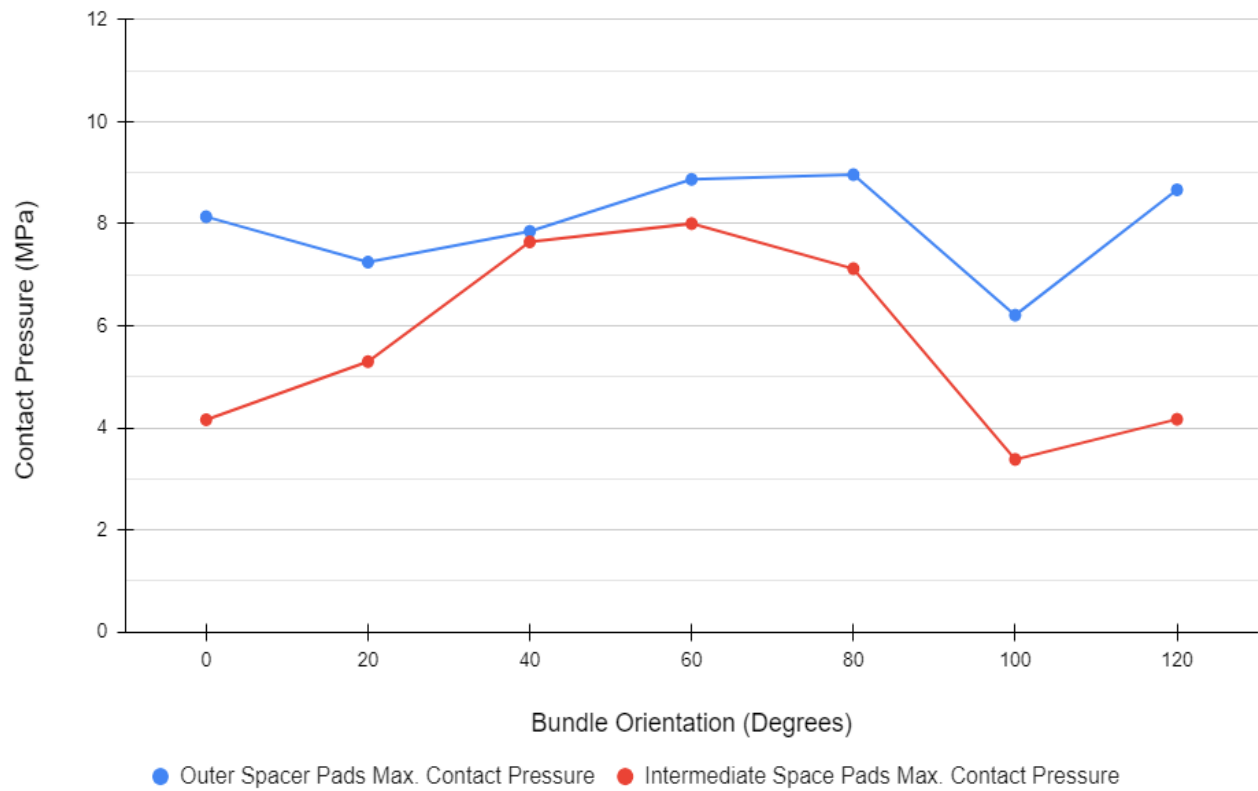
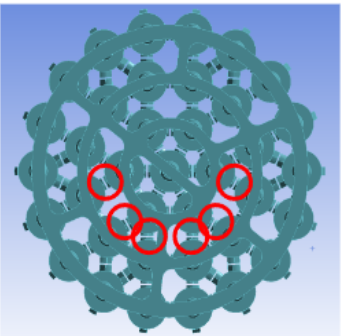
Bundle Rotation	80°	100°
End Plate Orientation		
Vertical Deformation of Fuel Elements at 15X Magnification (mm)		
Vertical Deformation of Upstream End Plate at 15X Magnification (mm)		

Table 5: Effects of Bundle / End Plate Orientation on Vertical Deformation Cont'd

Bundle Rotation	120°
End Plate Orientation	
Vertical Deformation of Fuel Elements at 15X Magnification (mm)	
Vertical Deformation of Upstream End Plate 15X Magnification (mm)	



Outer Spacer Pads



Intermediate Spacer Pads

Figure 64: Effect of Bundle Orientation on Spacer Pad Contact Pressure

In Figure 64 it is important to note how the spacer pad contact pressure experiences a sharp increase in the 40° to 80° orientations when there is no major end plate web in direct vertical support of the center end plate ring. The location of each type of spacer pad is identified in the images to the right of the graph.



### 8.3 Effect of End Plate Thickness on Deformation

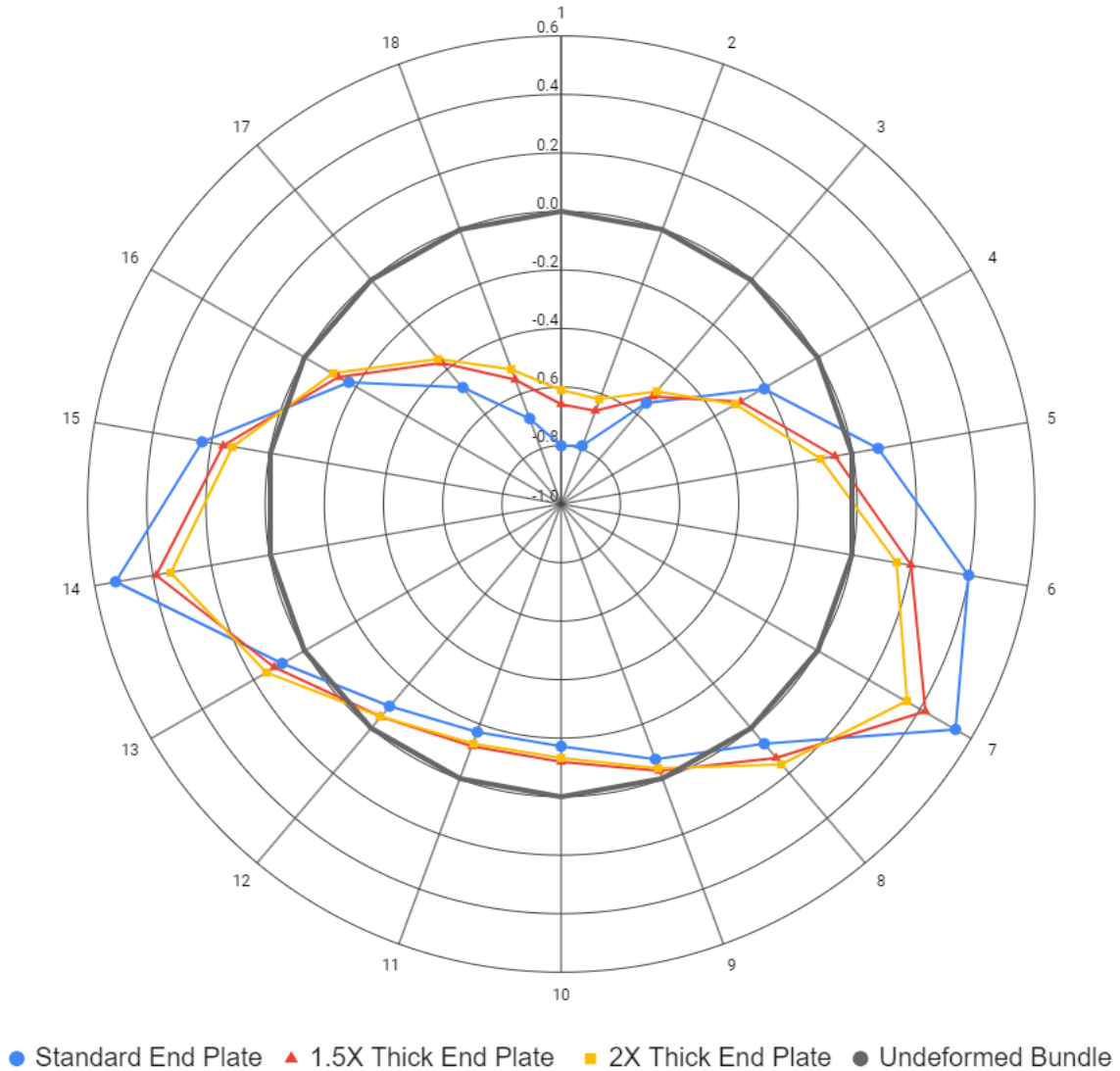


Figure 65: Effect of Increased End Plate Thickness on Midplane radial displacement of Outer Fuel Elements (mm)

In Figure 65, bundles with increased end plate thickness are observed to have reduced radial displacement and thus less overall deformation than bundles with the nominal end plate thickness. This is observed as the yellow and red lines being closer to the undeformed (black line) shape of the bundle.

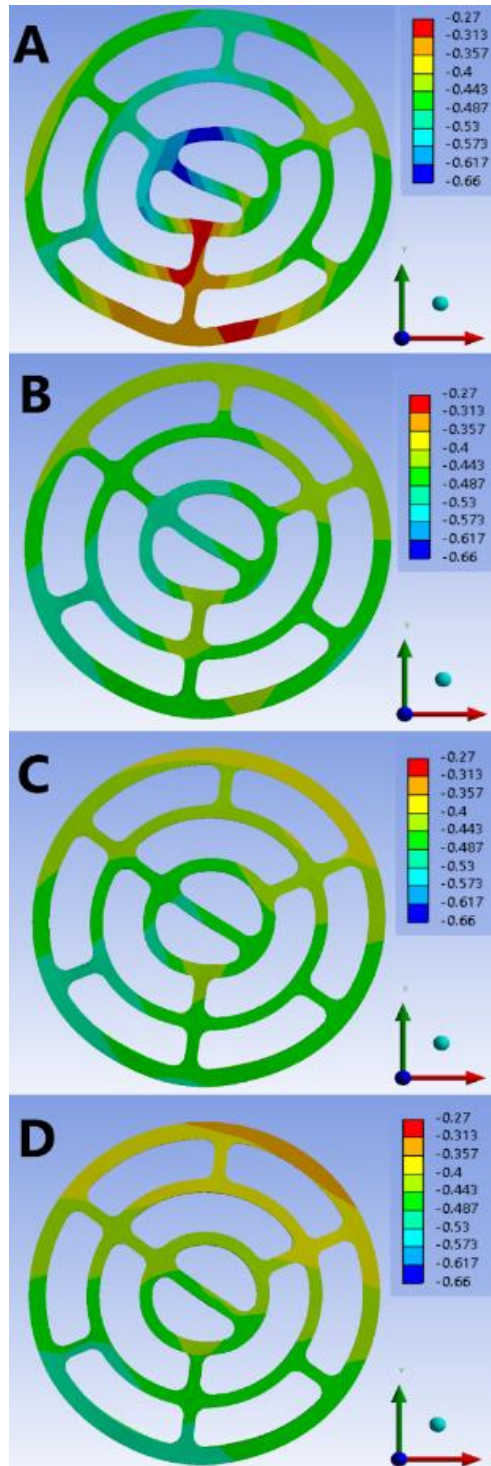


Figure 66: End Plate Thickness Vs. Vertical Deformation of Upstream End Plate – Nominal End Plate (A), 25% Thicker End Plate (B), 50% Thicker End Plate (C), and 100% Thicker End Plate (D) (mm, 15X Magnification)

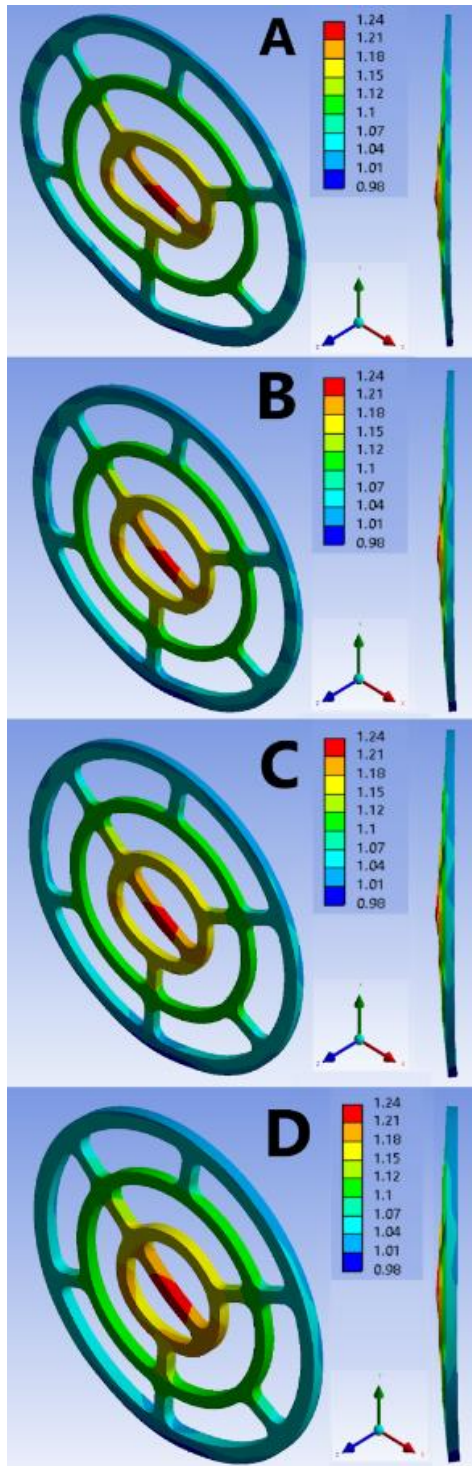


Figure 67: End Plate Thickness Vs. Axial Deformation of Upstream End Plate Nominal End Plate (A), 25% Thicker End Plate (B), 50% Thicker End Plate (C), and 100% Thicker End Plate (D) (mm, 15X Magnification)

## 9. Discussion

### 9.1 End Plate Deformation at NOC

Based on the assumptions and results of the model, end plate deformation at NOC does contribute to overall bundle performance and deformation. Movement within the end plates is small but contributes to the sagging effect experienced by the whole bundle. The end plates were never observed to buckle but the vertical compression did distort the end plate's concentricity and moderately decreased the distance between all three rings. This could have an effect on coolant flow through the bundle as the distortion may add additional impedance to coolant flow through sub channels. The largest deformation and stresses in the end plate concentrate in the center ring and lower webs where the partial weight of the bundle is transferred to the bottom fuel elements and pressure tube. This suggests that cracking and failure is likely to start in these locations. Between the upstream and downstream end plates, vertical deformation has high side-to-side symmetry, which is reflective of the uniform loading and material properties in the models. Vertical end plate deformation is also observed to be similar between the shield plug and latch based fuel channel architectures, despite the difference in boundary conditions. This indicates that the F3SP modification likely has no effect on bundle sag and primarily limits axial deformation.

Where deformation differs between the upstream and downstream end plates is in the axial deformation. As mentioned during model development in Section 7.5.1, the latch model exhibits a dishing and doming effect in the direction of coolant flow for the upstream and downstream end plates respectively. These effects are more distinct at pressures greater than the 3600 Pa dynamic coolant pressure and would be expected if a hydraulic drag load had been included. The shield plug supported bundle however, only experiences a doming effect on the upstream end plate with no axial deformation on the downstream end plate due to F3SP boundary conditions. This indicates the F3SP modification is likely to reduce end plate deformation by preventing doming of the downstream end plate. This comes at the expense of increased deformation of the upstream end plate through thermal expansion. Although the doming of the upstream end plate is noticeable with a shield plug supported bundle, there is no additional force to increase this doming through creep over the bundle's life in the reactor. The

coolant force acts against this doming effect and therefore it is not expected to compromise the end plate or bundle in a significant way. The mitigation of axial end plate deformation through the adoption of the F3SP is thus supported by these results. It is perceived that this fuel channel modification is working to effectively combat end plate cracking.

The maximum end plate stress is found in the corners of the lower webs near the bottom of the pressure tube, while localized bending at the fuel element connections causes minor stress spikes at those locations. These observations apply to both latch and shield plug supported bundles. Maximum stress in the end plates is significantly higher before the initiation of creep than after the bundle has been deformed. By the time the expected deformation values are reached for a bundle exiting the reactor, the maximum stress in the end plate has decreased by 87%. This is the result of contact changes between the bundle and pressure tube. Initially only 6 bearing pads on the two bottom elements are in contact with the tube, but deformation through creep eventually causes parts of 12 bearing pads to contact the tube. This distributes the bundle weight over more fuel elements and reduces the force being transferred through the end plate. The resulting reduction in stress slows the rate of deformation in the end plate, and by association, the sag of the bundle. This means that deformation of both the end plate and bundle through creep slows over time and with increasing burnup. The greater implication is that deformation is fastest during the early stages of the bundle's life in the reactor.

## **9.2 Effects of Bundle Orientation on Deformation**

The results of Table 5 show that the orientation of the bundle in the pressure tube does affect the deformation exhibited by both the fuel elements and end plate. The location of the major end plate webs with respect to the bottom of the pressure tube is the determining factor for whether deformation increases or decreases for each orientation. There are three of these major webs in the studied end plate design and they connect the outer ring and inner rings of the end plate. When one of these primary webs is not close to vertical or in the direction of gravity this increases vertical deformation, particularly for the center of the bundle. This is because there is no direct support for the center ring in this orientation, which causes a greater amount of sag and distortion in the end plate. Orientations of 40° through 80° from the nominal orientation exacerbated this effect with the 60° orientation causing maximum deformation to rise by 54 %.

Increased end plate deformation in the center ring also caused increased fuel element deformation and contact between spacer pads in the lower half of the bundle. From the 0° to 60° model, the maximum contact pressure between spacer pads in the lower elements increased by 9%, while contact pressure in the intermediate spacer pads doubled. The increased center ring deformation and spacer pad contact may have implications for coolant flow and heighten the risk of spacer pad fretting. A separate investigation into this using Computational Fluid Dynamics (CFD) would reveal what impacts there are to cooling effects from the different orientations. Overall these observations suggest that controlling bundle orientation may have advantages for limiting deformation.

To mitigate deformation in bundles with this end plate design, the ideal orientation is to have at least one of the major webs near vertical and parallel to gravity. In Table 5 this orientation corresponds to rotations of 0° and 120°. Maintaining this orientation provides improved support for the center ring of the end plate to better resist the weight of the fuel elements. The effects of controlling orientation are mainly limited to the center elements and lower half of the fuel bundle. The higher number of secondary webs between the intermediate and outer ring of the end plate was found to result in consistent deformation of the outer fuel elements in all orientations. They were spaced close enough that no matter the orientation of the bundle the support provided by the end plate in these areas varied minutely. As a result, this feature is assessed to be an effective part of the end plate design and should be maintained in the event of future modifications. As developed, the current model could be easily adjusted to use any number of new end plate designs to determine if and how orientation may affect deformation.

### **9.3 Effects of End Plate Thickness on Deformation**

The results of Section 8.3 indicate that increasing the thickness of the endplate does have a notable effect on the vertical deformation experienced by the bundle. Increasing end plate thickness up to twice the nominal thickness was seen to decrease maximum vertical end plate deformation by 21% and eliminate much of the concentric distortion. This meant the end plate was better able to maintain its shape and by association, subchannel flow area. This is supported by the visible reduction in fuel element deformation from Figure 65. On average a 50% thicker end plate was able to reduce the deformation of all outer fuel elements by approximately 15%. An end plate with twice the nominal thickness

achieved only marginally better reduction in deformation than a 50% thicker end plate despite the greater amount of material. As such, increasing end plate thickness beyond this value was found to offer little further advantage. This indicated that a limit was approached whereby further increases to end plate thickness would not continue to reduce deformation. The end plate became stiff enough that with a 50% increase in thickness it no longer experienced significant internal deformation. The end plate merely sagged with the fuel elements while maintaining its own shape. This suggests that a 50% thicker end plate is likely to be a worthwhile modification to this end plate design.

The doming of the upstream end plate through thermal expansion was largely unchanged by the increased end plate thickness. This is believed to be due to both the thermal expansion being the predominant force causing axial deformation and that the direction of that force acts perpendicular to the end plate face. The geometry of the end plate is such that it is stronger in plane than out of plane meaning that it will always be able to better resist vertical loads than axial loads. The weight of the bundle acts against the in-plane direction of the end plate, while the force from thermal expansion is only counteracted by the thickness and is imparted in the out of plane direction. As a result, a minute increase in end plate thickness improves resistance to vertical loads and sagging of the bundle, but does little to reduce axial deformation through thermal expansion. This is assessed as the reason for consistent axial deformation of the end plate for all evaluated increases in end plate thickness as seen in Figure 67. Increasing end plate thickness therefore reduces vertical deformation of both the end plate and bundle as a whole, but will have limited ability to combat dishing and doming effects to the same extent. These results conclude that the adoption of a thicker end plate is a worthwhile modification for reduced concentric deformation and vertical compression of the bundle.

## 10. Conclusions

This study added to the 37-Element CANDU® Fuel Bundle model being developed by RMC by refining boundary conditions and loading to develop a model for studying the effects of end plates in bundle deformation. A model with coolant pressure, end flux peaking temperatures, pellet weight, creep, realistic end plate constraints, and frictional contact between all bodies was constructed. It produced expected deformation characteristics as confirmed through comparison to experimental post-irradiation data. The final model used hollow fuel elements to reduce computational load, since increased creep was able to produce similar deformation profiles in models with solid fuel elements. Exploration of differences in bundle deformation between latch and F3SP fuel channel architectures was completed and indicated that dishing and doming of end plates was reduced by the F3SP modification. Furthermore, the model with F3SP constraints was found to be the best fit for post-irradiation data. It accurately recreated the trough and upward bow of fuel elements at the top and bottom of the bundle, respectively.

Under NOC and standard burnups the final model showed end plates deform by compressing vertically to cause concentric distortion and contribute to overall sag of the bundle. Vertical deformation and stresses in both the upstream and downstream end plates were observed to be highly comparable. Stresses concentrated in corners of the lower webs, while deformation was most prevalent in the center of the end plate. The deformation in the center of the end plate was exacerbated when bundle orientation was altered and it was found that controlling orientation was able to reduce this deformation by up to 54%. Vertical alignment of one of the major end plate webs was associated with being able to best limit this deformation. Thicker end plates were also observed to help reduce both fuel element and end plate deformation in the vertical direction. Thickening the end plate by 50% reduced outer fuel element deflection at the midplane by an average of 15% and maximum vertical end plate compression by 21%. Increasing end plate thickness beyond this value had little further advantage in combating deformation. Incorporation of radiation and pellet stiffening effects are seen as the most important addition for future development of this model.



## 11. Recommendations

There are two recommendations from this study with respect to the industry perspective. The first is to consider controlling orientation of bundles loaded into the reactor as a way of mitigating deformation. This was shown by the model to limit deformation in the center of the bundle with the potential to improve coolant flow and reduce fretting of intermediate spacer pads. The second recommendation is to adopt a 50% thicker end plate. A thicker end plate was shown to eliminate much of the end plate distortion but also reduce deflection in outer fuel elements. Combined, both of these recommendations will not eliminate the concerns that stem from bundle deformation, but should work proactively to mitigate them.

The feasibility of controlling both orientation and increasing end plate thickness will still need to be evaluated in other perspectives. Controlling bundle orientation in the fueling machine may not be something that is actually achievable with the rotary action of the magazine that holds the bundles. It may in turn be better to simply design a perfectly symmetrical end plate to ensure the deformation effects are the same no matter the orientation of the bundle in the fuel channel. Increasing end plate thickness will increase the total length of the fuel string and could also impact neutron flux at the ends of the bundle with addition of more material. Accordingly this improvement will also require further evaluation to ensure that the benefits of increasing the end plate thickness do not result in consequences that outweigh them.

With respect to future work there are several recommendations for additional studies and modifications to be made with this model. They are as follows:

1. With a benchmarked and partially validated model, studies can now be completed to look at the effects of high burnup on bundle deformation. This model made use of modified creep constants to accelerate deformation rates with an experimentally benchmarked duration. However, the model could now be used to estimate deformation over longer timelines. As is the case for the results of this study, caution would need to be exercised due to the model's current omission of pellets and changes in material properties known to occur with increased irradiation.

2. Alternative end plate designs can now be studied using this model as a basis to ascertain the advantages they may pose over the current design. The skewed web end plate from the enhanced CANDU® fuel bundle in Figure 6 could easily be incorporated into this model and evaluated under the same orientation and thickness conditions presented in Section 8 [13].
3. A CFD analysis could be developed based on this model to evaluate the effects of heat transfer and heat generation in a deformed bundle. This is a critical step that has yet to be taken by RMC but would provide a plethora of new information.
4. This model can now be used to study deformation effects in the bundle beyond just end plates. Having a set of working and partially validated boundary conditions there are many more parametric studies that can be completed on the bundle. These include bearing pad and spacer pad contact, fuel element diameter and wall thickness, and different temperature profiles.
5. Lastly, there are several areas for direct improvement to the model that would enhance its ability to predict experimental results. First and foremost, an approximation of fuel pellets using UO<sub>2</sub> material properties would better represent the fuel element stiffness and lead to a more realistic model. If the associated changes in properties due to radiation could also be included this would likely further reduce the difference between the model and experimental data. Direct modeling of pellets will be burdensome but prescribing different properties along the length of each fuel element may be a potential solution to this problem. Changes in Zircaloy-4 material properties from irradiation should also be further investigated and not be wholly ignored, since they will also have an effect on bundle deformation rates. Finally, an approximation for the average coolant drag loading needs to be estimated and coupled with the dynamic pressure loading. The drag loading is complex and changes with the bundle's location in the fuel channel. An average drag estimation will improve the accuracy of the coolant load. It will also increase the associated deformation effects given it is expected to be greater than the dynamic pressure load the model currently uses.

## 12. References

- [1] “Statistical Review of World Energy 2021,” *British Petroleum*. 2021. [Online]. Available: <https://www.bp.com/content/dam/bp/business-sites/en/global/corporate/pdfs/energy-economics/statistical-review/bp-stats-review-2021-full-report.pdf>
- [2] J. Rogelj et al, “Global Warming of 1.5°C - Chapter 2 Mitigation Pathways Compatible with 1.5°C in the Context of Sustainable Development,” *The Intergovernmental Panel on Climate Change*. 2018.
- [3] M. Collins et al, “Climate Change 2013: The Physical Science Basis - Chapter 12 Long-term Climate Change: Projections, Commitments and Irreversibility,” *Cambridge University Press, Cambridge, UK and New York, USA*. 2013.
- [4] “Global Temperature and Carbon Dioxide,” *U.S Global Change Research Program*. 2009. [Online]. Available: <https://www.globalchange.gov/browse/multimedia/global-temperature-and-carbon-dioxide>
- [5] S. Wappelhorst, “Update on Government Targets for Phasing Out New Sales of Internal Combustion Engine Passenger Cars,” *The International Council on Clean Transportation (ICCT)*. [Online]. 2021. Available: <https://theicct.org/publication/update-on-government-targets-for-phasing-out-new-sales-of-internal-combustion-engine-passenger-cars/>
- [6] M. Shellenberger, “The Nuclear Option: Renewables Can’t Save the Planet - but Uranium Can,” *Council on Foreign Relations - Foreign Affairs*, (96-5), 159-165. 2017.
- [7] M. Mueller, “Nuclear Power is the Most Reliable Energy Source and It’s Not Even Close,” *US Department of Energy - Office of Nuclear Energy*. 2021. [Online]. Available: <https://www.energy.gov/ne/articles/nuclear-power-most-reliable-energy-source-and-its-not-even-close>

- [8] W.M.J. Garland, "The Essential CANDU: A Textbook on the CANDU Nuclear Power plant Technology," *University Network of Excellence in Nuclear Engineering (UNENE)*. 2014.
- [9] G.L. Brooks, "A Short History of the CANDU Nuclear Power System," *Ontario Hydro Demand/Supply Hearing*. 1993. [Online]. Available: <https://canteach.candu.org/content%20library/19930101.pdf>
- [10] W.R. Clendening et al, "Assessment and Management of Aging of Major Nuclear Power Plant Components Important to Safety: CANDU Pressure Tubes," *Engineering Safety Section - International Atomic Energy Agency (IAEA)*. 1998.
- [11] "Uranium and Nuclear Power Facts," *Government of Canada: Natural Resources Canada*. [Online]. 2022. Available: <https://www.nrcan.gc.ca/our-natural-resources/minerals-mining/minerals-metals-facts/uranium-and-nuclear-power-facts/20070#L6>
- [12] "Darlington Nuclear's Unit 1 Sets World Record for Continuous Operation." *Ontario Power Generation (OPG)*. 2020. [Online]. Available: <https://www.opg.com/stories/darlington-nuclears-unit-1-sets-world-record-for-continuousoperation/#:~:text=Unit%20at%20OPG's%20Darlington,by%20a%20nuclear%20power%20reactor.>
- [13] C.M. Morad et al, "CANDU Study and Review," *International Nuclear Atlantic Conference (INAC)*. 2017.
- [14] P.K. Chan, "CCE 533 Nuclear Fuel Engineering Part 2: Fuel Production," *Royal Military College of Canada, Kingston, ON*. 1 - 133. 2021.
- [15] "Nuclear Fuel Manufacturing," *Government of India Department of Atomic Energy*, 2019. [Online]. Available. <https://www.nfc.gov.in/nuclear-fuel.html>
- [16] G. Horhoianu, "A Finite Element Model for Static Strength Analysis of CANDU Fuel Bundle," *Dragos Victor IONESCU Institute of Nuclear Research*. Pitesti, Romania. 2005.

[17] J.S. Bell & B.J. Lewis, "CANDU Fuel Bundle Deformation Modeling with COMSOL Multiphysics," *ELSEVIER Nuclear Engineering and Design*, (250) 134-141. 2012.

[18] P.K. Chan, "CCE 533 Nuclear Fuel Engineering Part 1: Introduction Lectures," *Royal Military College of Canada, Kingston, ON*. 1 - 88. 2021.

[19] J.H. Park & Y.M. Song, "Thermal Hydraulics of Advanced 37-Element Fuel Bundle in Crept Pressure Tubes," *EPJ Nuclear Science and Technology*, (2-16). 2016.

[20] L.K. Beland, MECH 883 Computer Modeling of Nuclear Materials I - IV. *Queen's University Department of Mechanical and Materials Engineering, Kingston, ON*. 2022.

[21] P.K. Chan, "CCE 533 Nuclear Fuel Engineering Part 3: Fuel Thermal Performance Lectures," *Royal Military College of Canada, Kingston, ON*. 1 - 34. 2021.

[22] B. Lewis, E. Nihan Onder & A.A. Prudil, "Fundamentals of Nuclear Engineering," *John Wiley & Sons Ltd, West Sussex, UK*. 2017.

[23] D. Dennier & A.M. Manzer, "Element BOW Profiles from New and Irradiated CANDU Fuel Bundles," *Fuel Design Branch - Atomic Energy of Canada Ltd, Mississauga, ON*. 1996.

[24] M. Tayal, S.D. Yu, & P.N. Singh, "Improvements, Verifications and Validations of the BOW Code," *Atomic Energy of Canada Ltd (AECL)*. 1995.

[25] M. Tayal, "Modeling CANDU Fuel Under Normal Operating Conditions: ELESTRES," *Atomic Energy of Canada Ltd (AECL)*. 1987.

[26] "MOOSE Simulation Environment," Idaho National Laboratory. 2022. [Online]. Available: <https://moose.inl.gov/SitePages/Home.aspx>

[27] R. Soni, "Analyzing the Three-Dimensional Deformation Behaviour of an Empty CANDU® Fuel Bundle Using the Finite Element Method," *Royal Military College of Canada - Thesis*. 2017.

- [28] A. Williams & S. Yatabe, "An ANSYS Based 3-Dimensional Thermomechanical Model of a CANDU Fuel Pin," *Canadian Nuclear Laboratories Nuclear Review*. (6-2). 2017.
- [29] J.S. Bell & B.J. Lewis, "CANDU Fuel Bundle Deformation Modeling with COMSOL Multiphysics," *ELSEVIER Nuclear Engineering and Design*, (250) 134-141, 2012.
- [30] K. Lee, D. Wowk & P.K. Chan, "Finite Element Analysis of an Empty 37-Element CANDU® Fuel Bundle to Study the Effects of Pressure Tube Creep," *CNL Nuclear Review, Royal Military College of Canada, Kingston, ON*, 2020.
- [31] A.M. Manzer, "Deformation Assessment of Extended Burnup Bruce B Bundle G85159W," *CANDU Owners Group Inc, Toronto, ON*, 2003.
- [32] P.T. Henry, (1996) "Fuel String Supporting Shield Plug (F3SP) for Ontario Hydro - Bruce NGS," *General Electric Canada - Nuclear Fuel Handling, Peterborough, ON*, 1996.
- [33] D.V. Hutton, *Fundamental of Finite Element Analysis*. McGraw Hill, 2004.
- [34] A. Rabindranath, "Stochastic Simulation and Lagrangian Dynamics," 2011. [Online]. Available. <http://stochasticandlagrangian.blogspot.com/2011/07/what-does-shape-function-mean-in-finite.html>
- [35] D. Wowk, "MEE 547 Advanced Finite Element Analysis Lecture Notes Ch 1 - 11" *Royal Military College of Canada, Kingston, ON*, 2021.
- [36] W. Frei, "Meshing Consideration for Linear Static Problems," *COMSOL - COMSOL Blogs*, 2013. [Online]. Available. <https://www.comsol.com/blogs/meshing-considerations-linear-static-problems/>
- [37] "What is FEA | Finite Element Analysis," *Simscale*, 2023. [Online]. Available. <https://www.simscale.com/docs/simwiki/fea-finite-element-analysis/what-is-fea-finite-element-analysis/>
- [38] "Newton Raphson Method," *Byjus - The Learning App*. 2023. [Online]. Available. <https://byjus.com/maths/newton-raphson-method/>

- [39] G.A. Reymann et al, "MATPRO - Version 10 A Handbook of Material Properties for use in the Analysis of Light Water Reactor Fuel Rod Behaviour" *Idaho National Engineering Laboratory, TREE-NUREG-1180*, 1978.
- [40] "ANSYS Help Files - Chapter 4: Nonlinear Material Properties," *ANSYS Mechanical APDL 2023 R1*, 2023. [Online]. Available. <https://ansyshelp.ansys.com/>
- [41] D. Kaddour, S. Frechinet, A.F. Gourgues-Lorenzon, J.C. Brachet, L. Portier, and A. Pineau, "Experimental determination of creep properties of zirconium alloys together with phase transformation," *Elsevier Scripta Materialia*, 51 (6), pp. 515-519. 2004.
- [42] M. Tayal, B. Wong, & Y. Shudoh, "Effect of Radial Power Profile on Endplate Integrity," *Fourth International Conference on CANDU Fuel, Pembroke, ON*. 1-4, 1994.
- [43] D.J.C. Pierce, P.K. Chan, & W. Shen, "Mitigation of End-Flux-Peaking in Fresh CANDU Fuel Bundles Using Neutron Absorbers," *Journal of Nuclear Engineering and Radiation Science*, Vol. 6 / 031601-15, 2020.
- [44] F. Abbasian, G.I. Hadaller, & R.A. Fortman, "Single-Phase and Two-Phase CFD Simulations of the Coolant Flow Inside A Bruce/Darlington CANDU Flow Channel," *Stern Laboratories Inc, Hamilton, ON*, 2015.
- [45] P. Hudson, "Design - 37-Element Fuel Bundle for Ontario Hydro 808E587," *General Electric Canada, Peterborough, ON*. 1990.
- [46] CANDU 6 Program Team. "CANDU® Technical Summary," *Atomic Energy of Canada Ltd, Mississauga, ON*. 2005.
- [47] L.C. Walters and A.F. Williams, "Fuel Bundle Deformation Model," *International Conference on CANDU Fuel*, 2003.
- [48] K.H. Kang, H.J. Ryu, K.C. Song, & M.S. Yang, "Thermal Expansion of UO<sub>2</sub> and Simulated DUPIC Fuel," *Journal of Nuclear Materials*, Vol. 301, pp. 242-244, 2002.

[49] “Beam Deflection Tables,” *MechaniCal Inc*, 2023. [Online]. Available. <https://mechanicalc.com/reference/beam-deflection-tables>

[50] T. Wierzbicki, “Deflection Behaviour for Beams with Compressive Axial Loads and Transverse Loads,” *LibreTexts Engineering, MIT*, 2021.